Dist: A

REPORT DOCUMENTATION PAGE

Form Approved
OMB No. 0704-0188

AGENCY USE ONLY (Leave blank)	2. REPORT DATE	3. REPORT TYPE AND DATES COVERED
	1 July 1994	Annual Technical: 07/01/93-06/30/94

4. TITLE AND SUBTITLE
(U) Hypervelocity Air Flows with Finite Rate Chemistry

5. FUNDING NUMBERS
PE - 61103D
PR - 3484
SA - AS
G - F49620-93-1-0373

6. AUTHOR(S)
I. Boyd, R. Hanson, M. Holden, J. Kunc, E. P. Muntz

7. PERFORMING ORGANIZATION NAME(S) AND ADDRESS(ES)
Department of Aerospace Engineering
University of Southern California
Los Angeles, CA 90089-1191

8. PERFORMING ORGANIZATION REPORT NUMBER
URI 92-1
AFOSR-TR- 94 0573

9. SPONSORING/MONITORING AGENCY NAME(S) AND ADDRESS(ES)
AFOSR/NA
110 Duncan Avenue, Suite B115
Bolling AFB DC 20332-0001

10. SPONSORING/MONITORING AGENCY REPORT NUMBER

SEP 22 1994

11. SUPPLEMENTARY NOTES

12a. DISTRIBUTION/AVAILABILITY STATEMENT
Approved for public release; distribution is unlimited
A

12b. DISTRIBUTION CODE

13. ABSTRACT *(Maximum 200 words)*

In the first year of this program the foundation for a productive collaboration has been laid. Using the CUBRC experiments as a focus detailed design calculation for LENS flow fields about a sphere cone have been completed and reported. Considerations of PLIF and PEBF measurements have been made for LENS as preliminary studies for this program. Very encouraging results have been obtained and reported on the efficient calculation of state and energy dependent vibrational transition probabilities. Initial PLIF measurements in a small shock tunnel have been made and reported.

82 pg

94-30415

94 9 22 001

DTIC

14. SUBJECT TERMS
Nonequilibrium Flows, Nonequilibrium Flow Computation, Nonequilibrium Flow Measurements, PLIF, Pulsed e-beam Fluorescence, Vibrational Collision Probabilities

15. NUMBER OF PAGES
8

16. PRICE CODE

17. SECURITY CLASSIFICATION OF REPORT	18. SECURITY CLASSIFICATION OF THIS PAGE	19. SECURITY CLASSIFICATION OF ABSTRACT	20. LIMITATION OF ABSTRACT
Unclassified	Unclassified	Unclassified	UL

NSN 7540-01-280-5500

Standard Form 298 (890104 Draft)
Prescribed by ANSI Std 239-18
298-01

AD-A284 727

Summary of Research Progress

Because of the collaborative nature of this project the progress is summarized below for each organization involved. During the research time period the individual investigators have met three times in conjunction with their attendance at the Orlando, Reno and Colorado Springs AIAA meetings. Additionally, Professor Muntz has visited CUBRC in Buffalo twice during the research period for interchanges with CUBRC management and for technical discussion with M. Holden and others. A Stanford student spent the summer of 1992 at CUBRC and this summer two Stanford students and one USC student are in residence at CUBRC.

Research Progress at Cornell University (Professor Iain Boyd)

Completed Work

Numerical simulations were performed of candidate test conditions and body geometries to be tested in LENS. These were obtained using a computer code developed at NASA Ames Research Center by Grant Palmer. This code solves the Navier-Stokes equations with coupled thermal and chemical nonequilibrium relaxation. The code was installed and executed on the Silicon Graphics Indy work-station purchased through the URI program. The simulations were performed by the graduate student funded by the URI (Anand Srinivasan) and supervised by Professor Iain Boyd.

The results of a first series of numerical computations were presented at the AIAA Thermophysics Conference in June 1994 (*Boyd, I.D., Srinivasan, A., Muntz, E.P., Hanson, R.K., and Holden, M.S.*, "Thermochemical Nonequilibrium Design Calculations for Detailed Hypervelocity Experiments in the LENS Facility," AIAA Paper 94-2097). These consisted of hypersonic flows of air produced under typical LENS operating conditions. Flows were computed over various spherically-capped cone geometries. Here we summarize the important findings of this numerical study:

1. LENS is expected to produce flows with vibrational and chemical nonequilibrium. Along the stagnation streamline, the translational temperature overshoots the vibrational value. A significant degree of dissociation occurs for both oxygen (which is nearly fully dissociated) and nitrogen. Above the shoulder of the body, where rapid expansion occurs, the vibrational mode freezes and exceeds the translational value.
2. Variation of the cone angle emphasizes different aspects of hypervelocity flows. At large angle, the effects of recombination along the body are observed. At small angle, the effects of rapid expansion and thermochemical freezing become significant.
3. The physical effects predicted in the computations such as thermal nonequilibrium, significant dissociation, freezing, and recombination, should all be measurable using the non-intrusive optical diagnostic techniques being developed at USC and Stanford. The signal strengths and spatial resolution appear adequate for acquisition of accurate and useful measurements.
4. It is concluded that successful, detailed measurements of this type of flow in LENS will contribute significantly to our understanding of these flows. Almost certainly, the

new measurements will indicate failings of the numerical models currently employed to simulate these phenomena.

Future Work

Further simulations will be conducted to identify additional flow conditions and possibly additional geometries of interest for testing in LENS. This study will concentrate on pushing the flow conditions to higher altitudes. The Navier-Stokes code is to be extended to compute separate vibrational relaxation for each molecular species present in the flow. Sensitivity of the computations to changes in chemical models and rate constants will be investigated.

In addition to using the Navier-Stokes solver, it is intended at the highest altitude conditions to consider use of computer codes developed at Cornell University using the direct simulation Monte Carlo method (DSMC). Experimental data recently generated in LENS on the surface of an interplanetary probe geometry will also be calculated using the DSMC technique.

Research Progress at CUBRC (Dr. Mike Holden)

During the past year, CUBRC has been preparing experimental research programs in two areas: (1) the study of real gas effects in air at velocities from 10,000 to 15,000 ft/sec, and (2), a study of hydrogen combustion associated with scramjet propulsion at velocities from 8,000 to 14,000 ft/sec. Both of these programs are being conducted in the LENS facility and are being fully supported by other members of the URI research contract.

The studies of real gas effects center around two flow configuration—a sting-mounted planetary probe model, and a large sphere/cone/flare configuration. The experimental studies that have or will be conducted are focused on the effects of flowfield chemistry on the flow structure and the surface heat transfer and pressure. These efforts are fully integrated in both the design and analysis phases with detailed computations using the DSMC codes, and with Navier-Stokes solvers such as the GASP code, all of which incorporate non-equilibrium real gas chemistry.

The experimental studies of hydrogen combustion in hypervelocity flows are centered around measurements of the mixing and combustion of single or multiple hydrogen jets, angled to the airflow, in an environment typical of that generated in a hypersonic combustor of a vehicle flying at velocities between 8,000 ft/sec and 14,000 ft/sec. Here, the emphasis is on developing and understanding the combined and separate effects of mixing and combustion on the flowfield characteristics and pressures and the heating leads generated in the combustion chamber and the subsequent generation of thrust. Again, real gas effects, as well as combustion, are the object of our investigation.

In both the real gas and the combustion studies, the development, calibration, and use of such advanced non-intrusive instrumentation as electron-beam techniques, laser-induced fluorescence (LIF), and holographic interferometry to measure flowfield properties is an integral part of the research program.

Studies of Real Gas Effects

There are two basic investigations being conducted as a part of our study of real gas effects in hypervelocity flows. These center around investigations with a sting-mounted planetary probe, and studies of the non-equilibrium flowfield and surface characteristics of a large sphere/cone/flare configuration. Both of these studies will be conducted over a velocity range of 8,000 to 15,000 ft/sec in the LENS facility. In each program, we will employ surface and flowfield instrumentation to examine real gas effects on flowfield characteristics. Detailed calculations are being made with DSMC and Navier-Stokes codes to design the experimental studies and analyze their results.

Real Gas Experiments with the Planetary Probe Configuration

Experiments ahve been conducted with the sting-mounted planetary probe configuration to examine the heat transfer and pressure to the forebody and wake region as well as to obtain flowfield information for examination of the bow-shock structure and the radiative effects of the flowfield. The planetary probe, which is a spherically-blunted 70-degree cone mounted on a cylindrical sting, is a configuration that has been selected for comparative studies in the LENS shock tunnel, in the HEG piston-driven shock tunnel, in the NASA Ames combustion-driven shock tunnel, in the GASL expansion tunnel, and possibly the T5 Facility at Cal-Tech. The purpose of the studies, which are to be conducted at nominally the same freestream conditions, is to analyze the relative performance of these facilities under high-enthalpy (5 Mj/kg and 10 Mj/kg) conditions and to generate fundamental measurements with which to examine the performance of models of real gas effects employed in the DSMC and Navier-Stokes solvers. Experimental studies have already been conducted at 5 Mj/kg on this configuration in the LENS facility, and the test conditions have been released to members of the American and European computational communities to obtain predictions of these flows. The measurements of the flowfield characteristics and the distribution of properties of the surface of the body will not be released to the predictors until their results are compared with the experimental data at the European Aerospace Meeting in November 1994. Both DSMC and Navier-Stokes solutions are being obtained under the current contract by members of the URI research team. The corresponding measurements at 10 Mj/kg are to be conducted within the near future. Later, we intend to obtain flowfield density and temperature (both translational and vibrational) measurements in the bow-shock and wake regions of this flow. These measurements will provide invaluable data with which to analyze the models of vibrational relaxation and coupled dissociation effects in both nitrogen and air flows. An active dialog is anticipated between all members of the experimental and theoretical communities in the study of these flows.

Real Gas Studies with the Large Sphere/Cone/Flare Configuration

Currently, we are actively engaged in the design of the model and the fabrication of the instrumentation to perform studies of the flowfield over the large sphere/cone/flare configuration. Detailed computations have been performed to select the optimum model geometry to examine non-equilibrium real gas flows along the cone and in the recirculation region at

the cone/flare junction. This configuration would be run over a range of freestream conditions in both air and nitrogen to obtain conditions to examine flows from frozen to fully equilibrium gas flow chemistry. Currently, electron-beam equipment and instrumentation are being prepared at USC, Imperial College, and CUBRC for these studies. Also, instruments to examine flowfield radiation and flowfield chemistry (LIF) are being assembled at Stanford University and CUBRC. This same instrumentation would be used in later studies of the planetary probe and hydrogen combustion.

Studies of Hydrogen Combustion in Hypervelocity Flows

Models and instrumentation are currently being prepared for a preliminary study of hydrogen combustion in hypervelocity flows, to be conducted in the LENS facility in late August or September. In this program, we plan to employ a model that has been previously used to supply combustion data for the NASP program. This model is being extensively instrumented with heat transfer, pressure, and skin-friction instrumentation. High-speed schlieren photography and holographic interferometry measurements are planned to examine the flowfield structure. These studies will be conducted at 8,000, 10,000, 12,000, and 14,00 ft/sec to examine the effects of freestream velocity on the combustion and mixing of hydrogen from single and multiple jets injected into the flow. both air and nitrogen will be used as the test medium so that the combined and separate effects of mixing and combustion can be examined. Theoretical prediction employing Navier-Stokes codes are being or will be obtained to compare with the experimental measurements. These preliminary studies will provide the data from which we will select test cases in which extensive flowfield studies will be conducted with LIF to examine the mixing and combustion of these flows and to provide fundamental data for evaluation and improvement of the combustion and turbulence models used in the codes.

Research Progress at Stanford (Professor Ron Hanson)

The primary goal of this program is the application of planar laser-induced fluorescence (PLIF) diagnostic concepts in the LENS hypersonic shock tunnel facility. Toward this end, the Stanford effort during our first year of support focused initially on modifying one of our small shock tubes to provide hypersonic flow capability in a reflected shock tunnel configuration. Two different end-wall geometries and nozzle designs were tested to establish the extent of perturbations in stagnation conditions, tunnel start-up times, and the quality of the flow at the nozzle exit. In these experiments, the primary diagnostics were reflected-zone pressure, pulsed shadowgraphy and PLIF of NO; the gas was typically argon seeded with up to 1% NO. Once the tunnel was operating satisfactorily, a cylinder model was mounted in the supersonic/hypersonic flow to provide a realistic environment for developing PLIF measurement capability. A number of experiments were then conducted to provide useful experience for the two new students associated with this program. The relatively simple procedures for operating the shock tunnel allow fast turnaround times, as short as ten minutes between runs, which facilitate (relative to large-scale facilities such as LENS) study and development

of complex diagnostics. The optimization and application of a quantitative PLIF diagnostic requires selection and close control of several variables ranging from electronic timing (laser, gated intensifier, shock detection, etc.), laser parameters (energy/pulse, wavelength, linewidth, timing, optical train, etc.), spectroscopic parameters (absorption transition), and camera parameters (intensifier gating, laser sheet corrections, camera focusing). At the present time, the students and staff involved with this project have progressed to a stage that useful PLIF data are obtained on nearly every shock tube run.

During this summer period, the two students are working at CUBRC (Calspan) to gain experience in the LENS facility. They are beginning to address the problems associated with implementing PLIF in this facility, including design of the laser delivery system (i.e., the sheet illumination in the tunnel flow) and mounting of the CCD camera. goals for the summer include using the CCD camera, in a gated mode, to acquire images of radiative emission from hypersonic flow over a body at high Mach numbers. Once the electronic triggering is under control, the spectral luminosity of the flow will be characterized, since this will represent a sever background problem for the PLIF signals. The results from these tests will be used to plan the spectral (and temporal) filtering which will be needed in actual PLIF experiments. Although the present emphasis is on detection of NO in hypersonic flow over a body, there is a chance that combustion experiments will also be run this summer, in which case the objective will be detect OH in combusting H_2-air flows.

With regard to publications, one paper based on the work at Stanford to study tunnel start-up with PLIF has been presented (AIAA, Colorado Springs, June 1994) and another based on PLIF measurements of the flow over a cylinder has been submitted for presentation (AIAA, Reno, January 1995).

Progress at USC

Transition Probabilities and Viscosities (J. A. Kunc)

The main goals of this part of the program are: 1) to obtain the state-to-state transition probabilities for molecular collisions (with the molecules in arbitrary vibrational-rotational states) resulting in the V-T (vibration-translation) and V-V (vibration-vibration) exchange, and 2) to provide a general, comprehensive study of the effect of dissociation on the viscosity of high-temperature gases.

1) Dynamics of the V-T and V-V transitions is of fundamental importance in high-energy flows because the vibrational excitation of molecules can cause a serious unbalance in the distribution of the gas energy among the translational modes and internal modes of the gas molecules. In addition, vibrational excitation plays a crucial role in efficiency of dissociation and many chemical reactions. Therefore, this part of the program is devoted to evaluate computationally efficient (possibly analytical) expressions for the cross sections and transition probabilities for the V-T and V-V processes defined above.

The initial phase of this part the program (resulting in analytical temperature-dependent first-order perturbation theory expressions for V-T transitions in collisions of oxygen and nitrogen molecules) and the second phase (resulting in analytical energy-dependent infinite-

order perturbation theory expressions for V-T transitions in the collisions) have already been completed (see Appendix). The obtained results encourage development of an approach yielding the transition probabilities for both the temperature-dependent and energy-dependent V-V transition probabilities in the atmospheric gases such as nitrogen and oxygen. This development will be the subject of this part of the program in the incoming year. The approach will be based on the same infinite-order perturbation scattering theory because preliminary results indicate that the approach may lead to analytical V-V transition probabilities.

2) Investigation of momentum transfer in dissociating gases is of a primary importance for physics of supersonic and hypersonic flows because the temperatures in the flows are usually high enough to cause significant dissociation. Theoretical models of the momentum transfer in dissociating gases are of a special interest for description of the transport properties (viscosity, conductivity, diffusion coefficient) in high-energy flows because of the experimental difficulties involved in measuring these properties at high temperature. Therefore, a part of this program focuses on modeling of transport of momentum and energy in high-temperature gases with ongoing dissociation.

The initial phases of this research (resulting in a study of impact of dissociation on viscosity of high-temperature iodine vapor supported on a previous grant) has suggested that the impact can also be profound in other gases. Therefore, a significant part of this program in the coming year will be devoted to a general study of the viscosity of dissociating diatomic gases, especially atmospheric gases such as nitrogen and oxygen.

Pulsed electron beam flourescence (E. P. Muntz, D. A. Erwin)

As documented in AIAA-94-2631 and AIAA-94-2097 (see Appendix) a pseudo-spark electron gun has been purchased and operated with reasonable but not complete success relative to the application of obtaining diagnostic quality gas flow mesurements. A beam isolation method based on a series of replaceable vaporizing diaphragms has been designed, constructed and undergone successful initial tests. During the summer of 1994 the student (Fred Lutfy) who is responsible for the e-beam measurements is at CUBRC. He is at present gaining valuable experience making c.w. e-beam measurements in LENS for purposes of calibrating the LENS free stream properties and test time. This experience will be essential for the subsequent implementation of the pulsed e-beam fluorescence measurements. Refinements of the pseudospark e-beam are presently being considered and will be implemented this fall. We expect to be able to demonstrate a working pulsed e-beam fluorescence system suitable for installation in LENS by April 1995.

Personnel

I. Boyd
D. Erwin
R. Hanson
M. Holden
J. Kunc
E. P. Muntz

Publications

1. Holden, M. S., "Recent Advances in Hypersonic Test Facilities and Experimental Research," AIAA 93-5005.
2. Holden, M. S., Craig, J. E., Parker, R. A. and Kolly, J. M., "Aerothermal and Aero-Optical Seeker-Head Studies in the LENS Facility at Velocities Up to 3.5 km/sec,"
3. J. L. Palmer, A. F. P. Houwing, M. C. Thurber, S. D. Wehe, and R. K. Hanson, "PLIF Imaging of Transient Shock Phenomena in Hypersonic Flows", AIAA-94-2642.
4. E. P. Muntz, Iain Boyd, Andrew Ketsdever, "Rarefied Flow Testing in the 1990s: Measuring Those Phenomena that are Difficult to Calculate," AIAA-94-2631.
5. S. H. Kang and J. A. Kunc, "Energy Dependence of Vibration-Translation Transitions in Collisions of Neutral Particles," AIAA-94-2403.
6. I. D. Boyd, A. Srinivasan, E. P. Muntz, R. K. Hanson, M. S. Holden, "Thermochemical Nonequilibrium Design Calculations for Detailed Hypervelocity Experiments in the LENS Facility," AIAA-94-2097.

Presentations

1. Holden, M. S., "Recent Advances in Hypersonic Test Facilities and Experimental Research," AIAA/DGLR 5th International Aerospace Planes and Hypersonics Technologies Conference, 30 November - 3 December 1993, Munich, Germany.
2. Holden, M. S., Craig, J. E., Parker, R. A. and Kolly, J. M., "Aerothermal and Aero-Optical Seeker-Head Studies in the LENS Facility at Velocities Up to 3.5 km/sec," 3rd Annual AIAA/BMDO Interceptor Technology Conference, San Diego, CA, July 11–14, 1994.
3. J. L. Palmer, A. F. P. Houwing, M. C. Thurber, S. D. Wehe, and R. K. Hanson, "PLIF Imaging of Transient Shock Phenomena in Hypersonic Flows", 18th AIAA Aerospace Ground Testing Conference, June 20–23, 1994, Colorado Springs, Colorado.
4. E. P. Muntz, Iain Boyd, Andrew Ketsdever, "Rarefied Flow Testing in the 1990s: Measuring Those Phenomena that are Difficult to Calculate," 25th AIAA Plasmadynamics and Lasers Conference, June 20–23, 1994, Colorado Springs, Colorado.
5. S. H. Kang and J. A. Kunc, "Energy Dependence of Vibration-Translation Transitions in Collisions of Neutral Particles," 25th AIAA Plasmadynamics and Lasers Conference, June 20–23, 1994, Colorado Springs, Colorado.

6. I. D. Boyd, A. Srinivasan, E. P. Muntz, R. K. Hanson, M. S. Holden, "Thermochemical Nonequilibrium Design Calculations for Detailed Hypervelocity Experiments in the LENS Facility," 6th AIAA/ASME Joint Thermophysics and Heat Transfer Conference, June 20–23, 1994, Colorado Springs, Colorado.

APPENDIX

AIAA-94-2403

ENERGY DEPENDENCE OF VIBRATION-TRANSLATION TRANSITIONS IN COLLISIONS OF NEUTRAL PARTICLES

S.H. Kang and J.A. Kunc
Department of Aerospace Engineering
University of Southern California

25th AIAA Plasmadynamics and Lasers Conference
June 20-23, 1994 / Colorado Springs, CO

Energy dependence of vibration - translation transitions in collisions of neutral particles

Steve H. Kang and Joseph A. Kunc
Departments of Aerospace Engineering
University of Southern California
Los Angeles, California 90089-1191

Abstract

We study, using an operator solution of the Schrödinger equation for the collision system, the vibration - translation (V-T) energy exchange in collisions of diatomic homonuclear molecules. The energy- and temperature-dependent transition probabilities are evaluated for collisions of molecules in arbitrary vibrational states, and when the change of the vibrational quantum number of the target molecule during the V - T transition can be greater than one. Examples of numerical results are given for various transitions in $O_2 + O_2$ and $N_2 + N_2$ interactions.

1 Introduction

The one of important area of kinetic studies of high-temperature gases is energy transfer in molecular collisions. Particularly, determining probabilities of energy transfer between the translational motion and the vibrational motion of molecules is of wide spread interest. Calculations of the V - T transition probabilities as functions of the collision impact energy and impact parameter are not available for collisions of diatomic molecules. In this work we calculate such probabilities, using a quantum-mechanical approach,[1,2] studying the V-T energy transfer in the following collisions:

$$X_2(k) + X_2(v) \rightarrow X_2(k) + X_2(v'), \tag{1}$$

where a diatomic homonuclear molecule X_2 in a vibrational state v (v, v' and k are molecular vibrational quantum numbers) collides with another diatomic homonuclear molecule in a vibrational state k. After the collision, the target molecule X_2 is left in a vibrational state v', while the vibrational state of the incident molecule is the same as before the collision. (Both molecules are in the ground electronic states at all times).

The V-T transition probabilities of the present work are obtained using solution[1] of the time-dependent Schrödinger equation for the collision system (1) with the evolution operator transforming the initial state of the system into a final state at some time t. The transition probabililites for $t = \infty$ are then calculated from the probability amplitudes. Each molecule participating in the collision is represented during interaction by two identical vibrating atoms. The intermolecular potential energy (which depends on the intermolecular

distance and on the spatial orientation of the colliding molecules) is constructed as a sum of all pairwise (atom-atom) interactions in the collision system. Subsequently, analytical expressions for the V-T transition probabilities as functions of the collision impact parameter and impact energy are obtained. Averaging of the probabilities over the impact parameter gives the probabilities as functions of the collision impact energy, and subsequent averaging over the distribution of the impact energies in the gas gives the probabilities as functions of the gas temperature.

Anharmonicity and rotation of the molecules are taken into account by assuming that the vibrational part of the intramolecular potential is of the Morse type and that the rotational part is the centrifugal stretching potential that depends on the molecular rotational quantum number.[3,4] Therefore, although we consider only V-T transitions (simultaneous rotational transitions are ignored) the corresponding transition probabilities are functions of the initial (before collision) rotational quantum numbers of the molecules participating in the collisions.

2 Intramolecular potentials

The Morse rotating oscillator is used as a model of the rotational-vibrational motion of the diatomic molecules. The effective intramolecular potential energy U_{eff} of a diatomic molecule is given as

$$U_{eff}(R) = U_v(R) + U_J(R), \tag{2}$$

where $U_v(R)$ is the vibrational part and $U_J(R)$ is the rotational part of the potential.

The intramolecular potential of a rotationless Morse oscillator can be approximated by the Morse potential,

$$U_v(R) = D\left\{\exp[2\beta(R_e - R)] - 2\exp[\beta(R_e - R)]\right\}, \tag{3}$$

where D is the dissociation energy, referred to the minimum of the potential, R is the internuclear distance, R_e is the molecular bond length, and β is the Morse constant.

The rotational part of the intramolecular potential (2) is given by

$$U_J(R) = \frac{\hbar^2[J(J+1) - \Lambda^2]}{2\bar{\mu}R^2}, \tag{4}$$

with Λ being the quantum number for the axial component of the electronic angular momentum, and $\bar{\mu}$ being the reduced mass of the molecule. In the calculations we assume that the rotational part of the potential energy of the oscillator is[4],

$$U_J(R) = U_J(R = R_o) = \frac{\hbar^2 J(J+1)}{2\bar{\mu}R_o^2}, \tag{5}$$

where R_o is the position of the minimum of the effective potential U_{eff},

$$R_o = R_e + 4l_\alpha^4 J(J+1)/R_e^3, \tag{6}$$

where

$$l_\alpha^2 = \frac{\hbar}{2\beta(2\bar{\mu}D)^{1/2}}. \tag{7}$$

The rotational-vibrational energy (in cm^{-1}) of the rotating Morse oscillator with vibrational quantum number v and the rotational quantum number J is[5]

$$G_{v,J} = -D + \omega_e(v+1/2) - \omega_e x_e(v+1/2)^2 + B_e J(J+1) - D_e J^2(J+1)^2, \tag{8}$$

where ω_e, $\omega_e x_e$, B_e and D_e are the usual molecular spectroscopic constants .

3 Intermolecular potentials

We denote the target molecule as particle 1 and the incident molecule as particle 2 (see Fig.1). The distance between the centers of the colliding molecules is $\vec{r}$; the angle between the internuclear axis of the molecule 1 and $\vec{r}$ is denoted by θ_1 and the angle between the internuclear axis of the molecule 2 and $\vec{r}$ is denoted by θ_2. Here, r_1, r_2, r_3 and r_4 are the distances between the atoms in the collision system. The pairwise (atom-atom) interaction potentials are taken as Morse-type potentials,[2]

$$U^{(i)}(r_i) = D_m\{\exp[2\kappa(r_e^{(i)} - r_i)] - 2\exp[\kappa(r_e^{(i)} - r_i)]\}, \tag{9}$$

where D_m and κ are potential constants, and $r_e^{(i)}$ is the equilibrium value of r_i. Consequently, the resultant (overall) intermolecular potential is

$$U(r) = \sum_{i=1}^{4} U^{(i)}(r_i), \tag{10}$$

where r_e is the equilibrium value of r.

One should recall that the repulsive-attractive potential such as the potential (9) is not the only potential possible during interaction of two atoms. Depending on the spin vectors of the colliding atoms, the pairwise atom-atom potentials can be repulsive-attractive as well as repulsive potentials. However, in the case considered here, where the interacting molecules are in the electronic ground states, the pairwise interactions are dominated by the repulsive-attractive potential of type (9). Therefore, instead of statistical averaging over all possile potential curves of the particular atom-atom interaction we describe this interaction by the single intermolecular potential (9).

Taking the above into account, the overall intermolecular potential can be written as

$$\begin{aligned} U(r, x_1, x_2, \theta_1, \theta_2) &= U_o(r, \theta_1, \theta_2) + U_1(r, x_1, \theta_1, \theta_2) \\ &+ U_2(r, x_2, \theta_1, \theta_2) + U_{12}(r, x_1, x_2, \theta_1, \theta_2), \end{aligned} \tag{11}$$

where

$$\begin{aligned} U_o &= D_m\left\{\exp[2\kappa(r_e^{(i)} - r_e)]\exp(Q\cos\theta_1 - Q\cos\theta_2)\exp[2\kappa(r_e - r)] + \right. \\ &- \left. 2\exp[\kappa(r_e^{(i)} - r_e)]\exp(0.5Q\cos\theta_1 - 0.5Q\cos\theta_2)\exp[\kappa(r_e - r)]\right\}, \end{aligned} \tag{12}$$

$$\begin{aligned} U_1 &= D_m\left\{\exp[2\kappa(r_e^{(i)} - r_e)]\exp(Q\cos\theta_1 - Q\cos\theta_2)\exp[2\kappa(r_e - r)] + \right. \\ &- \left. \exp[\kappa(r_e^{(i)} - r_e)]\exp(0.5Q\cos\theta_1 - 0.5Q\cos\theta_2)\exp[\kappa(r_e - r)]\right\} x_1\kappa\cos\theta_1, \end{aligned} \tag{13}$$

$$U_2 = -D_m \left\{ \exp[2\kappa(r_e^{(i)} - r_e)] \exp(Q\cos\theta_1 - Q\cos\theta_2) \exp[2\kappa(r_e - r)] + \right.$$
$$\left. - \exp[\kappa(r_e^{(i)} - r_e)] \exp(0.5Q\cos\theta_1 - 0.5Q\cos\theta_2) \exp[\kappa(r_e - r)] \right\} x_2 \kappa \cos\theta_2, \quad (14)$$

$$U_{12} = -D_m \left\{ \exp[2\kappa(r_e^{(i)} - r_e)] \exp(Q\cos\theta_1 - Q\cos\theta_2) \exp[2\kappa(r_e - r)] + \right.$$
$$- 0.5 \exp[\kappa(r_e^{(i)} - r_e)] \exp(0.5Q\cos\theta_1 - 0.5Q\cos\theta_2) \exp[\kappa(r_e - r)] \Big\}$$
$$\times x_1 x_2 \kappa^2 \cos\theta_1 \cos\theta_2, \quad (15)$$

where $Q = R_e\kappa$, and x_k is the deviation of the internuclear distance of the kth molecule from its equilibrium distance R_e.

The first term in Eq. (11) describes the relative motion of the colliding molecules accompanied by vibrational excitation and deexcitation. The second and the third terms represent the coupling between the relative motion and the vibrational motion of the molecule 1 and 2, respectively. The last term represents the coupling between these vibrational motions of both molecules and between the vibrational motions and the relative motion of the molecules. The perturbation potential U_1 causes V-T energy transfer between the molecule 1 and translation, and the perturbation potential U_2 causes V-T energy transfer between the molecule 2 and translation. Since we are interested in V-T of the one of the colliding molecules, U_1 is chosen. Using relationships (9) in Eq. (13) and averaging over the angles θ_1 and θ_2 one has

$$U_1(r_1, x_1) = \frac{1}{4}\int_0^\pi \int_0^\pi U_1(r_1, x_1, \theta_1, \theta_2) \sin\theta_1 \sin\theta_2 d\theta_1 d\theta_2$$
$$= \frac{D_m^* x_1}{R_e} \left\{ h_1 \exp[2\kappa(r_e^* - r)] - 2h_2 \exp[\kappa(r_e^* - r)] \right\}, \quad (16)$$

where $h_1 = Q\coth Q - 1$, $h_2 = Q\coth(Q/2) - 2$, $Q = \kappa R_e$, and D_m^* and r_e^* are defined, respectively, as,

$$D_m^* = D_m \left(\frac{4\sinh^2(Q/2)}{Q\sinh Q} \right)^2, \quad (17)$$

and

$$r_e^* = r_e - \kappa^{-1} \left\{ Q + 2\ln\left[\frac{2\sinh(Q/2)}{\sinh Q} \right] \right\}. \quad (18)$$

4 Transition probabilities

The general expression for the probability that the target molecule will be excited during the collision (1) from a vibrational state v to a vibrational state v' (while the incident molecule will deexcite from a kth vibrational state to a k'th vibrational state) is[6,2]

$$P_{vv'}^{kk'} = \lim_{t\to\infty} \left| (k'v'|\hat{U}(t, -\infty)|kv) \right|^2, \quad (19)$$

where $\hat{U}(t, -\infty)$ is the unitary time evolution operator which at $t \to -\infty$ describes the system initial (unperturbed) state $|kv\rangle$. The relationship (19) applies to any pair of oscillators

with the same or different vibrational frequencies and, unlike perturbation methods is not restricted to small transition probabilities or single-quantum transitions.

The time-dependent Schrödinger equation for the collision system under consideration is

$$i\hbar\frac{\partial|\Psi(t)\rangle}{\partial t} = H(t)|\Psi(t)\rangle, \tag{20}$$

where $|\Psi(t)\rangle$ represents a state of the collision system at time t, and $H(t)$ is the time-dependent Hamiltonian,

$$H(t) = \frac{p_1^2}{2M_1} + \frac{p_2^2}{2M_2} + \frac{M_1\omega_1^2x_1^2}{2} + \frac{M_2\omega_2^2x_2^2}{2} + \frac{\partial^2U(r,x_1,x_2,t)}{\partial x_1\partial x_2}x_1x_2, \tag{21}$$

where $U(r,x_1,x_2,t)$ is the θ_1- and θ_2-averaged intermolecular potential, and where the last term on the right-hand-side is responsible for the energy transfer between the colliding molecules; M_1 and M_2 are masses, p_1 and p_2 are momenta, ω_1 and ω_2 are vibrational angular frequencies of the molecule 1 and 2, respectively, and the perturbing force $F(t)$ causing the energy transfer in the collision can be obtained from the last term on the right-hand-side.

The equation (20) can be solved using the approach proposed by Goldman and Krivchenov[7] and Shin[1,8]. The approach seeks solution of the equation (20) in the following form

$$|\Psi(t)\rangle = \hat{U}(t,-\infty)|\Psi(-\infty)\rangle, \tag{22}$$

where the time evolution operator must satisfy the equation

$$i\hbar\frac{d\hat{U}(t,-\infty)}{dt} = H(t)\hat{U}(t,-\infty), \tag{23}$$

with the initial condition $\hat{U}(-\infty,-\infty) = 1$.

It was shown by Shin[2,8], using Lie algebra[9,10] that the solution Eq. (22) can be written as

$$|\Psi(t)\rangle = c(t)\exp[f(t)\mathbf{a}_1\mathbf{a}_2^\dagger]\exp[g(t)\mathbf{a}_1^\dagger\mathbf{a}_2]\exp[s(t)(\mathbf{a}_1^\dagger\mathbf{a}_1 - \mathbf{a}_2^\dagger\mathbf{a}_2)]|\Psi(-\infty)\rangle, \tag{24}$$

where $|\Psi(-\infty)\rangle$ represents the system initial state $|kv\rangle$, and $\mathbf{a}$ and $\mathbf{a}^\dagger$ are creation and anihilation operators, respectively.[6].

Substituting relationship (24) into Eq. (20) one obtains the following set of equations:

$$c(t) = e^{-i(\omega_1+\omega_2)t/2}, \tag{25}$$

$$i\hbar\frac{df(t)}{dt} + \Delta Ef(t) + F(t)f^2(t) - F(t) = 0, \tag{26}$$

$$i\hbar\frac{dg(t)}{dt} - \Delta Eg(t) - 2F(t)f(t)g(t) - F(t) = 0, \tag{27}$$

$$i\hbar\frac{ds(t)}{dt} - F(t)f(t) - \frac{\Delta E}{2} = 0, \tag{28}$$

with the initial conditions,

$$f(-\infty) = g(-\infty) = s(-\infty) = 0 \quad \text{and} \quad c(-\infty) = 1, \tag{29}$$

where ΔE is the mismatch energy of the vibrational states of molecule.

Solution of the equations (20) - (28) can be simplified because in the case of the V - T collision we assume that the collision does not change the vibrational state of the incident molecule, that is, we assume that $k' = k$. In such case the perturbation energy is $U_1(r, x_1)$ (see Eq. (16)). Subsequently, in the case of the V - T collisions the perturbing force $F(t)$ and the energy $U_1(t, x_1)$ are related as follows:

$$U_1(t, x_1) = F(t)(\mathbf{a}_1^\dagger + \mathbf{a}_1). \tag{30}$$

The time dependence of the angle-averaged energy $U_1(t, x_1)$ is obtained from $U_1(r, x_1)$ using the expression for the collision trajectory, $r(t)$, which can be written as

$$t = \left(\frac{\mu}{2}\right)^{1/2} \int_{r^*}^{r} \frac{dr}{[E - U_o(r)]^{1/2}}, \tag{31}$$

where, as before, μ is the reduced mass of the collision system, E is the impact energy of the collision, and r^* is the distance of the collision closest approach.

Relationships (30), (31) and (16) gives the following integral of the perturbing force:

$$\left[\int_{-\infty}^{+\infty} F(t) e^{i\omega_1 t} dt\right]^2 = \hbar^2 \gamma, \tag{32}$$

where, the dependence on the impact energy E and on the impact parameter b are introduced by replacing the energy E in Eq. (32) by

$$E_s'' = \frac{1}{4}\left\{\left[E\left[1 - \left(\frac{b}{r^*}\right)^2\right] \pm \epsilon_{vv'}\right]^{1/2} + \left[E\left[1 - \left(\frac{b}{r^*}\right)^2\right]\right]^{1/2}\right\}^2, \tag{33}$$

where it is quite accurate to assume[11] that r^* is equal to the hard-sphere collision diameter. The relationship (33) was obtained using the following replacements: 1) the impact energy of the collision, E, is replaced[12] by the symmetrized energy $E_s' = (E_i^{1/2} + E_f^{1/2})^2/4 = [(E \pm \Delta E)^{1/2} + E^{1/2}]^2/4$, (plus sign is for the exothermic collision and minus sign is for the endothermic collision, and E_i and E_f are initial and final energies of the collision system, respectively), and 2) the energy E is subsequently replaced by $E[1 - (b/r^*)^2]$ (see Ref.13).

Using the above assumptions the probability (19) for the V - T collisions of type (1) (with $k' = k$) can be given as[14,2,15]

$$P_{v,v'}(E, b) = v!v'!\gamma^{|v'-v|} \exp[-\gamma] \left[\sum_{n=0}^{v_m} \frac{(-1)^n \gamma^n}{n!(v_m - n)!(|v' - v| + n)!}\right]^2, \tag{34}$$

where v_m is the lesser of v and v'.

The energy-dependent V-T transition probabilities for the diatomic - diatomic molecule collision is

$$P_{vv'}(E) = \frac{1}{\pi r^{*2}} \int_0^{r^*} 2\pi P_{vv'}(E,b) b db, \tag{35}$$

and the temperature-dependent probability for the $v \rightarrow v'$ V-T transition in gas where the distribution of the collision impact energies is a Maxwellian distribution of temperature T is

$$P_{vv'}(T) = \frac{2}{\pi^{1/2}(kT)^{3/2}} \int_0^{\infty} E^{1/2} P_{vv'}(E) \exp(-E/kT) dE. \tag{36}$$

The relationships (34) - (36) can be used to calculate the cross sections and rate coefficients for the V - T $v \rightarrow v'$ transitions discussed above. The corresponding cross section is

$$\sigma_{vv'}(E) = 2\pi \int_0^{r^*} P_{vv'}(E,b) b db, \tag{37}$$

and the rate coefficient in the gas in local thermal equilibrium at temperature T is

$$k_{vv'}(T) = \int\int \sigma_{vv'}(w) w F_1(\mathbf{v_1}) F_2(\mathbf{v_2}) d\mathbf{v_1} d\mathbf{v_2}, \tag{38}$$

where $F_1(\mathbf{v_1})$ and $F_2(\mathbf{v_2})$ are Maxwellian velocity distributions of the colliding molecules, and w is the relative speed of the molecules before the collision. The total energy of the binary collision system in laboratory coordinates is $M_1 v_1^2/2 + M_2 v_2^2/2 = (M_1 + M_2)V^2/2 + \mu w^2/2$, and $d\mathbf{v_1} d\mathbf{v_2} = d\mathbf{V} d\mathbf{w}$ ($\mathbf{V}$ is the velocity of the center of mass of the collision system in the laboratory coordinates). Therefore, the relationship (38) can be rewritten as

$$k_{vv'}(T) = 2\pi r^{*2} \left(\frac{8kT}{\pi\mu}\right)^{1/2} \int_0^1 \int_0^{\infty} P_{vv'}(T; x, y) x y e^{-x} dx dy, \tag{39}$$

where $x = \mu w^2/2kT = E/kT$ and $y = b/r^*$.

Results

Examples of the V-T transition probabilities $P_{v,v-1}(E)$ and $P_{v,v-2}(E)$ for vibrational deexcitation of nitrogen and oxygen molecules in collisions (1) are given in Figs. 2 - 7. The probabilities, obtained from Eq. (35), are strong functions of the impact energy E, and increasing functions of the vibrational quantum number v at low impact energies and decreasing functions of v at high impact energies. One can also see from the figures that at higher impact energies the probabilities $P_{v,v'}(E)$ for $\Delta v = v - v' = 2, 3$ are often not negligable when compared to $P_{v,v'}(E)$ for $\Delta v = 1$.

Acknowledgments

We thank Alex Dalgarno, Evgenii Nikitin and Hyung Shin for many comments. This work was supported by the AFOSR/URI Grant F49620-93-1-0373 and AFOSR/URI Grant 90-0170.

[1]H. K. Shin, J. Phys. Chem. **77**, 1666 (1973).

[2]H. K. Shin, in *Dynamics of Molecular Collisions*, edited by W. H. Miller (Plenum, New York, 1976), p. 131.

[3]J. A. Kunc, J. Phys. B **23**, 2553 (1990).

[4]J. A. Kunc, J. Phys. B **24**, 3741 (1991).

[5]G. Herzberg, *Spectra of Diatomic Molecules* (Van Nostrand Reinhold, New York, 1961).

[6]J. D. Kelley, J. Chem. Phys. **56**, 6108 (1972).

[7]I. I. Goldman and V. D. Krivchenkov, in *Problems in Quantum Mechanics*, edited by (Addison-Wesley, New York, 1961), p. 103.

[8]H. K. Shin, J. Chem. Phys. **75**, 220 (1981).

[9]J. Wei and E. Norman, J. Math. Phys. **4**, 575 (1963).

[10]J. Wei and E. Norman, Proc. Am. Math. Soc. **15**, 327 (1964).

[11]E. E. Nikitin, *Theory of Elementary Atomic and Molecular Processes in Gases* (Clarendon, Oxford, 1974).

[12]F. E. Heidrich, K. R. Wilson, and D. Rapp, J. Chem. Phys. **54**, 3885 (1971).

[13]K. Takayanagi, Prog. Theor. Phys., Kyoto **8**, 497 (1952).

[14]N. Rosen and C. Zener, Phys. Rev. **40**, 502 (1932).

[15]H. K. Shin and P. L. Altick, Chem.Phys.Lett **52**, 580 (1977).

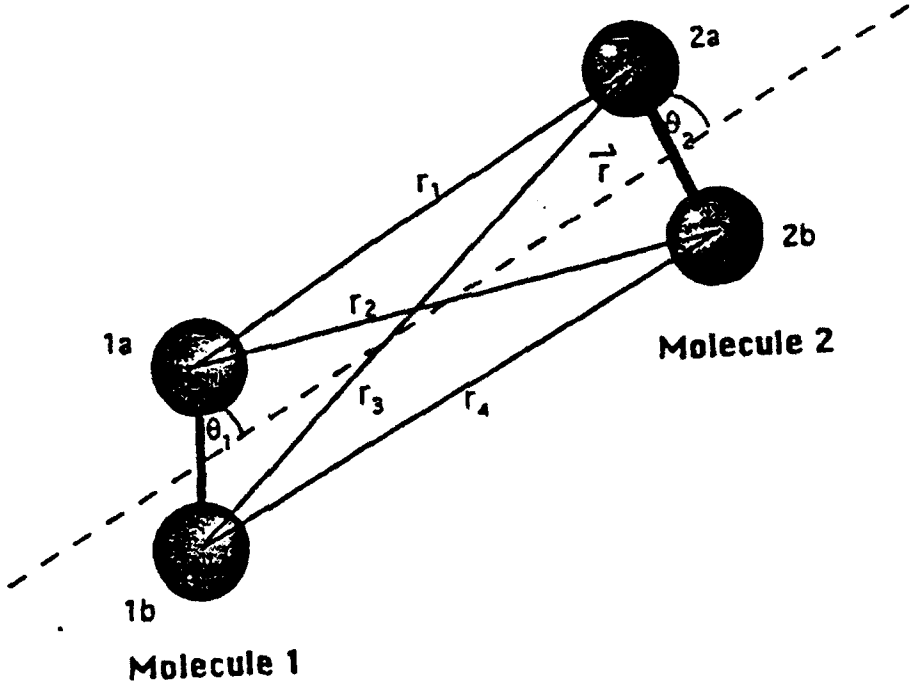

Fig.1

The geometry of the collision system of two diatomic homonuclear molecules.

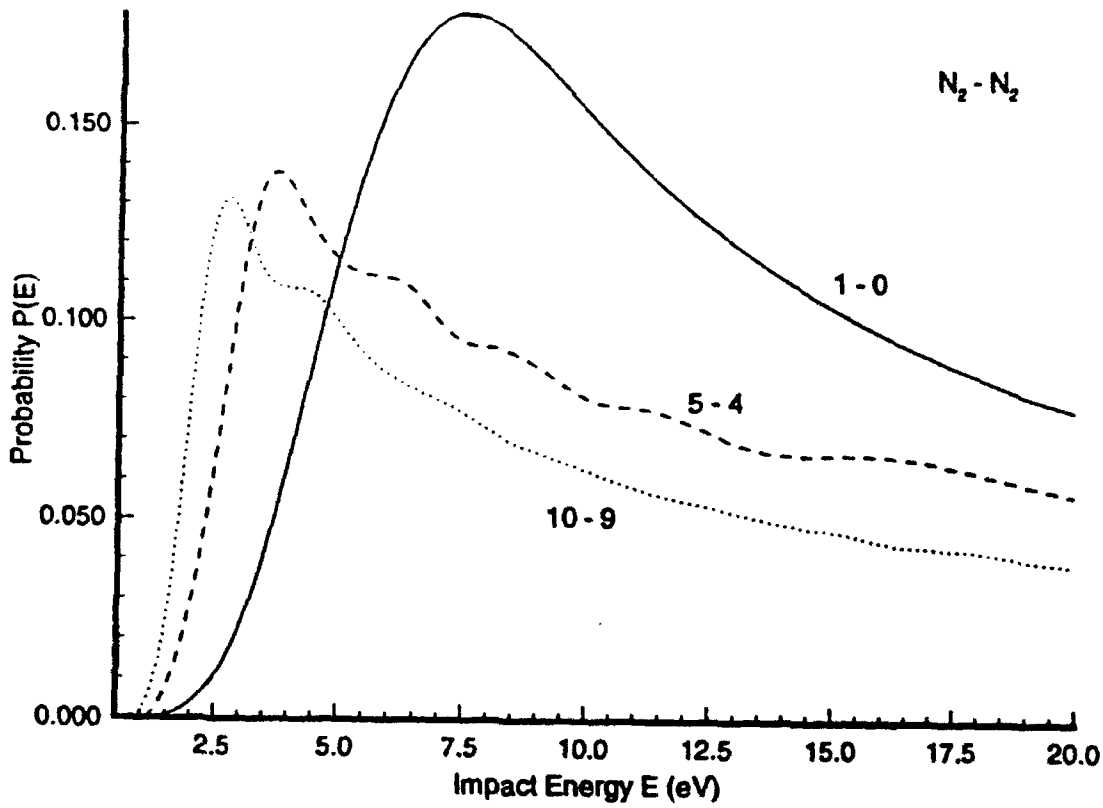

Fig.2

The transition probabilities $P_{vv'}(E)$ for the vibrational deexcitation of the target molecules resulting from the V-T energy transfer in the $N_2 + N_2(X^1\Sigma_g^+, v) \rightarrow N_2 + N_2(X^1\Sigma_g^+, v-1)$ collisions. The incident molecules are in the electronic ground states.

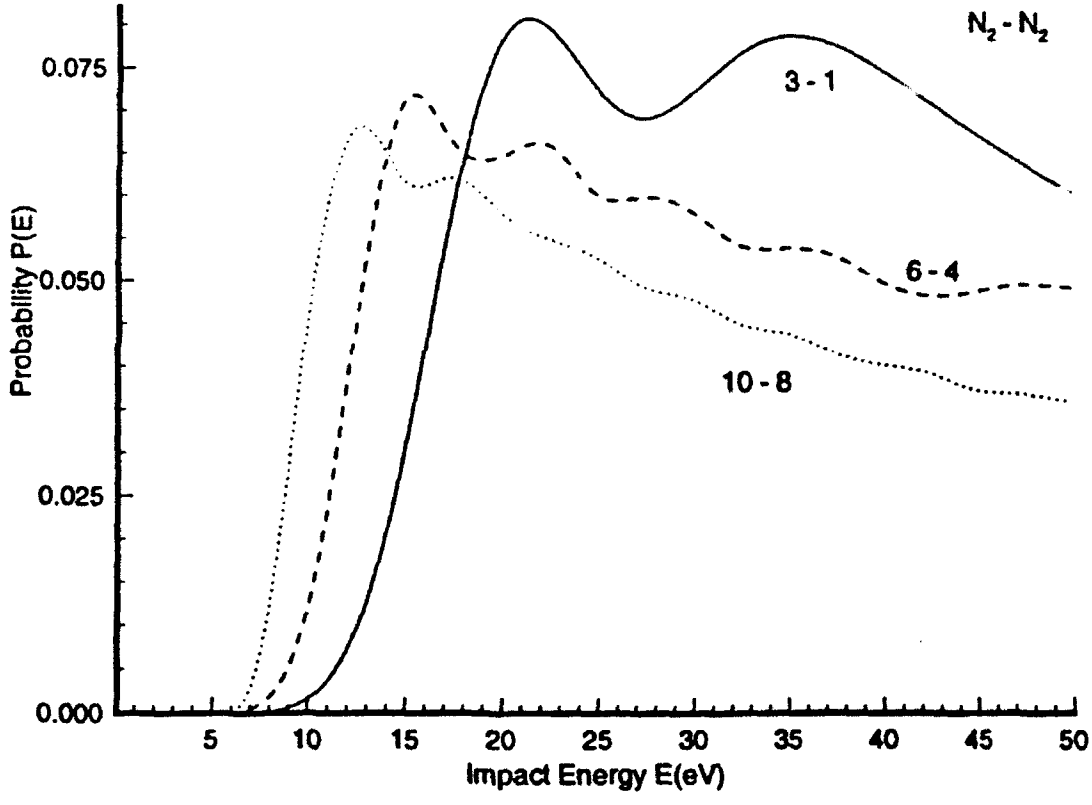

Fig.3

The transition probabilities $P_{vv'}(E)$ for the vibrational deexcitation of the target molecules resulting from the V-T energy transfer in the $N_2 + N_2(X^1\Sigma_g^+, v) \rightarrow N_2 + N_2(X^1\Sigma_g^+, v-2)$ collisions.

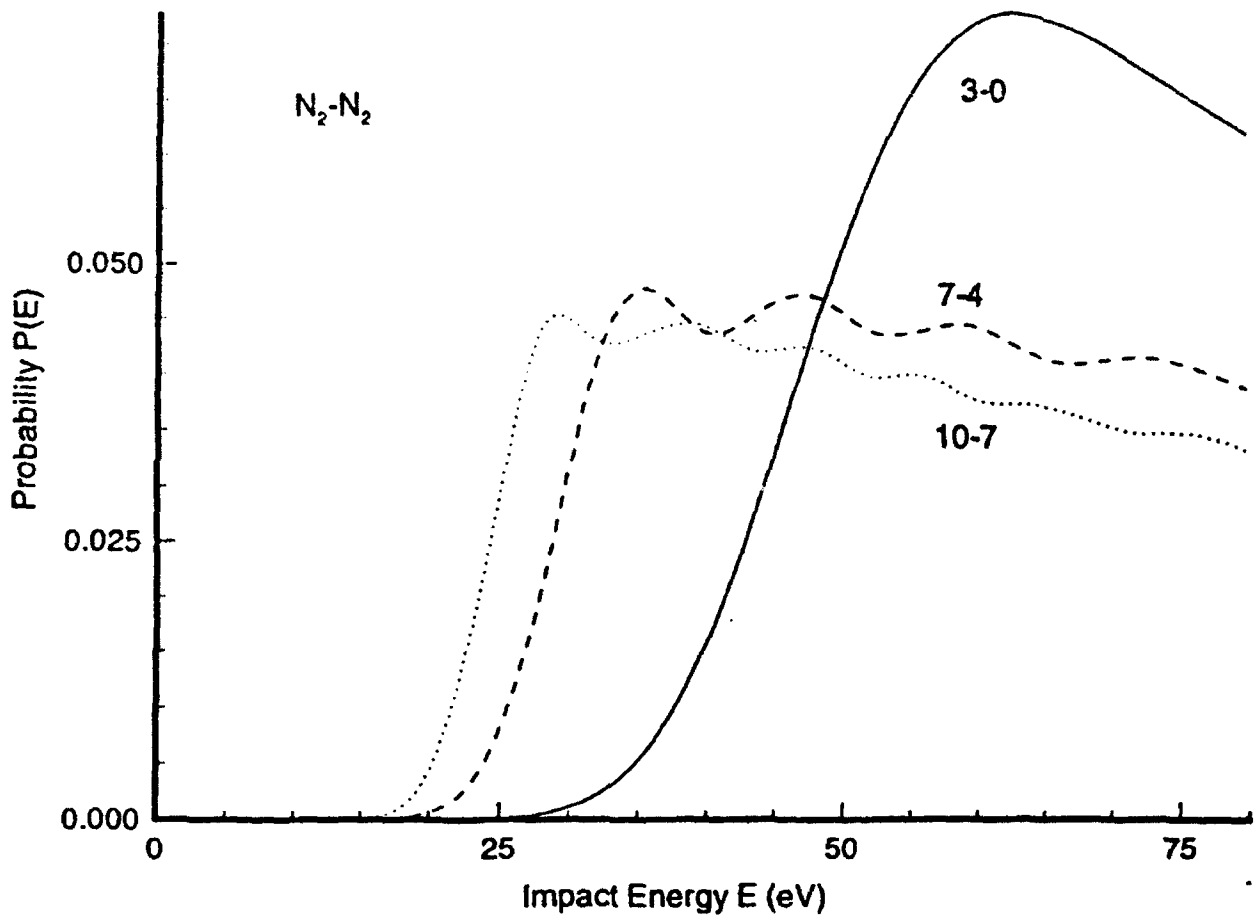

Fig.4

The transition probabilities $P_{vv'}(E)$ for the vibrational deexcitation of the target molecules resulting from the V-T energy transfer in the $N_2 + N_2(X^1\Sigma_g^+, v) \rightarrow N_2 + N_2(X^1\Sigma_g^+, v-3)$ collisions.

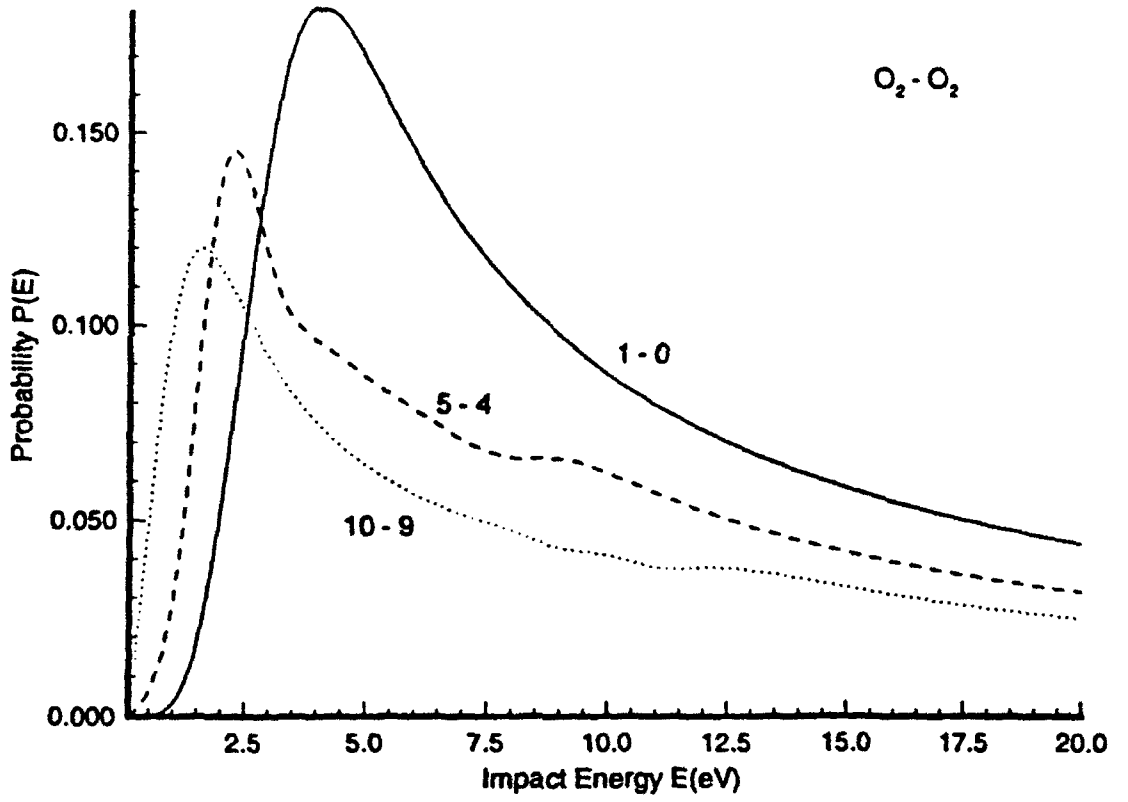

Fig.5

The transition probabilities $P_{vv'}(E)$ for the vibrational deexcitation of the target molecules resulting from the V-T energy transfer in the $O_2 + O_2(X^3\Sigma_g^-, v) \rightarrow O_2 + O_2(X^3\Sigma_g^-, v-1)$ collisions.

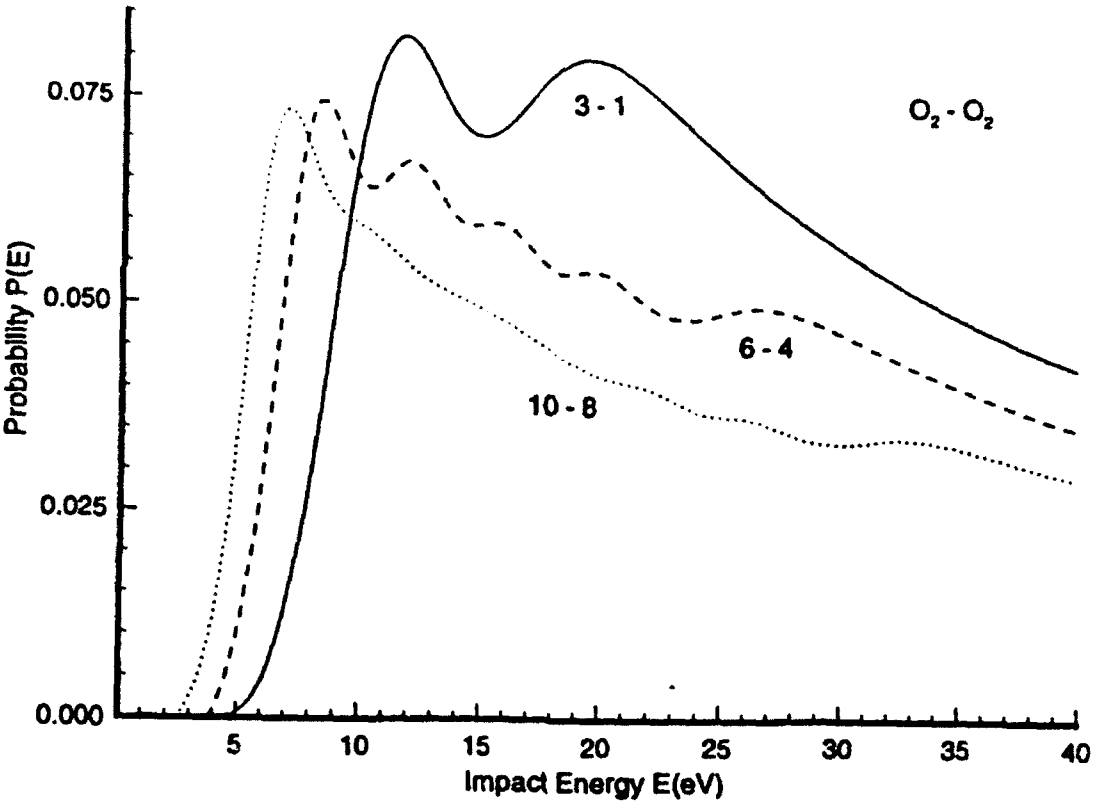

Fig.6

The transition probabilities $P_{vv'}(E)$ for the vibrational deexcitation of the target molecules resulting from the V-T energy transfer in the $O_2 + O_2(X^3\Sigma_g^-, v) \rightarrow O_2 + O_2(X^3\Sigma_g^-, v-2)$ collisions.

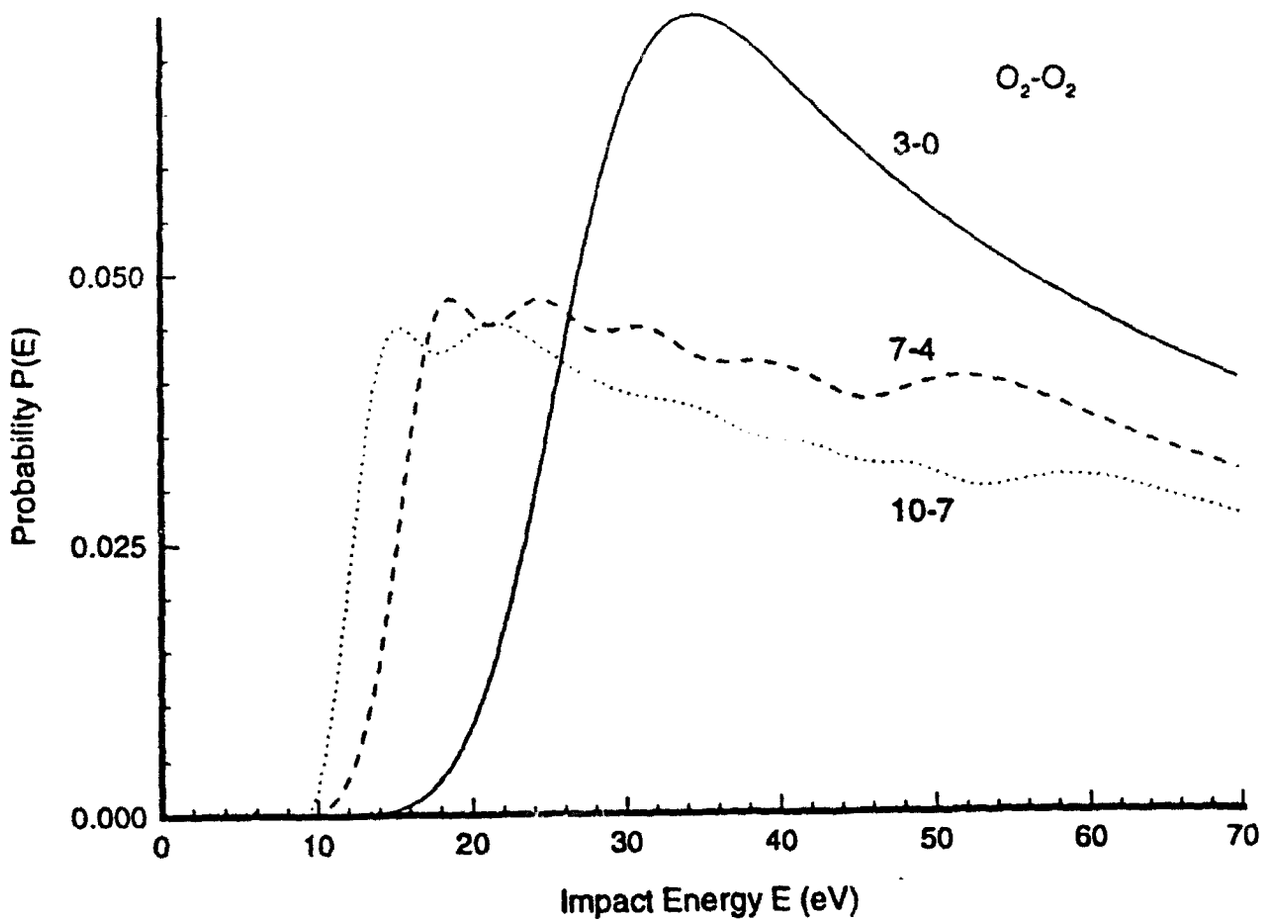

Fig.7

The transition probabilities $P_{vv'}(E)$ for the vibrational deexcitation of the target molecules resulting from the V-T energy transfer in the $O_2 + O_2(X^3\Sigma_g^-, v) \rightarrow O_2 + O_2(X^3\Sigma_g^-, v-3)$ collisions.

AIAA–94–2631

Rarefied Flow Testing in the 1990s: Measuring Those Phenomena that are Difficult to Calculate

E. P. Muntz, Iain Boyd, Andrew Ketsdever
Collaboration for Nonequilibrium Technologies (CNET)

an association of
Air Force Phillips Laboratory
Calspan-UB Research Center
Cornell University
Stanford University
University of Southern California

25th AIAA Plasmadynamics and Lasers Conference
June 20-23, 1994 / Colorado Springs, CO

Rarefied Flow Testing in the 1990s: Measuring Those Phenomena that are Difficult to Calculate

E. P. MUNTZ,*IAIN BOYD,†ANDREW KETSDEVER‡
Collaboration for Nonequilibrium Technologies (CNET)
an association of
Air Force Phillips Laboratory
Calspan-UB Research Center
Cornell University
Stanford University
University of Southern California

Abstract

Some experimental facilities and approaches that will be required for rarefied flow testing in the 1990s have been discussed. Because of the successful development of the DSMC technique and continuing increases in computer performance, rarefied flow testing will transition to be largely the study, development and validation of detailed collision models. The details of both surface interaction and gas-gas collision phenomena will be of great interest; not only for the traditional high speed flight problem but also for emerging applications in plasma chemistry, materials processing and microscale flows. Interestingly, there appears to be facilities available that can at least begin the work discussed here, although extensive instrumentation development needs to be pursued.

1 Introduction

Since the early 1960s rarefied flow testing has dealt with the study of nonequilibrium flow phenomena. Primary emphasis has been on non-reacting gas flows with and without vibrational and rotational nonequilibrium, as well as on idealized plasma flows. During the same period a remarkable computational gas dynamics technique, the Direct Simulation Monte Carlo method (DSMC) was pioneered by G. Bird [1] and developed by Bird and others. By 1990 it was clear that the DSMC technique could predict low temperature flows of monatomic gases with great precision. In many cases, particulary where surface interactions are not involved, the predictions are at least as accurate as can be measured (cf. Pham-Van-Diep et al. [2], Erwin et al. [3]). Lest one forget the importance of experiments amid computational

*Professor, Aerospace Engineering, University of Southern California, Fellow

†Assistant Professor, Mechanical and Aerospace Engineering, Cornell University, Member

‡Research Assistant, Aerospace Engineering, University of Southern California, Student Member

euphoria, note that the absolutely persuasive validation of DSMC was a spectacular comparison of experimental molecular velocity distribution functions in a hypersonic shock wave to predictions [2], illustrated here in Figs. 1 and 2.

The DSMC method, although computationally intensive, is inherently three dimensional as well as being time accurate if necessary; its usefulness in engineering applications has been expanding along with computer performance. Because the technique follows molecular motion and thus specifies the relative collision energies of reacting molecules, it has the potential for following nonequilibrium chemical processes with great precision. A capability that opens up such areas as; materials processing, plasma chemistry, coating techniques as well as other applications like the development of micromechanical devices.

One can compute non-reacting flows with some precision, and flows of rotationally and vibrationally active diatomic gases with sufficient accuracy for many engineering purposes. Dissociating, ionizing flows, as well as those where it is important to know the vibrational population distributions can be computed by the DSMC method but with unknown accuracy. Clearly, a major objective of rarefied flow testing in the 1990s will be to examine the accuracy of flow predictions where vibration coupled to nonequilibrium chemistry and ionization are important. It is interesting to note that relatively very efficient methods for predicting the results of energy dependent inelastic collisions are simultaneously emerging (Kunc, [4]; Kang and Kunc [5]), so that there is a growing possibility of providing the extensive base of necessary physical data for modeling reacting, nonequilibrium flows.

Two interesting results related to transport properties have recently been recognized but have yet to be widely accepted as major issues. One is the uncertainty associated with intermolecular potentials in energetic collisions (Pham-Van-Diep et al., [6]) and the other with the possibility of non-monatonic changes in transport properties as a function of temperature noted by Kang and Kunc [7] for dissociating iodine vapor.

Another area that is not well understood is surface interactions of energetic particles. They are of particular importance in material processing flows and plasma surface processing, requiring for accurate predictions a vast leap in our present understanding. Of equal uncertainty are high altitude phenomena in the shuttle glow category including contamination of sensitive satellite surfaces.

The remainder of this paper presents several examples of rarefied flow testing related to what we consider the important issues for the 1990s. Note that only in one of these examples is the facility that is used a more or less conventional air flow facility (a shock tunnel). This is really due to the anticipated continued growth in the capability of the DSMC technique, paralleling expected increases in computational performance. The combination of the DSMC technique and computational capability permits one to concentrate on validating suitably accurate physical models for the anticipated applications rather than be restricted to imperfect experimental simulations of flow phenomena.

2 Experimental Studies of Nonequilibrium Reacting Flows

Although the DSMC technique has in the past suffered from poor numerical performance, recent progress in computer hardware has to a large extent overcome this issue. Many

different implementations have been reported spanning vector [8], parallel [9], and scalar [10] machines. These advances have led to application of the method to an increasingly complex range of problems. The DSMC method may therefore be viewed as a very powerful framework in which it is now possible to consider implementation of more detailed physical models. Consideration is given in this section to the types of measurement that may assist in the development of more accurate collision models for the DSMC technique.

In addition, two experimental studies are described in this section, both of which are being pursued by the Collaboration for Nonequilibrium Technologies (CNET) and relate directly to investigating the accuracy of physical modeling in nonequilibrium flow fields.

2.1 DSMC Physical Models

As a first step, a brief review is given of the current state of direct verification against experimental data of DSMC models for various collisional phenomena. For the basic mechanism of elastic translational energy exchange, the simple models of Variable Hard Sphere (VHS) [11] and Variable Soft Sphere (VSS) [12] are available. Of these, VSS is probably the more useful as it is based on both viscosity and diffusion coefficients. More advanced collision models have been developed for specific applications. Perhaps the most noteworthy of these is the helium shock wave calculations of Pham-Van-Diep et al. [2]. A detailed analysis was performed of the collision dynamics of the helium atom. Comparison with experimental measurements of velocity distributions in strong shock waves gave excellent agreement. This study probably represents the most detailed verification of the DSMC technique undertaken to date. A clear conclusion from Ref. [2] is that including more physical detail in a DSMC simulation leads to more physically accurate results. This is the level of verification that should be the goal of future DSMC modeling efforts for all other inelastic collision mechanisms. The primary reason why such studies have not been undertaken is the almost complete lack of sufficiently detailed experimental measurements.

Modeling of rotational energy exchange has been studied for several gases including nitrogen [13]-[15], iodine [16], and hydrogen [17]. The simple models developed in these investigations were in each case compared with the available experimental data. Only in the case of nitrogen are there measurements of rotational energy distributions. Yet this is the level of detail required to develop advanced physical models. Comparison with these rotational energy distributions [15] indicated that the present simple models do not capture all of the detailed effects observed experimentally. In the iodine study [16], it was found that the rate of rotational relaxation was well simulated at relatively low temperature. At higher temperatures, however, the simple model gave a relaxation rate that was too high. This illustrates that rotational relaxation requires a more sophisticated approach and probably cannot be modeled using a single relaxation time. Almost certainly, this finding for iodine also applies to the molecular components in air.

Models for vibrational and chemical relaxation using the DSMC technique are in a rather poor state. There is almost no experimental data available in the literature to assist in development of these important phenomena. Simple models have been developed for vibrational relaxation [18], and chemistry [19, 20]. Without detailed measurements, however, it is not clear how successful these models are. To illustrate the type of experiment that would benefit

this area, we consider hypersonic flow of iodine over a 5 cm radius sphere. Flow conditions (listed in Table 1) are chosen to match those achievable in a test facility under development at USC. The free-stream Knudsen number is about 2×10^{-3} placing the flow in the near-continuum regime. Using a wall temperature of 500 K, the flow is computed using the DSMC technique. The models employed for viscosity and rotational energy exchange are described in Ref. [16]. The vibrational and dissociation models are described in Pham-Van-Diep et al. [21]. Profiles of density, temperature, and mole fraction are shown along the stagnation streamline in Figs. 3a–3c. Iodine has a very soft potential similar to the Maxwellian molecule. As shown in Fig. 3a, a thick, viscous shock wave is formed in front of the sphere. There is a distinct post-shock region before the density climbs again at the relatively cold surface. Figure 3b demonstrates that a strong degree of thermal nonequilibrium is predicted for this flow. The vibrational mode only equilibrates with translation and rotation as the wall is approached. Figure 1c shows that a significant degree of dissociation occurs. Indeed, the degree of dissociation of iodine under these flow conditions exceeds that predicted for nitrogen at much higher enthalpy in the LENS hypersonic facility [23].

From the modeling point of view, the measurements that would help validate the computations include rotational and vibrational temperatures, and molecular and atomic number densities. In presenting these DSMC calculations, very little confidence can be placed in the results without obtaining more accurate physical constants from experimental or theoretical studies. To illustrate how detailed measurements may help to develop advanced physical models, the vibrational energy distributions are computed at three points along the stagnation streamline at coordinates $x = -0.530$ (shock front), $x = -0.515$ (peak vibrational temperature) and $x = -0.501$ (near surface) as shown in Fig. 4abc. These distributions are compared with the Boltzmann distributions given by the macroscopic temperature computed by DSMC at each of the three locations (Fig. 4). It is immediately clear in each case that the DSMC vibrational energy distributions are very close to the Boltzmann form. This may be attributed to the use of a single vibrational relaxation time, and the use of Larsen-Borgnakke collision mechanics [24]. Detailed experimental measurements of the vibrational energy distributions through shocks such as that presented here are required to assess the validity of these simple models.

2.2 DSMC Resolution Limitations

In addition to the requirement for detailed experimental measurements of basic flow properties, there is a more general requirement for data to assist in the development of DSMC physical models for simulating trace species and rare collisional events. A good example of this is the BSUV series of flight experiments [22]. In these flights, the ultra-violet emission radiated by nitric oxide under conditions of hypersonic, high-altitude, thermochemical nonequilibrium was measured experimentally. Attempts to compute the radiation using both CFD and DSMC techniques have been successful up to an altitude of 80 km in the atmosphere. Beyond this altitude, the CFD predictions of emission are orders of magnitude lower than those measured in flight. At these higher altitudes, the degree of dissociation of nitrogen and oxygen is small. Consequently, the amount of NO produced in the flow is low. Thus, in a DSMC simulation employing one million particles, less than 10 NO particles

were produced. Hence, under these conditions, the DSMC technique does not predict any radiation.

This issue is essentially one of resolution and occurs whenever a particular species or collision mechanism that occurs infrequently has a major significance in determining the flow properties of interest. In the simulation, there must be a sufficient number of particles and collisions to resolve the species and mechanisms of most interest. Even with the advances in computer hardware, it will not always be possible to solve these problems just by increasing the total number of particles in a simulation. As described above, radiation is one example: however, there are many others. There is currently a great deal of interest in applying the DSMC technique to model gas flows in materials processing. In several of the candidates for thin-film growth and plasma etching, the processes involve use of low-pressure jets and beams that are essentially rarefied flows. These processes may involve thermal, rf discharge, or plasma sources. The role of chemical kinetics in these systems is of much greater significance than in aerodynamics. The production at a substrate of pre-cursors with well-specified energies is governed by the fluid mechanics and chemical kinetics of these flows. This places a strong emphasis on the kinetic models employed in any computation of these processes. In a similar way to high-temperature air, the kinetics constants for the systems of interest are not well understood. In addition, in many cases, the components of most interest are present only as trace species and the important chemical reactions occur infrequently. There is therefore a strong requirement for detailed measurement of some of the basic flow properties in these systems. Without the generation of such data, it may be difficult for the DSMC technique to make a real contribution in this area.

2.3 High Energy Air Flow Experiments

A program to study experimentally and computationally the flow is a large high energy shock tunnel, the CUBRC LENS facility, began last year. The flow about models will be studied with conventional instrumentation as well as PLIF (Hanson, [25]) and pulsed electron beam fluorescence (PEBF). Experiment design computations have been completed (Boyd et al., [26]) for shock tunnel stagnation and free stream conditions presented in Tables 2 and 3. The model was a sphere-cone with a 0.254 m nose diameter and a 10° half-angle. Details of the calculation are given in Boyd et al. [26]. Representative conditions in the flow field behind the shock wave are given for three stations in Table 4. The three stations are at the stagnation streamline (1) and positions 0.3 m (2) and 1.08 m(3) from the stagnation point measured along the centerline of the model. For the purposes of the present paper the feasibility of measuring vibrational level populations for N_2, O_2 and NO in the model flow field using PEBF are considered.

2.3.1 Pulsed electron beam fluorescence

Electron beam fluorescence (EBF) is a well established diagnostic technique for the study of hypersonic flows up to number densities around 10^{17} cm^{-3} and providing the flows are not strongly self-radiating [27]. The chief limitation of EBF has been that the electrons scatter at high gas densities and that the fluorescence emission is difficult to interpret due

to quenching in unknown quenching environments. Previously, Muntz, Kunc and Erwin [28] and Wojcik et al. [29] have investigated ways around both of these difficulties (Electron-Photon Fluorescence) by using a combination of an e-beam and laser photons. Cattolica [30] has reported on some experiments relative to the EPF concept and Wojcik et al. [29] on pulsed electron beam fluorescence (PEBF). We have come to the opinion that a high current, pulsed electron beam offers the most interesting approach. High current beams are self focusing so that they can partly negate scattering at higher densities. They retain the chief advantage of EBF which is the simultaneous broad-band excitation of all the rotational and vibrational internal energy states of all flow species and they can be coupled with gated detection to avoid quenching related interpretation difficulties as well as suppressing the importance of flow radiation.

High current pulsed e-beams can be generated by pseudosparks. Pseudospark devices [31, 32] operate on the left hand side of the Paschen minimum. The discharge prefers long path lengths and an axial discharge generating energetic electrons is produced. A typical pseudospark electron beam generator (after Frank [32]) is illustrated in Fig. 5. The discharge electrons are given enough ballistic energy to separate from the field lines at the device's exit and are observed to form a well collimated beam of electrons. The pulsed pseudospark discharge produces an electron beam with a relatively broad energy range, having a mean between 0.5 and 0.7 times the breakdown potential (Benker, [31]).

2.3.2 Pulsed e-beam installation in a shock tunnel

Since the pressure (*10–100* pa *depending on gas, geometry and desired* breakdown potential) in the pseudospark chamber is important care must be exercised for installations in gas dynamic facilities. Figure 6 shows a schematic of the pulsed electron gun (PEG) inside of a blunt cone model. The gatling diaphragm apparatus consists of a 0.0005 in thick mylar sheet which is sandwiched between two 3 in diameter steel plates (one of which is geared). These plates have 12, 0.2 in diameter holes around a 1.35 in radius circle (see Fig. 7). A PEG operating at 35 kV voltage and 1 kA current for approximately 10 ns has about 50 times the energy needed to vaporize a few mm diameter area of the mylar sheet. Gas in the facility does not have time to enter the PEG chamber before the e-gun firing sequence is complete (about 10 ns). After a discharge, a stepper motor can rotate the mylar sandwich to align the next orifice. The mylar membrane has three main functions. First, it effectively isolates the PEG from the test section gases until the gun is fired (tested to 1 atm pressure differential). Second, it allows for minimal time losses between calibration in the shock tunnel dump tank prior to a run and the actual run. Third, it reduces model between-run refurbishment time since each mylar cartridge is good for 12 discharges.

2.3.3 Calibration facility and preliminary results

A schematic of the calibration facility is shown in Fig. 8. The PEG, which operates at 35 kV on hydrogen, fires into a chamber containing the test gas. The subsequent fluorescence trace is captured using an RCA C3103A-02 photomultiplier tube (PMT) through a double .85m Spex spectrometer. The light from a small control volume in the calibration chamber

is focused through a combination of two lenses and a mirror onto the spectrometer entrance slit. The calibration was conducted by filling the chamber with helium or nitrogen gas to known pressures ranging from 5 to 180 mTorr, firing the PEG, and measuring the fluorescence signal at the appropriate wavelength. There was a complication, the PEG that was available produced inconsistent beams. Specifically, the beam wandered somewhat (approx. $\pm$ 0.5 cm). The problem does not lie with PEG technology, but rather with the specific version used in these initial experiments. Unfortunately, this complication forced us to substitute a drift tube for the gatling diaphragm apparatus, which caused the chamber pressure to be restricted to an upper limit of 180 mTorr, due to interference with gun operation from contamination of the discharge chamber by test gases. In addition, a commercially available Rogowski coil did not operate well in the electromagnetic interference environment created by the PEG. While we manufactured satisfactorily shielded coils for the purpose, subsequent temporary problems were encountered with their installation and no reliable current measurements are currently available. To obtain viable preliminary results, the gun was fired thirty-two times for each condition, and the results averaged by the digitizer to produce a representative signal vs. time trace. Signal averaging minimized the effect of pulse-to-pulse variations in beam current.

The averaged PMT output from the calibration experiments was recorded versus time at varying test gas pressures. These plots are displayed in Figs. 9 and 10. Figure 11 illustrates a qualitative linear trend between pressure (density) and integrated signal strength for both nitrogen and helium (the latter was chosen since it is one of the driver gases in the LENS facility). These results are only qualitative due to the lack of good current data. The curves in Figs. 9 and 10 are not self similar. This is the result of discharge trigger time complications caused by the drift tube. The lower chamber pressures seem to destabilize the trigger, thus the averaged traces have a broadened shape.

2.3.4 Signal levels in LENS experiments

We now consider applying PEBF to the nonequilibrium LENS flowfields assuming the 10° half-angle sphere-cone discussed earlier. Typical species concentrations and temperatures behind the shock wave are presented in Table 4. These are of course approximate; also, they do not represent properties in either the boundary or entropy layers.

Following Muntz and Erwin [33] and Muntz [27] the total population of an excited state k due to instantaneous excitation by a pulsed e-beam of current I_B and duration τ_B is

$$[N_k(v', J')]_{t=0} = 6.25 \times 10^{18} I_B \Omega_{d,k} n(v_1'', J_1'') \tau_B L \qquad (1)$$

where L is the length of emission observed along the beam's direction of propagation, $n_i(v_1'', J_1'')$ is the number density of a rotation-vibrational level of the ith species in the flow field and $\Omega_{l_2,k}$ is the excitation collision cross-section for beam electrons to bring the v_1'', J_1'' molecules in the initial electronic state l_1 to v', J' of an upper electronic state k, it is assumed that the transition can be approximated by $\Delta J = 0$. There is subsequent spontaneous emission to a lower electronic state l_2 designated by v_2'', J_2''.

The emission to l_2 is observed for a time τ_{OBS}. For the $[N_k]_{t=0}$ molecules generated by the e-beam, the number of photons emitted during τ_{OBS} for the transition $v' \rightarrow v_2''$ is

$$N_{PH} = [N_k(v', J')]_{t=0}(A_{k,l_2}(v', v_2'')/A_{k,l_2})(1 - e^{-A_{k,l_2}\tau_{OBS}}) \quad (2)$$

For this experiment it has been assumed that all emitted lines from the J' rotational level (typically $J_2'' = J^1 \pm 1, 0$) are not resolved. A_{k,l_2} is the spontaneous emission probability for k to l_2. $A_{k,l_2}(v', v_2'')$ is the product of the Franck-Condon factor for the v', v_2'' transition with A_{k,l_2}.

Using eqs. (1) and (2) typical numbers of emitted photons that provide information about a particular v_1'', J_1'' level can be estimated. The number densities listed in Table 4 need to be converted to approximate v_1'', J_1'' population. An examination of the N_2, O_2 and NO vibration and rotational partition functions indicates that a fractional populations of 0.005 and above for rotational levels will cover a significant proportion of the rotational population of each of these molecules even at the maximum temperature of 5000 K. Similarly a vibrational fractional population of 0.05 is appropriate. It is unlikely that observations will be made of single rotational lines, a more likely number is 10, thus the rotational partition function becomes effectively 0.05. The number density $n_i(v_1'', J_1'')$ is related to the total number density of species i through the normalized fractional populations P_R and P_V, or $n_i(v_1'', J_1'') = n_i P_R(J_1'')P_V(v_1'')$. Consider nitrogen, substitute into equation (1) for: the minimum N_2 number density from Table 4 of 8×10^{23} m^{-3}, the excitation cross-section $\Omega_{l_1,k} = 10^{-18}$ cm^2, $L = 1$ mm, $\tau_B = 10^{-8}$ s, $I_B = 10^3$ amps, $P_R = 0.05$ and $P_v = 0.05$. The resulting total number of excited state emitters become 1×10^{10}. With a τ_{OBS} of 10^{-8} s eq. (2) gives for a typical $A_{k,l_2}(v', v_2'')/A_{k,l_2} = 0.3$, $N_{PH} = 3 \times 10^7$. Assuming a reasonable optical system with an acceptance solid angle of 0.06 sr and detective quantum efficiency of 0.3, the number of statistically useful photons is 5×10^4.

For O_2 based on the results presented by Muntz [27] and Table 4 there will be about a factor of 50 decrease in emission. In this case the rotational structure will not be observable in detail, but certainly observations of vibrational population are feasible. The prospects for useful detection of NO do not appear particularly encouraging based on the results presented earlier by Muntz [27]. However this needs to be re-examined, since it depends on the issue of self-absorption for the resonance fluorescence that is excited by the e-beam.

2.4 Iodine Vapor Flows to Study Vibrational Population Distribution in Dissociating Gases

The need to examine nonequilibrium chemically reacting flows in detail and with precision has been the stimulus for developing an iodine vapor flow facility [34]. The CNET group is actively pursuing experiments in dissociating iodine vapor in the facility shown in Fig. 12. The facility operates at $T_0 = 1500$ K and 10 atm or below. Typical free stream conditions for one nozzle developed by Bradley [35] are shown in Table 1. The purpose for making an iodine vapor tunnel is to provide long test times compared to a typical shock tunnel so that detailed population distribution function measurements can be completed. The calculations for the flow around a sphere in this tunnel mentioned previously indicate some of the physical

information that can be obtained from the iodine experiments (cf. discussion in section 2.1). Preliminary results for a pilot scale version of the iodine tunnel have been recently reported (Boyd et al. [21]; Boyd et al. [17]; Pham-Van-Diep [36]).

3 Facilities for the Study of Energetic Interactions of Gases with Surfaces and Other Gases

The interactions of energetic gas phase particles with solid materials and other gases are important for a wide range of engineering disciplines. The physics of surface interactions is critical to the semi-conductor, materials processing and space science/engineering industries to name a few. For example, spacecraft which operate in low earth orbit (LEO), such as the Space Shuttle, Hubble Space Telescope and the space station, must be designed to withstand the adverse effects of oxygen atom material degradation of optical, structural, and electrical systems. The interactions between atmospheric gas species among themselves and other gas species such as outgassed molecules and rocket exhaust plume species are also of great interest. Gas-gas interactions at the surface of spacecraft are responsible for the phenomena known as shuttle glow [37]–[39]. Early observations of shuttle glow and material degradation caused by exposure to atmospheric atomic oxygen with relative energies near 5 eV and fluxes of about 10^{15} cm^{-2}-sec^{-1} caused the creation of several ground based facilities capable of producing energetic atomic species. Systems capable of reproducing LEO conditions are more adaptable, cost efficient and practical than dedicated satellite missions.

The Department of Aerospace Engineering at the University of Southern California in conjunction with the United States Air Forces' Phillips Laboratory has been developing a facility capable of producing a ground state, energetic O atom beam with energies and fluxes similar to those encountered in LEO [40, 41]. Figure 13 shows the general schematic of the energetic atomic beam facility at USC. Ion engine technology has been incorporated to produce a beam of energetic ions. Because the engine can be run on several gases, simulation of any atmospheric specie can be achieved. The ions are acceleated to the desired energy using electrostatic grids producing a well-collimated beam which is mass and energy selected using a Wien filter [42]. The atomic ions undergo a charge exchange process in molecular hydrogen (large cross-section, small scattering angle per collision) in the reaction

$$X^+ + H_2 \rightarrow X + H_2^+ \tag{3}$$

to produce energetic atoms. Energies upwards of 80 eV with continuous fluxes estimated around 10^{15} sec^{-1} should be easily achievable in this facility.

Several successful similar facilities have been developed. For example, Cross and Blais [43] employed the plasma formed by focusing a c-w CO_2 laser beam in a rare-gas/oxygen mixture. The laser sustained the spark-initiated plasma which flowed through a hydrodynamic expansion nozzle producing an atomic beam of neutral species. Flux densities of 10^{17} cm^{-2}–sec^{-1} of atomic oxygen were measured at the target material sample; however, there was no way to remove the unwanted energetic rare-gas component of the beam before impacting the sample. Another system developed by Physical Sciences, Inc. [44, 45] uses a laser to induce breakdown in a high pressure O_2 region at the throat of an expansion nozzle.

The plasma formed at the nozzle throat continues to absorb radiation as long as the laser is on (pulse width of 2.5 μsec) and extends down the nozzle as a blast wave dissociating the molecular oxygen. Energies of 5.3 eV $\pm$ 3% have been achieved with approximately 10^{18} atoms per laser pulse at 3 Hz operation. Diagnostics of the beam suggests that the resulting beam is 80% dissociated with less that 17% ionization and about 1% metastable population.

The success of the facilities creating energetic atmospheric species (in the long run certainly not only O atom) will depend on some experimental specification of the incident and reflected particles. As the facility technology matures significant contributions on both surface scattering and gas on gas interaction are anticipated. Although they do not necessarily look like typical flow facilities, they will in fact be very important to rarefied flows due to the availability of the DSMC technique.

4 Summary

Some experimental facilities and approaches that will be required for rarefied flow testing in the 1990s have been discussed. Because of the successful development of the DSMC technique and continuing increases in computer performance, rarefied flow testing will transition to be largely the study, development and validation of detailed collision models. The details of both surface interaction and gas-gas collision phenomena will be of great interest; not only for the traditional high speed flight problem but also for emerging applications in plasma chemistry, materials processing and microscale flows. Interestingly, there appears to be facilities available that can at least begin the work discussed here, although extensive instrumentation development needs to be pursued.

Acknowledgments

The authors would like to thank Jerome Maes for skillfully stitching email traffic into a paper. Fred Lutfy and John Schilling were responsible for the pulse e-beam results. The work was supported by the Air Force Phillips Laboratory (A. Ketsdever—Palace Knight program) and the Air Force Office of Scientific Research under University Research Initiative F49620–93–0373 with Julian Tishkoff as grant monitor.

References

[1] Bird, G. A. *Molecular Gas Dynamics and the Direct Simulation of Gas Flows*, Clarendon Press, Oxford, 1994.

[2] Pham-Van-Diep, G. C. Erwin, D. A., Muntz, E. P. "Nonequilbrium Molecular Motion in a Hypersonic Shock Wave," *Science*, 245, p. 624, 1989.

[3] Erwin, D. A., Pham-Van-Diep, G. C., Muntz, E. P., "Nonequilibrium Gas Flows I: A Detailed Validation of Monte Carlo Direct Simulation for Monatomic Gases," *Physics of Fluids A*, 3 (4), p. 697, 1991.

[4] Kunc, J. A. "Vibration-Translation Exchange in Diatom-Diatom Collisions," J. Phys. B: At. Mol. Opt. Phys., 24, p. 3741, 1991.

[5] Kang, S. H., Kunc, J. A., "Energy Dependence of Vibration-Translation Transitions in Collisions of Neutral Particles," AIAA Paper 94–2403, June 1994.

[6] Pham Van Diep, G. C., Muntz, E. P., Erwin, D. A., "A Study of Microkinetic Adjustments Required to Match Shock Wave Experiments and Monte Carlo Direct Simulation for a Wide Mach Number Range," AIAA Paper 90–1689, 1990.

[7] Kang, S. H., Kunc, J. A., "Viscosity of High-Temperature Iodine," *Phys. Rev. A*, 4, (6), p. 3596, 1991.

[8] Boyd, I. D., "Vectorization of a Monte Carlo Method for Nonequilibrium Gas Dynamics," *Journal of Computational Physics*, 96, p. 411, 1991.

[9] McDonald, J. D., "Particle Simulation in a Multi-Processor Environment," AIAA Paper 91–1366, June 1991.

[10] Dietrich, S. and Boyd, I. D. "A Scalar Optimized Parallel Implementation of the DSMC Technique," AIAA Paper 94–0355, January 1994.

[11] Bird, G. A., "Monte Carlo Simulation in an Engineering Context," in Rarefied Gas Dynamics, edited by Sam S. Fisher, Volume 74 of Progress in Astronautics and Aeronautics, Part I, AIAA, New York, p. 239, 1981.

[12] Koura, K. and Matsumoto, H., "Variable Soft Sphere Molecular Model for Inverse-Power-Law or Lennard-Jones Potential," *Physics of Fluids A*, 4, p. 2459, 1991.

[13] Boyd, I. D. "Rotational-Translational Energy Transfer in Rarefied Nonequilibrium Flows," *Physics of Fluids A*, 2 (3), p. 447, 1990.

[14] Boyd, I. D., "Temperature-Dependence of Rotational Relaxation in Shock-Waves of Nitrogen," *Journal of Fluid Mechanics*, 246, p. 343, 1993.

[15] Boyd, I. D., "Relaxation of Discrete Rotational Energy Distributions Using a Monte Carlo Method," *Physics of Fluids A*, 5, p. 2278, 1993.

[16] Boyd, I. D., Pham-Van-Diep, G.C., and Muntz, E.P., "Monte Carlo Computation of Nonequilibrium Flow in a Hypersonic Iodine Windtunnel," *AIAA Journal*, 32, p. 964, 1994.

[17] Boyd, I. D., Cappelli, M.A., and Beattie, D.R., "Monte Carlo Computation of Nozzle and Plume Flows of a Low-Power Hydrogen Arcjet," AIAA Paper 93–2529, June 1993.

[18] Boyd, I. D., "Analysis of Vibrational-Translational Energy Transfer Using the Direct Simulation Monte Carlo Method," *Physics of Fluids A*, 3 (7), p. 1785, 1991.

[19] Haas, B. L. and Boyd, I. D., "Models for Direct Monte Carlo Simulation of Coupled Vibration-Dissociation," *Physics of Fluids A*, 5, p. 478, 1993.

[20] Marriott, P. M. and Harvey, J. K., "New Approach for Modelling Energy Exchange and Chemical Reactions in the Direct Simulation Monte Carlo Method," Rarefied Gas Dynamics, Ed. A. E. Beylich, VCH, Weinheim, 1991, p. 784.

[21] Pham-Van-Diep, G. C., Muntz, E. P., and Boyd, I. D., "Measurement of Vibrational Population Distributions in a Free-Jet Flow of Chemically Reacting Iodine Vapor and Comparisons With Monte Carlo Predictions," AIAA Paper 93–2996, July 1993.

[22] Candler, G. V., Boyd, I. D., et al., "Continuum and DSMC Analysis of Bow Shock Flight Experiments," AIAA Paper 93–0275, January 1993.

[23] Boyd, I. D., Srinivasan, A., Muntz, E. P., Hanson, R. K., and Holden, M. S., "Thermochemical Nonequilibrium Design Calculations for Hypervelocity Experiments in the

LENS Facility," AIAA Paper 94–2097, June 1994.

[24] Borgnakke, C. and Larsen, P. S., "Statistical Collision Model for Monte Carlo Simulation of Polyatomic Gas Mixture," *Journal of Computational Physics*, 18, p. 405, 1975.

[25] Hanson, R. K., Seitzman, J. M., Paul, F. H., "Planar Laser Induced Imaging and Combustion Gases," *Applied Physics B*, 50, p. 441, 1989.

[26] Boyd, I. D., Holden, M. S., Muntz, E. P., Hanson, R. K., "Thermochemical Nonequilibrium Design Calculations for Detailed Hypervelocity Experiments in LENS Facility," AIAA Paper 94–2403.

[27] Muntz, E. P., "The Electron Beam Fluorescence Technique," AGARDograph 132.

[28] Muntz, E. P., Kunc, J. A., Erwin, D. A., "A Pulsed Electron-Photon Fluorescence Technique for Temperatures and Specie Concentration Measurement at Points in Relatively Dense, Unseeded Air Flow," AIAA Paper 87–1526, January 1987.

[29] Wojcik, R., Schilling, J. N., Erwin, D. A., "Rarefied Flow Diagnostics Using Pulsed High-Current Electron Beams," AIAA Paper 90–1515, January 1990.

[30] Cattolica, R. J., "Modern Developments in Electron-Beam Fluorescence," Rarefied Gas Dynamics, ed. A. Beylich, VCH, Weinheim, p. 1552.

[31] Benker, W., Christensen, J., Frank, K., Gundel, H., Hartmann, W., Redel, T., Steller, M., "Generation of Intense Electron Beam by the Pseudospark Discharge," *Plasma Science*, 17, p. 754, 1989.

[32] Frank, K., Christensen, J., "The Fundamentals of the Pseudospark and its Applications," *Plasma Science*, 17, p. 748, 1989.

[33] Muntz, E. P., Erwin, D. A., "Rapid Pulse Electron Beam Fluorescence for Flow Field Diagnostics," in New Trends in Instrumentation for Hypersonic Research, ed. A. Boulier, p. 265, NATO ASI Series, Series E: Applied Sciences—Vol. 21, Kluwer, Dordrecht, 1993.

[34] Pham-Van-Diep, G. C. Muntz, E. P., Weaver, D. P., Dewitt, T. G., Bradley, M. K., Erwin, D. A., Kunc, J. A., "An Iodine Hypersonic Wind Tunnel for the Study of Nonequilibrium Reacting Flows," AIAA Paper 92–0566.

[35] Bradley, M. K., "Flow Models for the Design of a Hypersonic Iodine Vapor Wind Tunnel Nozzle with Chemical and Vibrational Nonequilibrium Effects," Ph.D. Thesis, University of Southern California, 1994.

[36] Pham-Van-Diep, G. C., Chemically Reacting, Hypersonic Flows of Iodine Vapor for the Study of Nonequilibrium Phenomena in Diatomic Gases," Ph.D. Thesis, University of Southern California, 1993.

[37] Mende, S. B., Garriott, O. K., Banks, P. M., "Observations of Optical Emissions on STS-4," *Geophys. Res. Letts.* 10 (2), p. 122, 1983.

[38] Hunton, D. E., "Shuttle Glow," *Scientific American*, 92, November 1982.

[39] Yee, J. H., Abreu, V. J., "Visible Glow Induced by Spacecraft-Environment Interaction," *Geophys. Res. Letts.*, 10 (2), p. 126, 1983.

[40] Ketsdever, A. D., Weaver, D. P., Muntz, E. P., "An Inertially Tethered Hydrogen Charge Exchanger for the Production of 5–30 eV O Atoms," AIAA Paper 92–2931, 1992.

[41] Ketsdever, A. D., Weaver, D. P., Muntz, E. P., "A Molecular Hydrogen Ring Jet Charge Exchanger for the Production of Energetic Oxygen Atoms," AIAA Paper 94–0371, 1994.

[42] Teal-Quiros, E., Prelas, M., "New Tilted-Poles Wien Filter with Enhanced Perfor-

mance," *Rev. Sci. Instrum.*, 60 (3), p. 350, 1989.

[43] Cross, J. B., Blais, N. C., "High Energy/Intensity CW Atomic Oxygen Beam Source," in RGD eds. Muntz, Weaver, D. H. Campbell, *Prog. in Aero. and Astro.*, Vol. 116, AIAA, Washington, D. C., 1989.

[44] Caledonia, G. E., Krech, R. H., Green, B. D., "A High Flux Source of Energetic Oxygen Atoms for Material Degradation Studies," *AIAA Journal*, 25 (1), p. 59, 1987.

[45] Caledonia, G. E., Krech, R. H., Upschulte, B. L., Sonnenfroh, D. M., Oakes, D. B., and Holtzclaw, K. W., "Fast Oxygen Atom Facility for Studies Related to Low Earth Orbit Activities," AIAA Paper 92-3974, 1992.

Table 1: Iodine Vapor Hypersonic Tunnel Free Stream Conditions.
(after Bradley [35])

Density	1.46×10^{-3} kg/m^3
Temperature	180 K
Mach Number	8.2
Degree of Dissociation	0.023

Table 2: LENS operating parameters.
(private communication with D. Boyer)

T_0	6000 K
p_0	1500 atm
throat diameter	0.057 m

Table 3: Free stream flow conditions representing an altitude of 24.5 km.
(private communication with D. Boyer)

ρ_∞ (kg/m^3)	4.4×10^{-2}
T_∞ (K)	881
u_∞ (km/s)	4.12
M_{N_2} (mass fraction)	0.720
M_{N_2}	0.223
M_{NO}	0.0565
M_O	0.00074

Table 4: Representative behind shock properties.
(after Boyd et al. [26])

Station	Species	No. Density (#/m^3)	T_v K	T_R K
1	N_2	$6 \cdot 10^{24}$	5000	5000
	O_2	$2 \cdot 10^{23}$	5000	5000
	O	$3 \cdot 10^{24}$	5000	5000
	NO	$5 \cdot 10^{23}$	5000	5000
2	N_2	$1 \cdot 10^{24}$	3400	2800
	O_2	$2 \cdot 10^{23}$	3400	2800
	O	$2 \cdot 10^{23}$	3400	2800
	NO	$1 \cdot 10^{23}$	3400	2800
3	N_2	$8 \cdot 10^{23}$	2600	2700
	O_2	$2 \cdot 10^{23}$	2600	2700
	O	$8 \cdot 10^{22}$	2600	2700
	NO	$6 \cdot 10^{22}$	2600	2700

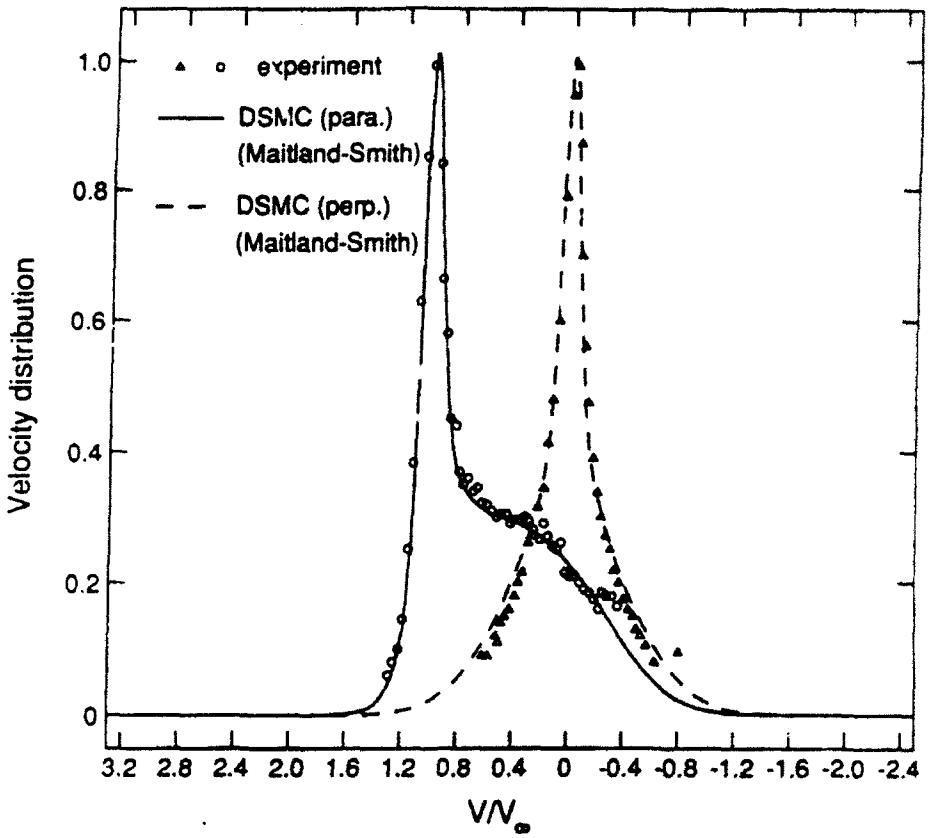

Figure 1: Predicted and experimental molecular motion parallel (para) and perpendicular (perp) to the flow in a Mach 25 normal shock wave in helium about one-third of the way through the shock (at a density $n/n_\infty = 0.285$).

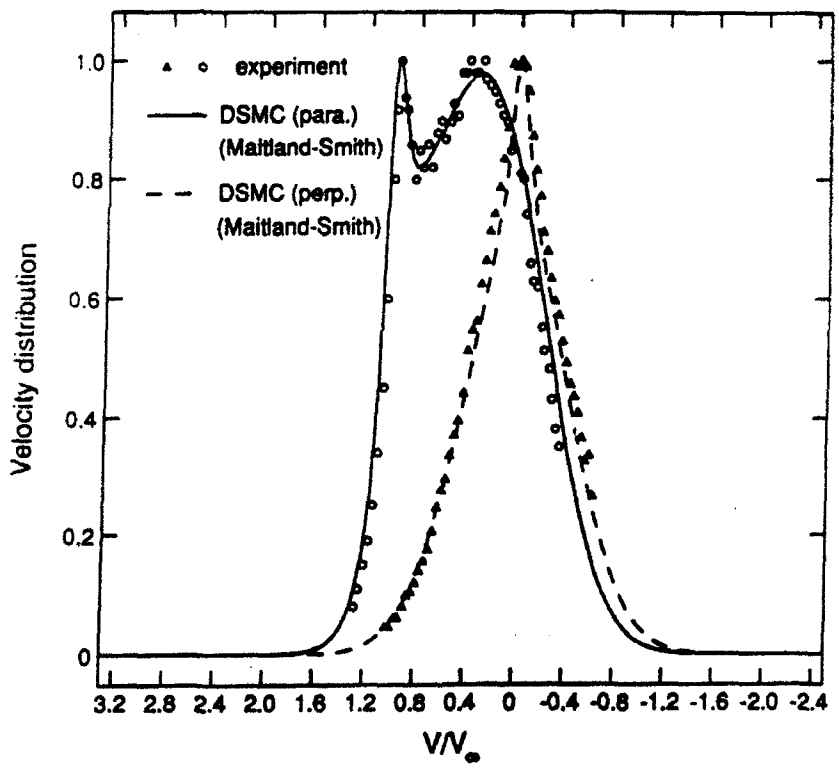

Figure 2: Predicted and experimental molecular motion as in Fig. 1 but slightly more than half-way through the shock (at a density $n/n_\infty = 0.565$).

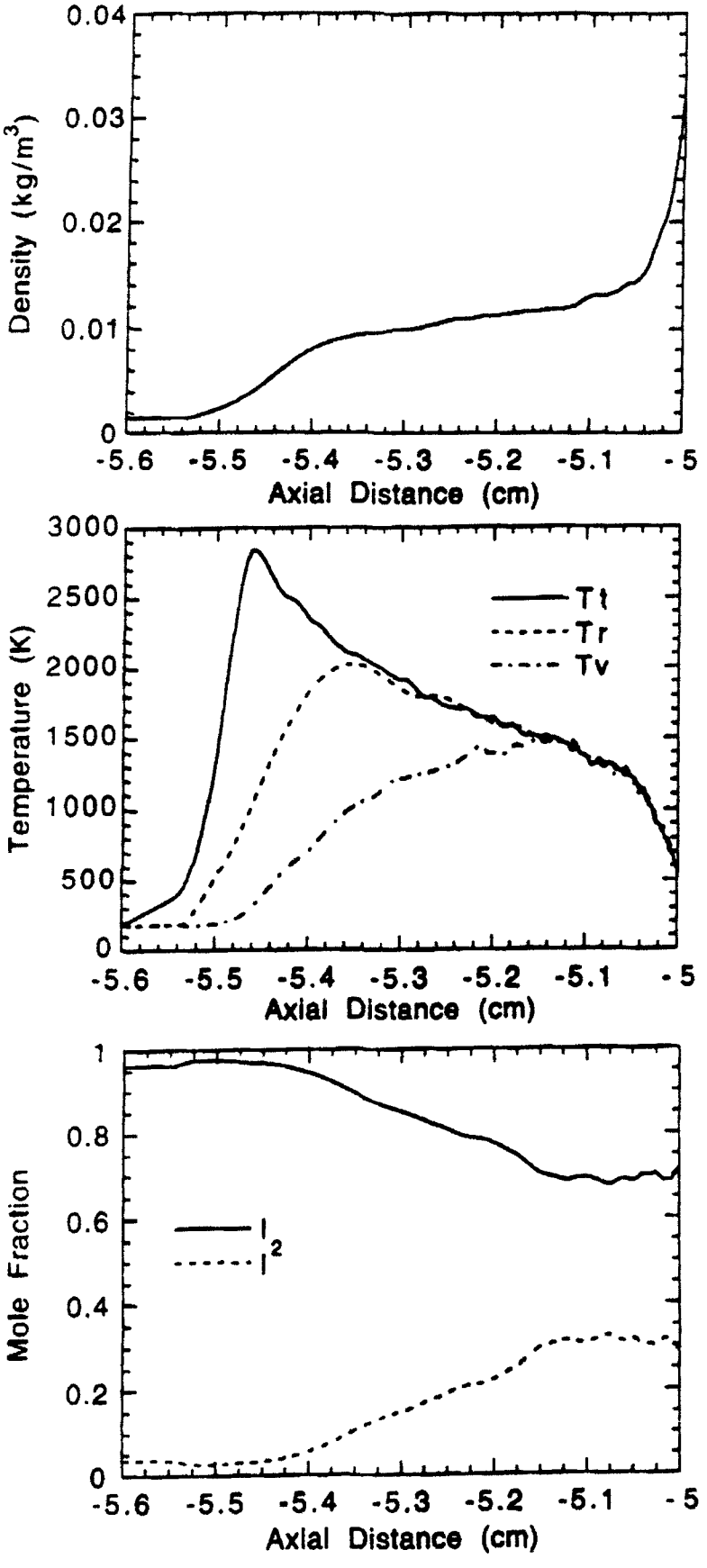

Figure 3: Conditions along the stagnation streamlines of a 10 cm diameter sphere in iodine vapor flow provided in Table 1.

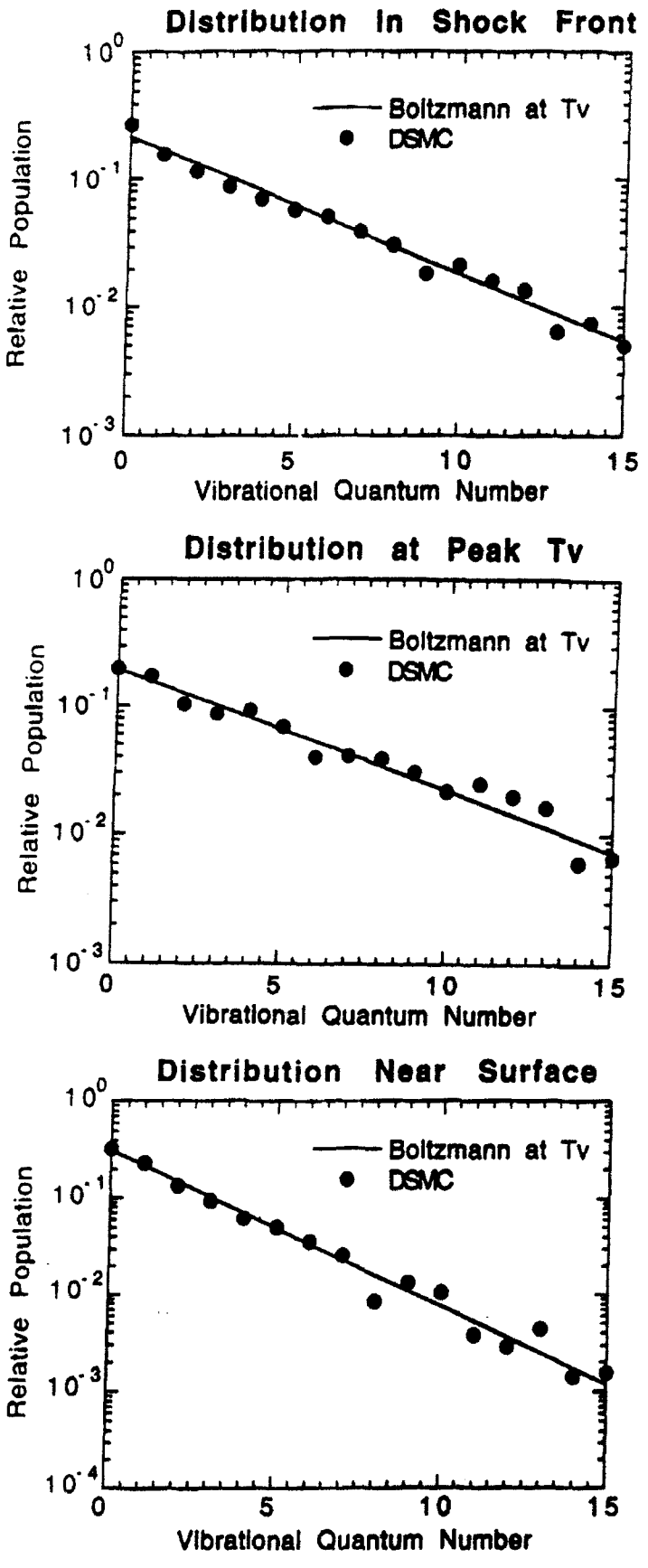

Figure 4: Population of vibrational levels at three positions along stagnation streamlines for the same flow as in Fig. 3.

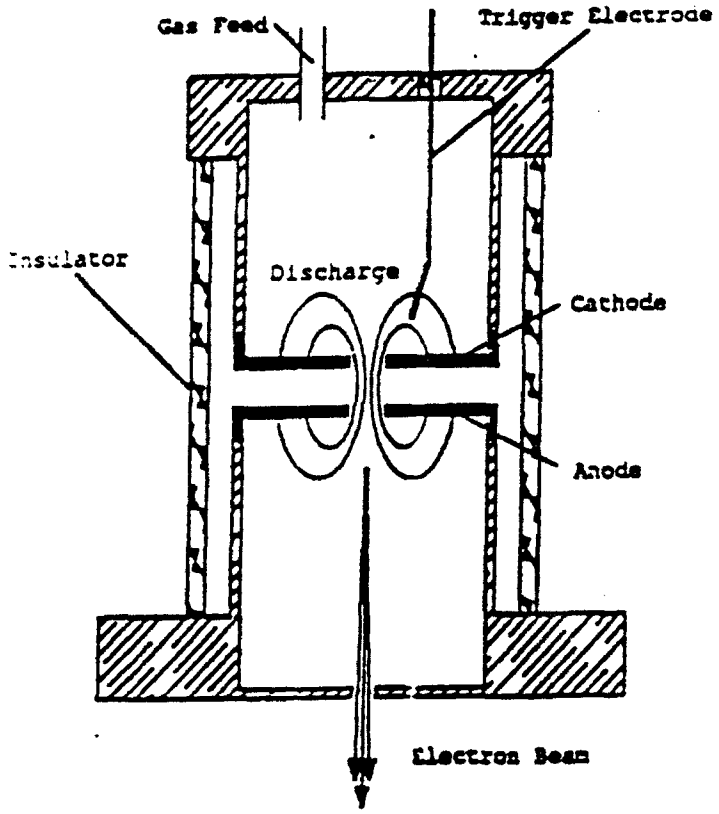

Figure 5: Pseudospark pulsed electron gun used in preliminary calibration experiments.

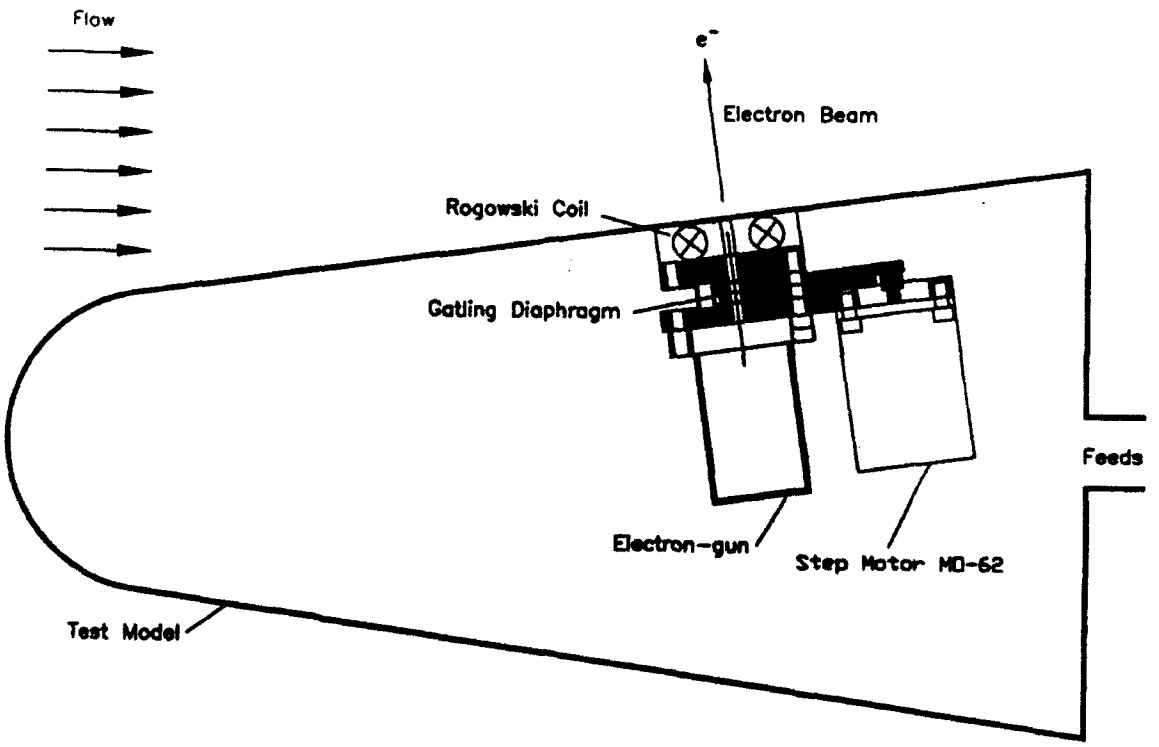

Figure 6: Pulsed electron gun installation inside blunt cone model.

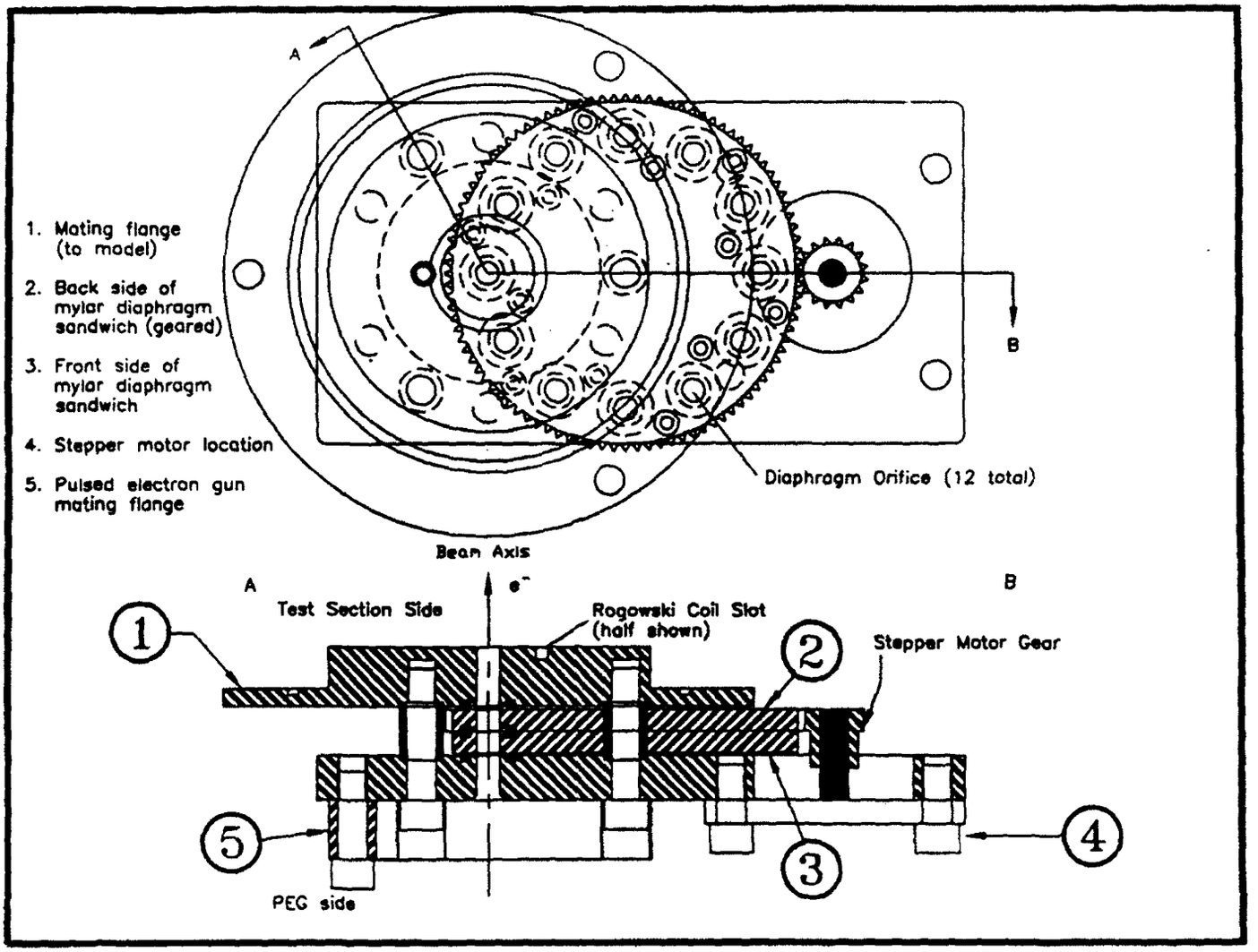

Figure 7: Gatling diaphragm with evaporative windows for pulsed electron gun.

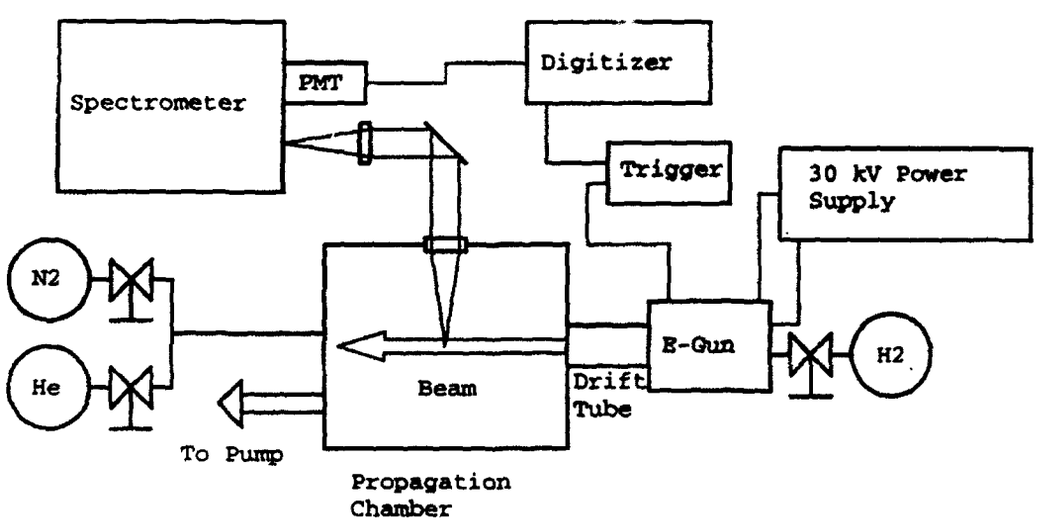

Figure 8: Calibration facility schematic.

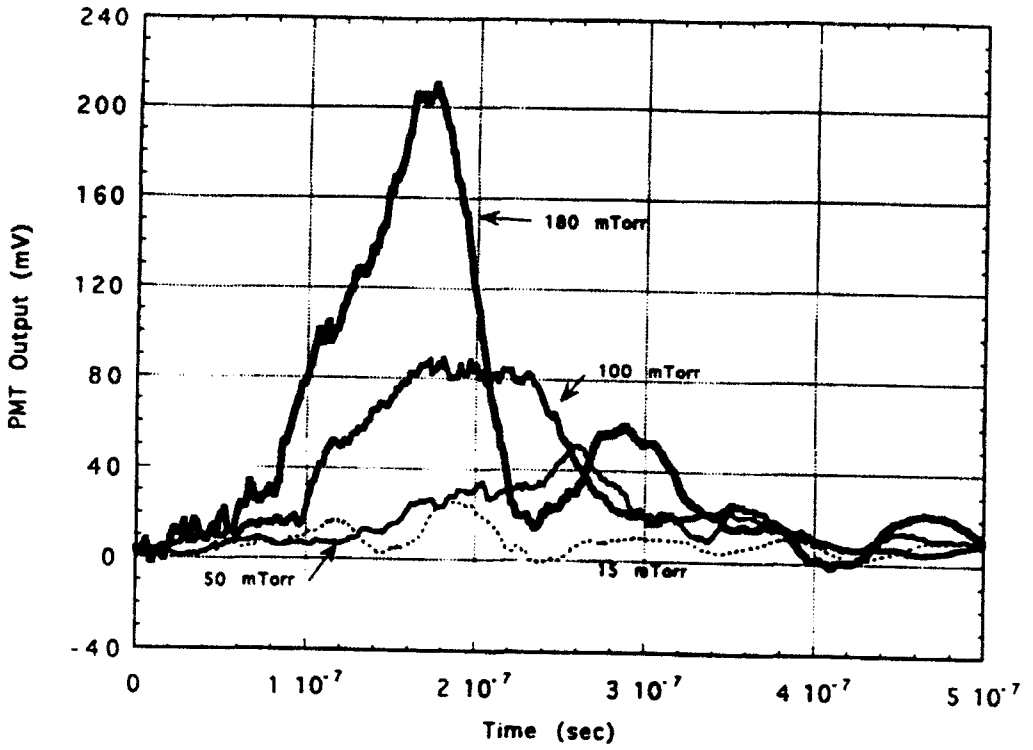

Figure 9: Averaged photomultiplier outputs (50 Ω termination) for four helium pressures, observation of $2'S$-$3'P$ line (5016 A).

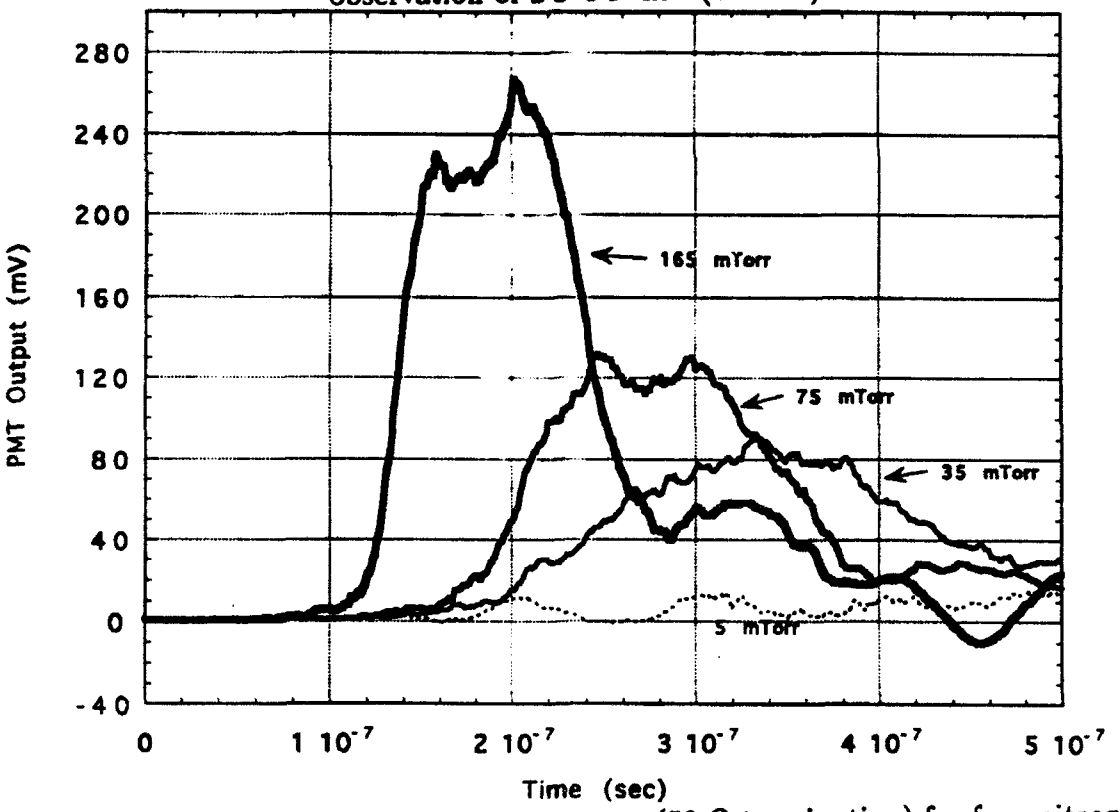

Figure 10: Averaged photomultiplier outputs (50 Ω termination) for four nitrogen pressures, observation of $X^2\Sigma - B^2\Sigma$. 0,0 band of first negative system.

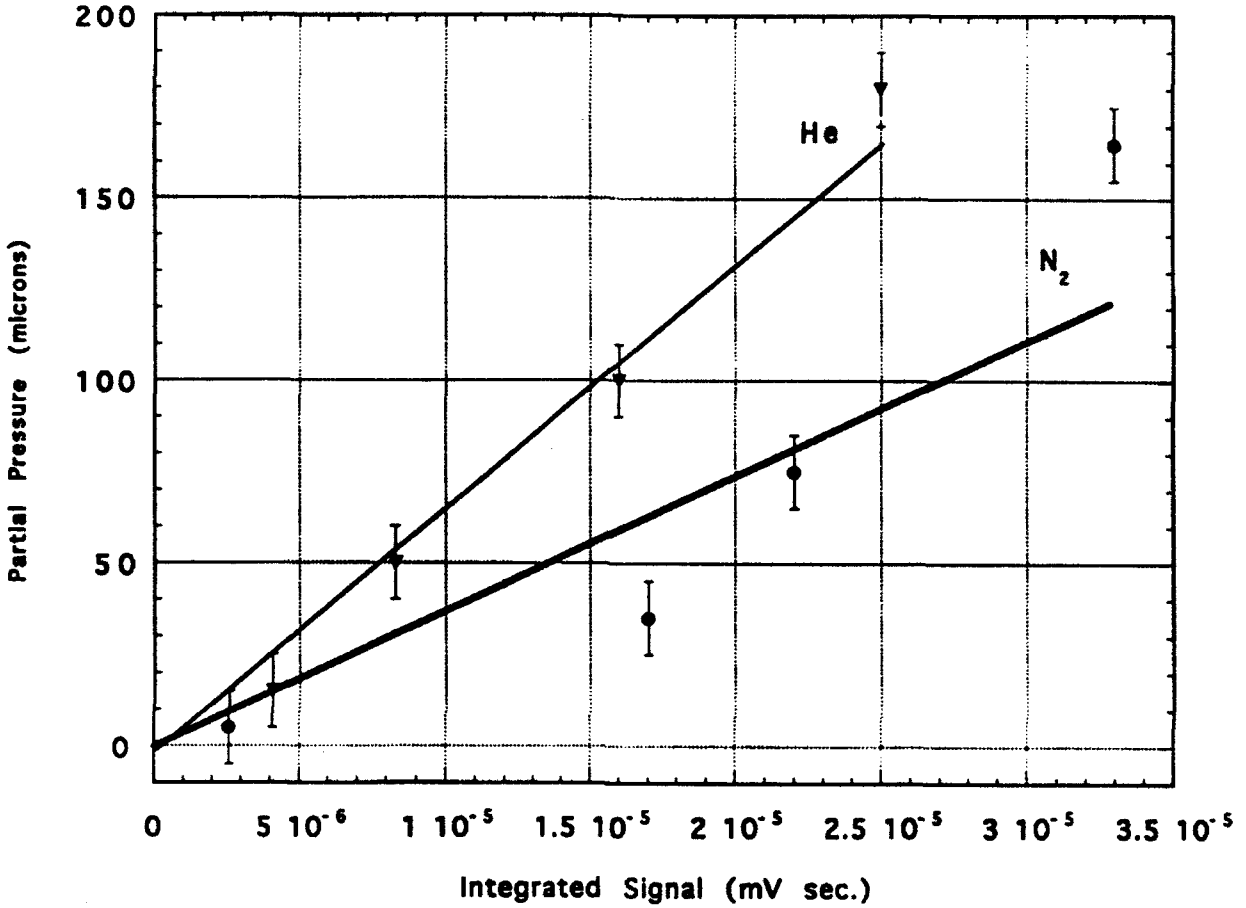

Figure 11: Total integrated signals from two previous figures versus pressure for He and N_2.

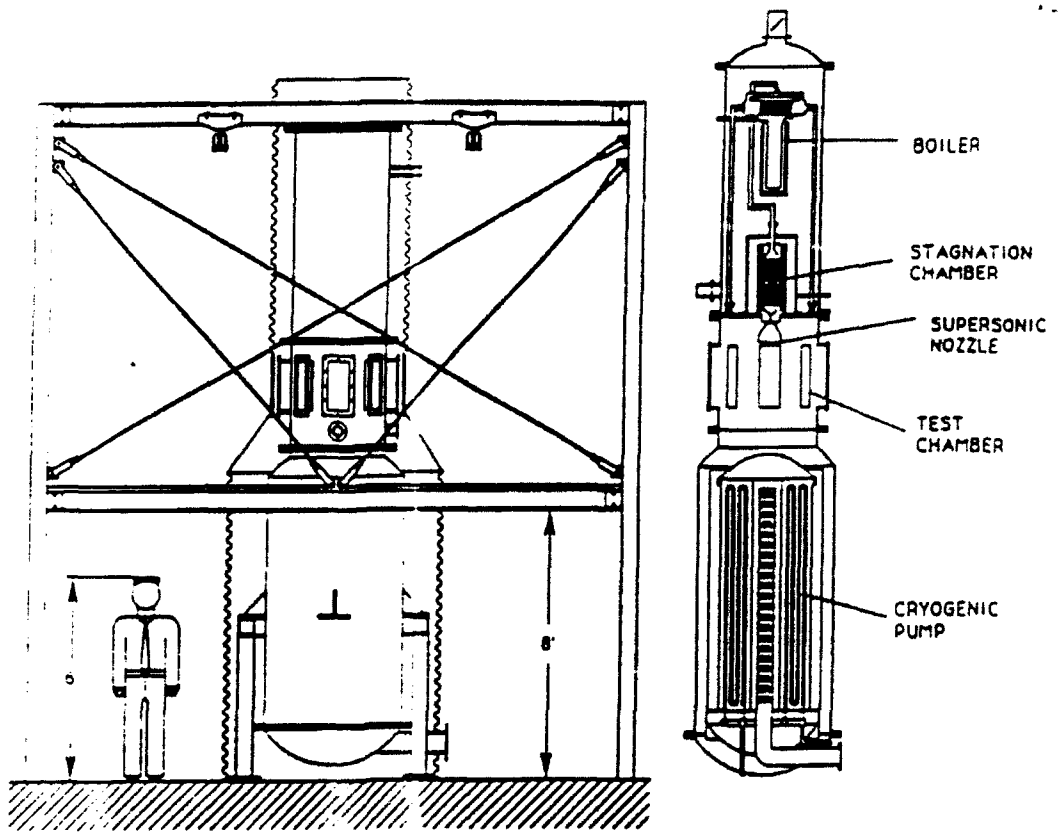

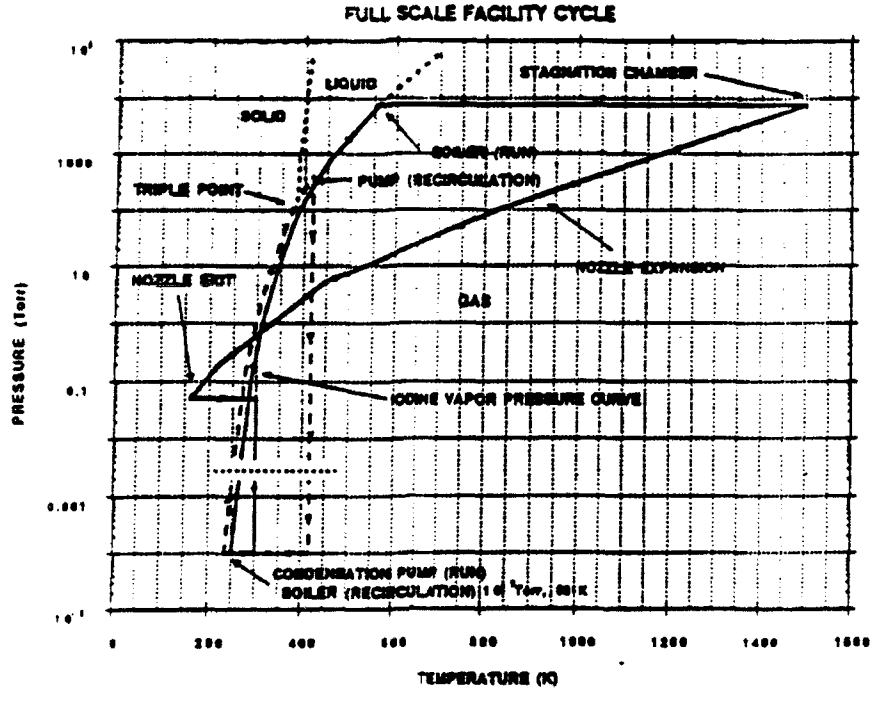

Figure 12: Iodine vapor hypersonic flow facility, 30 min run time, flow conditions given in Table 1.

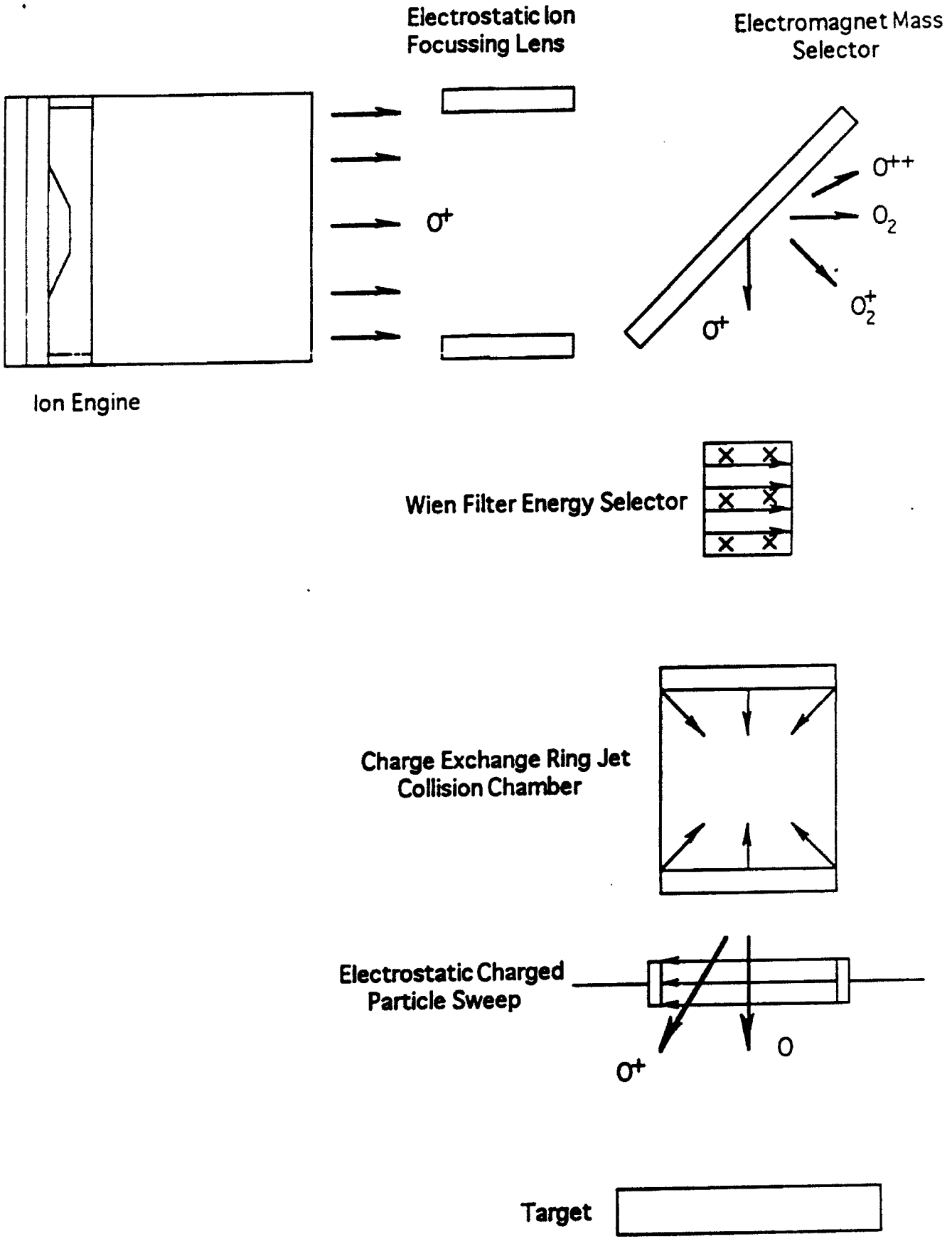

Figure 13: Oxygen atom production facility schematic.

AIAA-94-2097

Thermochemical Nonequilibrium Design Calculations for Detailed Hypervelocity Experiments in The LENS Facility

I. D. Boyd and A. Srinivasan
Cornell University
Ithaca, NY 14853.

E. P. Muntz
University of Southern California
Los Angeles, CA 90089.

R. K. Hanson
Stanford University
Stanford, CA 94305.

M. S. Holden
CUBRC
Buffalo, NY 14225.

6th AIAA/ASME Joint Thermophysics and Heat Transfer Conference
June 20-23, 1994 / Colorado Springs, CO

THERMOCHEMICAL NONEQUILIBRIUM DESIGN CALCULATIONS FOR DETAILED HYPERVELOCITY EXPERIMENTS IN THE LENS FACILITY

Iain D. Boyd* and Anand Srinivasan†
Cornell University, Ithaca, NY 14853

E. Philip Muntz§
University of Southern California, Los Angeles, CA 90089

Ronald K. Hanson**
Stanford University, Stanford, CA 94305

Michael S. Holden‡
CUBRC, Buffalo, NY 14225

Abstract

The Large Energy National Shock Tube is a relatively new hypersonic facility that produces sufficiently high enthalpy to dissociate both oxygen and nitrogen. Optical diagnostic techniques are under development that will probe these hypersonic flows at a detail not previously obtained. A critical element of these studies is the selection of flow conditions and body shape that will maximize interesting and measurable flow physics. In this paper, computations that include thermochemical nonequilibrium are presented for laminar hypersonic flow. Implications of the computed results for the use of the experimental diagnostics are discussed. It is demonstrated that a number of key physical phenomena in hypersonic flows may be generated and measured in this facility. It is concluded that the proposed experiments may contribute substantially to our understanding and modeling of such flows.

Introduction

Future generations of high-speed flight vehicles will be designed using increasingly sophisticated computational fluid dynamics (CFD) predictions. Depending on the flight conditions, these will be most likely accomplished at low altitudes using traditional continuum techniques to solve the Navier-Stokes equations, or particle Monte Carlo methods at high altitudes to provide a direct simulation of the gas dynamics. A large and important fraction of the flight envelope of these vehicles involves hypervelocity flight that is accompanied by nonequilibrium flow field chemistry. In addition, observables from high-altitude exhaust plumes, high-speed atmospheric and transatmospheric vehicles, as well as high altitude missile wakes, are critically sensitive to nonequilibrium chemistry. Assessment of the accuracy of simulation techniques for calculating these types of high-energy flows faces serious intrinsic barriers due to a lack of suitably detailed experimental flow field studies. For example, there are no studies presently in the literature that report measurements of multiple species concentrations or temperatures of different energy modes in hypersonic flow over simple body shapes.

Production of energetic hypersonic air flows in ground-based facilities is difficult. Present facilities permit investigation under very constrained circumstances and for very short test durations because of the requirement for high energy fluxes. Flight experiments are a possibility but are difficult to instrument in satisfactory detail for evaluation of critical thermochemical modeling. As a result, high-speed flows involving either equilibrium or nonequilibrium chemistry have not been evaluated except by relatively unsatisfactory indirect means such as observing shock shapes[1,2], measuring interferometer fringe shifts[3,4], obtaining line-of-sight low-resolution spectra of naturally emitted radiation[5,6], or using surface heat transfer and pressure measurements.[7,8]

A multi-disciplinary research program has been initiated to address the critically important absence of

* Assistant Professor. Mech. & Aero. Eng.
† Research Assistant. Mech. & Aero. Eng.
§ Professor. Aerospace Engineering.
** Professor. Mechanical Engineering.
‡ Senior Research Scientist.

suitably detailed experimental measurements in hypersonic flows. The aim of this program is to apply state-of-the-art experimental and numerical techniques in a combined approach. The primary experimental investigations will be conducted in the Large Energy National Shock Tunnel (LENS) located at CUBRC. Optical flow diagnostics are being developed at the University of Southern California, and at Stanford University. After testing, the hardware will be installed in the LENS facility. Numerical simulations employing both continuum and Monte Carlo methods with finite rate chemistry are being conducted at Cornell University.

The purpose of this paper is to describe use of continuum numerical simulations to design a set of interesting experimental configurations for investigation in the LENS facility. Based on the operating parameters of the shock tunnel, and the types of experimental diagnostic techniques that are being developed, the aim is to identify free stream conditions and body geometries that give rise to physical phenomena that can be measured and that will aid in development of physical models for the simulation techniques. A brief description of the experimental facility is provided including the range of operating conditions that are available. The diagnostic techniques are discussed including details of the required signal level and resolution. The continuum numerical method employed in this study solves the Navier-Stokes equations with finite-rate chemistry. A brief description of the code is given. Results are presented of parametric studies that illustrate some of the physical phenomena that may be generated in the LENS facility.

Experimental Facility

The main issues for experimental investigation of hypervelocity flows are: the ability to produce the high enthalpy flow conditions of interest; test time available for measurement; and contamination level. The LENS facility became operational in 1992 and has demonstrated its capabilities of achieving stagnation enthalpies in excess of 10^8 ft^2/s^2. This is achieved by generating stagnation conditions such as T_o=6,000 K and p_o=1,500 atm. Expansion of this stagnant gas through large nozzles typically produces a free stream condition of M_∞=8.5 for which the test time achieved is about 3 msec. This is a relatively long test-time that provides a number of advantages to the LENS system. For example, it permits investigation of slowly developing flow field structure in which separation or mixing occurs. The long test time also allows experimental measurements to be gathered with greater confidence.

The flight corridor that may be investigated in LENS is shown in Fig. 1. The estimated LENS hypersonic shock tunnel performance is show in Fig. 2. In this paper, flight conditions are investigated at an altitude of 24 km. This approach is taken to maximize the signals available for development and installation of the new optical diagnostic techniques. Future studies will consider the entire range of altitude and may include application of the direct simulation Monte Carlo (DSMC) method at the high end of the altitude scale.

Experimental Diagnostic Techniques

Experimental measurements to be taken of these flow fields will employ traditional intrusive and modern non-intrusive techniques. Pitot and electro-static probes will be used to measure pressure, and electron density and temperature, in the free stream and shock layer. On the surface of the body, heat transfer and shear stress will be measured. Non-intrusive techniques under development for application in the LENS experiments include Planar Laser-Induced Fluorescence (PLIF), Electron Beam Fluorescence (EBF) and Pulsed Electron Beam Fluorescence (PEBF). The methods are intended to yield detailed information on the hypervelocity flows including rotational and vibrational temperatures and number densities for individual species. These studies should provide a large amount of data in a degree of detail not seen before for thermochemical nonequilibrium air flows.

Electron Beam Studies

Electron beam fluorescence (EBF) is a well established diagnostic technique for the study of hypersonic flows up to number densities around 10^{23} m^{-3} and providing the flows are not strongly self-radiating.[9] The chief limitation of EBF has been that the electrons scatter at high gas densities and that the fluorescence emission is difficult to interpret due to quenching in unknown quenching environments. Previously, Muntz, Kunc and Erwin[10] and Wojcik et al.[11] have investigated ways around both of these difficulties (Electron-Photon Fluorescence) by using a combination of an e-beam and laser photons. Cattolica[12] has reported on some experiments relative to the EPF concept and Wojcik et al.[11] on pulsed electron beam fluorescence (PEBF). We have come to the opinion that a high current, pulsed electron beam offers the most interesting approach. High current beams are self focusing so

that they can partly negate scattering at higher densities. They retain the chief advantage of EBF which is the simultaneous broad-band excitation of all the rotational and vibrational internal energy states of all flow species and they can be coupled with gated detection to avoid quenching related interpretation difficulties.

High current pulsed e-beams can be generated by pseudosparks. Pseudospark devices[13,14] operate on the left hand side of the Paschen minimum. The discharge prefers long path lengths and an axial discharge generating energetic electrons is produced. The discharge electrons are given enough ballistic energy to separate from the field lines at the device's exit and are observed to form a well collimated beam of electrons. The pulsed pseudospark discharge produces an electron beam with a relatively broad energy range, having a mean between 0.5 and 0.7 times the breakdown potential (Benker[13]).

Since the pressure (10–100 Pa depending on gas, geometry and desired breakdown potential) in the pseudospark chamber is important, care must be exercised for installation in gas dynamic facilities. Figure 3 shows a schematic of the pulsed electron gun (PEG) inside of a blunt cone model. The gatling diaphragm apparatus consists of a 0.0005 in thick mylar sheet which is sandwiched between two 3 in diameter steel plates (one of which is geared). These plates have 12, 0.2 in diameter holes around a 1.35 in radius circle (see Fig. 4). A PEG operating at 35 kV voltage and 1 kA current for approximately 10 ns has about 50 times the energy needed to vaporize a few mm diameter area of the mylar sheet. Gas in the facility does not have time to enter the PEG chamber before the e-gun firing sequence is complete (about 10 ns). After a discharge, a stepper motor can rotate the mylar sandwich to align the next orifice. The mylar membrane has three main functions. First, it effectively isolates the PEG from the test section gases until the gun is fired (tested to 1 atm pressure differential). Second, it allows for minimal time losses between calibration in the shock tunnel dump tank prior to a run and the actual run. Third, it reduces model between-run refurbishment time since each mylar cartridge is good for 12 discharges.

Preliminary calibration studies have been performed in which either helium and nitrogen are employed as test gas. The PEG is fired into a known pressure of between 5 and 180 mTorr and the fluorescence measured. The expected linear trend is obtained between pressure (density) and integrated signal strength for each test gas. Further testing is necessary for full calibration of the diagnostic technique.

PLIF Studies

The flow computations presented in this paper will provide important input to the design of the PLIF component of the overall LENS research program. In a PLIF experiment, a suitable molecule in the test flow is excited by a laser sheet, with perpendicular collection of the resulting fluorescence.[15–20] The PLIF signal depends upon the mole fraction of the fluorescing species, and the temperature and pressure of the gas mixture. Therefore, flow field predictions can facilitate the design of an experiment with maximum dynamic range and signal-to-noise ratio (S/N) in the regions of interest. As explained by Palmer et al.[21] knowledge of these flow quantities is particularly relevant to the selection of the absorption line or combination of lines of the fluorescent species to use.

The planned PLIF investigation will use nitric oxide (NO) as the fluorescent species in an attempt to measure NO concentrations, rotational temperature, vibrational temperature, and velocity in the flow. The LENS experiments will benefit from the continuing efforts at developing and refining the diagnostic that have been proceeding at Stanford.[21–22] Most recently, work led by Houwing[22] used PLIF of NO to measure rotational temperature in supersonic flow over a cylinder. A schematic diagram of the experimental set-up for this study is shown in Fig. 5.

Numerical Investigation

Numerical studies of laminar hypervelocity flow in the LENS facility are being conducted using the continuum approach by solving the Navier-Stokes equations with coupled thermochemical nonequilibrium. The code employed has been developed by Palmer at NASA Ames Research Center.[23,24] It employs second-order flux splitting and has models implemented for finite rates of vibrational and chemical relaxation. The rotational and translational temperatures are assumed to be in equilibrium. The important phenomenon of coupled vibration-dissociation is modeled using the two-temperature approach of Park.[25] A seven species air model (N_2, O_2, NO, N, O, NO+, e^-) is employed. In the present study, thermochemistry is calculated using an implicit approach. The code is executed on a work-station and on a Cray C-90 supercomputer.

The numerical studies are conducted at different flow conditions and body geometries. The free stream flow conditions for LENS are computed using a nozzle code developed at CALSPAN.[26] The important in-

put parameters to this code are the stagnation temperature (T_o) and pressure (p_o), and the diameter of the nozzle throat (d^*). In addition to the mechanical constraints on the LENS system in terms of generating stagnation conditions, the amount of heating sustained by the nozzle throat also places a limit on the maximum operating enthalpy. In order to obtain high signal levels and nonequilibrium flow, an altitude of 24 km in the atmosphere is selected for the free-stream density condition. The LENS operating parameters that produce such flow are listed in Table 1. In Table 2 are the free stream conditions produced in the tunnel. In Table 2, M_X is the mass fraction of species X. Note that both the temperature and the amount of nitric oxide produced in the tunnel are higher in comparison to the air in the atmosphere at this density.

A spherically capped cone with a nose diameter of 0.254 m is selected as the generic body geometry for this investigation. Parametric study is conducted through variation of the cone angle. The overall length of the body is kept constant at about 1 m. The relatively large size of the body has several advantages. First, the large nose radius produces a well defined shock stand-off distance of a few centimeters. This provides sufficient spatial resolution for use of the optical diagnostic instrumentation. The length of the body is selected to allow sufficient time for recombination processes to develop. The relatively long test-time available at LENS allows the flow to develop fully while still providing time for measurement. In the calculations, an isothermal wall temperature of 500 K is assumed for the interaction of the flow with the surface of the cone.

The baseline configuration employs a cone angle of 10°. Further studies are performed in which this angle is varied between 0 and 20°. The aim is to assess the range of chemical physics occurring in these flows. At small angles, thermochemical relaxation may become frozen, whereas at large angles the flow moves towards chemical equilibrium. A schematic diagram of the baseline configuration is shown in Fig. 6. At a later date, a flare may be added at the base of the body to generate a region of recirculation.

Results and Discussion

The primary purpose in performing design calculations is to maximize the physical phenomena in the flow field that are measurable and that are of use in assessing and refining the computational models. Possible locations for positioning of the optical diagnostic instrumentation are indicated in Fig. 6. The calculations are to be used to guide final placement. In this section, results are presented for various geometric and free-stream conditions that are attainable in LENS. The emphasis is on generation of a range of phenomena that will challenge current physical models, and that are measurable.

10° Cone Angle

Flow field contours of the solution obtained for the baseline configuration are shown in Figs. 7a-7d. These results show the expected behavior for hypersonic flow over a spherically capped cone that has been investigated in many previous studies. The results of most interest here are for quantities that can be measured experimentally. These include rotational (assumed equal to translational) and vibrational temperatures, and species concentrations of N_2 and NO. To consider these properties in detail, profiles emanating normally from the surface at three different locations are presented. These profiles represent the paths that may be observed by the optical diagnostic techniques. For each of the geometric configurations considered, the locations of these profiles on the body surface are identified by the following X co-ordinates in Figs. 7: station 1, at X=0.0 m (stagnation streamline); station 2, at X=0.30 m; and station 3, at X=1.08 m.

Profiles of interest are first presented along the stagnation streamline in Figs. 8a-8c. These results indicate that the shock stand-off distance is about 18 mm. The temperature profiles indicate that the translational and vibrational modes equilibrate rapidly behind the shock-front. Behind the post-shock region there is a large boundary layer region in which the temperatures steadily fall to the surface value. The species mole fractions illustrate that at these flow conditions, molecular oxygen is nearly fully dissociated behind the shock. The degree of dissociation of molecular nitrogen is smaller but still noticeable. Strong recombination effects operate in the boundary layer. It is interesting that only very small changes occur in the relative concentration of nitric oxide along the stagnation streamline. The species concentrations shown in Fig. 8c should all be at sufficiently high levels to be readily measurable with the optical diagnostics in the LENS facility. This is the most basic requirement of any proposed LENS experiment. Generally, the densities and temperatures are greatest in this region, so that any difficulty in detection of the flow here would

imply that measurement elsewhere is hopeless.

Similar results are now shown in Figs. 9a-9c for station 2 which lies just beyond the shoulder of the cone. Care must be taken in the interpretation of the profiles along diagnostic stations 2 and 3. These data are not along streamlines. In spite of this, the initial rise in density and temperature will still be referred to as the shock front, and the region immediately behind will be termed the post-shock. In comparing the temperatures of Fig. 9a with those for the stagnation streamline, it is clear that the shock is much weaker at this point. Also, note the effect of the fluid expansion over the shoulder of the body. The translational temperature first rises above the vibrational temperature in the shock front. However, expansion subsequently relaxes the translational temperature more rapidly than vibration leaving the latter mode partially frozen. As the body surface is approached, the translational and vibrational energy modes equilibrate. The mole fractions indicate that less dissociation of molecular oxygen occurs due to the weaker shock strength in this region. In terms of molecular nitrogen concentration, the post shock value falls by more than a factor of two while the surface value falls by a factor of 12 in comparison with Fig. 8c.

The profiles obtained at the third diagnostic station are presented in Figs. 10a-10c. At this location, the thickness of the shock layer is about 20 mm. The temperature profiles indicate that the shock is much weaker than along the stagnation streamline. The translational temperature is first increased a small amount by the shock front. Subsequently, it rises further due to significant recombination close to the body surface. Note the relatively long vibrational relaxation zone that occurs over about 10 mm. The opportunity to measure these types of processes in detail should provide an excellent opportunity for in-depth assessment of the thermochemical models. It is clear from the mole fraction profiles that little changes in chemical composition occur in this region. In comparison with the values along the stagnation streamline, the concentration at the surface of molecular nitrogen is 5 times lower, while that for NO is 15 times lower.

20° Cone Angle

Assessment is now made of the effect of increasing the cone angle to 20° with all other flow conditions unchanged. In Figs. 11a-11f profiles of temperature, mole fraction, and number density are shown along diagnostic stations 2 and 3. The data along the stagnation streamline are essentially unchanged from Figs. 8 and so are not shown. Comparison of Figs. 11 with the results in Figs. 9-10 reveals some general trends. At station 2, Fig. 11a reveals that there is a significantly smaller degree of thermal nonequilibrium in comparison with Fig. 9a. The peak values for the translational and vibrational modes shown in Fig. 11a are equal indicating that the flow is closer to equilibrium at the larger cone angle. The number density profiles in Fig. 11c are similar to those in Fig. 9c except for being higher by a factor of about 2 at the body. At station 3, the profiles of all species concentrations show a different variation from Fig. 10. In comparison with the 10° case, the shock location is closer to the surface, and the post-shock region is shorter with the cone angle of 20°. The post-shock number densities of N_2 and NO are about 50% higher than the 10° case. At the body, these concentrations are about twice as high as the first calculation. The profile of atomic oxygen concentration is interesting: at 20° the post shock value is higher than case 1 yet the surface value is lower. It is proposed that these phenomena are due firstly to a stronger shock in the 20° case because of the blunter geometry; and secondly to a subsequent increase in recombination due to the higher pressures behind the shock. This interpretation is supported by the fact that both the translational and vibrational temperatures are higher at station 2 for the 20° case. Hence, increasing the cone angle to 20° places an increased emphasis on the recombination models. Significantly, the types of changes predicted for the different geometries by the present computations should be measurable with the non-intrusive diagnostics.

0° Cone Angle

To investigate the effect of rapid expansion, results are generated for a cone angle of 0°. These computations are presented in Figs. 12a-12f for temperatures, mole fractions, and number densities at the second and third diagnostic stations along the cone. Once again the results along the stagnation streamline are almost unchanged from the 10° case. At station 2, the degree of thermal nonequilibrium is assessed through comparison of Figs. 12a and 9a. For the 0° cone angle, the peak translational temperature is lower and the peak vibrational temperature slightly higher. The two modes only equilibrate right at the surface in Fig. 12a. It is clear that the degree of thermal nonequilibrium is much increased with the reduced cone angle. The number density profiles are quite similar for Figs. 12c

and 9c. As shown in Fig. 12d, the temperatures continue to exhibit a strong degree of nonequilibrium at station 3. The peak translational temperature at cone angle of 0° is significantly lower than the peak in Fig. 10a. However, the peak vibrational temperature in Fig. 12d is slightly higher than that obtained at 10°. This is a clear demonstration that the vibrational relaxation process is frozen under these conditions. The shapes of the number density profiles are quite similar to those shown in Fig. 10c. Generally, in Fig. 12f, the shock location is much further away from the surface, the post shock region is longer, and the concentrations are lower by a factor of 2 at the surface. In summary, decreasing the cone angle to 0° places a different emphasis on the thermochemical relaxation models for correct prediction of freezing effects. Again it is anticipated that the magnitude of changes computed here should be measurable.

To summarize the effects of changes in cone angle on flow field properties, the peak temperatures obtained in the computations presented above are plotted against their distance from the surface in Figs. 13a and 13b for diagnostic stations 2 and 3 respectively. It should be recalled from the previous discussions that the shock for the 20° cone angle is closest to the body surface. Hence, in these Figures, moving from left to right, the data for cone angles of 20°, then 10°, and finally 0° are shown. At station 2, Fig. 13a shows that the peak translational temperature decreases as the cone angle decreases from 20° to 0°. At the same time, the distance from the surface where the peak occurs is increased. By comparison, the peak vibrational temperature increases by a small amount over the same variation while the distance from the surface again increases. This increase in peak vibrational temperature illustrates the strong effect of freezing as the cone angle is decreased. At station 3, Fig. 13b indicates that the translational temperature again decreases with cone angle. However, the peak vibrational temperature for cone angle of 20° is actually higher than at 10°. This indicates that there is a strong effect due to recombination for the flow over the more blunted body.

10° Cone Angle with Fake Air

In addition to changes in geometry, the flows investigated in LENS may be varied through generation of different free-stream conditions. The most obvious way to accomplish this is through variation of total temperature and pressure, and the nozzle throat diameter. However, the composition of the gas also may be varied. Hence it is possible to manufacture a range of air-like gas compositions. The benefit in considering such studies is that it provides a robust challenge to the thermochemical models employed in the numerical computations. For example, by running with pure nitrogen, the subset of models relevant to N_2 and N may be tested. By systematically increasing the relative mole fraction of molecular oxygen in the free-stream, the models for all other species can be included. Due to safety reasons, it is unlikely that any tests will be made with pure oxygen. As an example of such studies, a computation is performed for a cone angle of 10°, using the same free-stream conditions for density, temperature, and velocity as shown in Table 2, but with mass fractions of M_{N_2}=M_{O_2}=0.5, and all other fractions set to zero. The results of this study are shown in Figs. 14a-14f for conditions along the stagnation streamline, and at the second diagnostic station. Along the stagnation streamline, the main difference from the previous 10° calculation is that a larger fraction of molecular oxygen is dissociated. This has the effect of reducing the post-shock temperatures, and the shock location is moved closer to the body. At station 2, the main differences are due to a decreased concentration of NO and atomic oxygen.

Experimental Considerations

Consideration is now given to the implications on the experimental investigations of the computed results presented in this section.

PEBF Experiments

Typical species concentrations and temperatures behind the shock wave are presented in Table 3. These are of course approximate; also, they do not represent properties in either the boundary or entropy layers.

Following Muntz and Erwin[27] and Muntz[9] the total population of an excited state k due to instantaneous excitation by a pulsed e-beam of current I_B and duration τ_B is

$$[N_k(v', J')]_{t=0} = 6.25 \times 10^{18} I_B \Omega_{d,k} n(v_1'', J_1'') \tau_B L \quad (1)$$

where L is the length of emission observed along the beam's direction of propagation, $n_i(v_1'', J_1'')$ is the number density of a rotation-vibrational level of the ith species in the flow field and $\Omega_{l_2,k}$ is the excitation collision cross-section for beam electrons to bring the v_1'', J_1'' molecules in the initial electronic state l_1 to v', J' of an upper electronic state k, it is assumed that the transition can be approximated by $\Delta J = 0$. There

is subsequent spontaneous emission to a lower electronic state l_2 designated by v_2'', J_2''.

The emission to l_2 is observed for a time τ. For the $[N_k]_{t=0}$ molecules generated by the e-beam, the number of photons emitted during τ for the transition $v' \rightarrow v_2''$ is

$$N_{PH} = [N_k(v', J')]_{t=0}(A_{k,l_2}(v', v_2'')/A_{k,l_2})(1-e^{-A_{k,l_2}\tau}) \quad (2)$$

For this experiment it has been assumed that all emitted lines from the J' rotational level (typically $J_2'' = J^1 \pm 1, 0$) are not resolved. A_{k,l_2} is the spontaneous emission probability for k to l_2. $A_{k,l_2}(v', v_2'')$ is the product of the Franck-Condon factor for the v', v_2'' transition with A_{k,l_2}.

Using Eqs. (1) and (2) typical numbers of emitted photons that provide information about a particular v_1'', J_1'' level can be estimated. The number densities listed in Table 3 need to be converted to approximate v_1'', J_1'' population. An examination of the N_2, O_2 and NO vibration and rotational partition functions indicates that fractional populations of 0.005 and above for rotational levels will cover a significant proportion of the rotational population of each of these molecules even at the maximum temperature of 5000 K. Similarly a vibrational fractional population of 0.05 is appropriate. It is unlikely that observations will be made of single rotational lines, a more likely number is 10, thus the rotational partition function becomes effectively 0.05. More discussion on these points is presented in the recent paper by Muntz, Boyd and Ketsdever.[28] The number density $n_i(v_1'', J_1'')$ is related to the total number density of species i through the normalized fractional populations P_R and P_V, or $n_i(v_1'', J_1'') = n_i P_R(J_1'')P_V(v_1'')$. Consider nitrogen, substitute into Eq. (1) for: the minimum N_2 number density from Table 3 of 8×10^{23} m^{-3}, the excitation cross-section $\Omega_{l_1,k} = 10^{-18}$ cm^2, $L = 1$ mm, $\tau_B = 10^{-8}$ s, $I_B = 10^3$ amps, $P_R = 0.05$ and $P_v = 0.05$. The resulting total number of excited state emitters becomes 1×10^{10}. With a τ of 10^{-8} s, Eq. (2) gives for a typical $A_{k,l_2}(v', v_2'')/A_{k,l_2} = 0.3$, $N_{PH} = 3 \times 10^7$. Assuming a reasonable optical system with an acceptance solid angle of 0.06 sr and detective quantum efficiency of 0.3, the number of statistically useful photons is 5×10^4. Accurate measurement of rotational temperature and vibrational population distributions will be possible.

For O_2 based on the results presented by Muntz[9] and Table 3 there will be about a factor of 50 decrease in emission. In this case, the rotational structure will be more difficult, but certainly observations of vibrational populations are realizable. The prospects for useful detection of NO do not appear particularly encouraging based on the results presented earlier by Muntz.[9] However this needs to be re-examined, since it depends on the issue of self-absorption for the resonance fluorescence that is excited by the e-beam.

PLIF Experiments

In contrast to flows investigated to date using PLIF in the Stanford shock tunnel, the flows in LENS will contain comparable levels of naturally-occurring NO, according to the calculations presented in this paper. Therefore, it is anticipated that seeding will be unnecessary. At the stagnation point, the results presented in Fig. 8c indicate that NO number densities are on the order of 10^{24} m^{-3} or more. By way of comparison, NO stagnation point concentrations on the order of 10^{22} m^{-3} proved adequate for the recent work at Stanford. Indeed, the magnitudes of the computed NO number densities for the LENS test case may well recommend the use of weaker, satellite absorption transitions to avoid difficulties with beam attenuation due to absorption. However, as mentioned previously, it is important to note that the fluorescent signal depends on many factors other than fluorescent species number density. For instance, collisional quenching of the NO fluorescence signal attributable to oxygen may be a significant factor in the LENS tunnel. By comparison, for the preliminary work at Stanford, in which an argon bath was used, this was not an important issue. In any case, the role for computations of NO number density (as well as number densities of other species) in evaluating candidate PLIF schemes is clear. The calculations suggest that the spatial resolution of the PLIF system will not be a limiting factor. It should be able to resolve the flow to better than 1 mm, which is considered acceptable given the computed shock standoff distance of 18 mm. The spatial resolution depends on the optical set-up of the camera system, and can be varied somewhat as desired, subject to physical constraints of camera placement in the LENS tunnel. For the most recent Stanford work, the spatial resolution was approximately 0.25 mm.

Summary

Computational results have been generated by solving the Navier-Stokes equations with coupled finite-rate thermochemical relaxation for the LENS hypersonic facility. Studies were made to investigate the

effect of variation in geometry and free-stream composition. The conditions investigated were designed to maximize the amount of thermochemical relaxation behavior in the flow. The standard condition employed a spherically capped cone with a cone angle of 10° and the flow conditions corresponded to an altitude of 24 km at a velocity of 4.12 km/s. Under these conditions, post-shock temperatures of about 5,000 K were obtained. In various regions of the flow field, both thermal equilibrium and nonequilibrium are observed for the translational and vibrational temperatures. Nonequilibrium was generated through rapid compression in the shock front and expansion over the spherical cap. In addition, significant dissociation of both oxygen and nitrogen was predicted. Chemical nonequilibrium was also affected by the variation in fluid physics occurring in the flow.

Variation of the cone angle led to an increased emphasis on different aspects of the thermochemical models. At a larger angle, recombination effects were significant, whereas at a smaller angle the relaxation processes were partially frozen. It is concluded that the LENS facility is capable of generating flow conditions that will challenge the current thermochemical models employed in numerical simulation. A further aspect of the present study was the assessment of whether the changes computed for the flow field as a result of variation in geometry and free-stream conditions could be measured using new non-intrusive diagnostic techniques that are under development for installation in LENS. It was concluded that the present results were very encouraging from this point of view. There appears to be adequate signal levels and the flow structures are sufficiently large so that spatial resolution should not be an issue. Therefore, there is the very exciting possibility that this combination of numerical and experimental studies will be successful in making significant progress in our understanding of these flows leading to development of improved predictive capabilities.

Acknowledgments

This work is supported by the Air Force Office of Scientific Research under University Research Initiative F49620-93-1-0373 with Julian Tishkoff as grant monitor.

Table 1. LENS operating parameters.

T_o	6,000 (K)
p_o	1,500 (Atm)
d*	0.057 (m)

Table 2. Free stream flow conditions representing an altitude of 24.5 km.

ρ_∞	4.4×10^{-2} (kg/m^3)
T_∞	881 (K)
U_∞	4.12 (km/s)
M_{N_2}	0.7199894
M_{O_2}	0.2227383
M_{NO}	0.0565355
M_O	0.000738

Table 3. Representative post-shock properties.

Station	Species	No. Density	T_v	T_R
1	N_2	6×10^{24}	5000	5000
	O_2	2×10^{23}	5000	5000
	O	3×10^{24}	5000	5000
	NO	5×10^{23}	5000	5000
2	N_2	1×10^{24}	3400	2800
	O_2	2×10^{23}	3400	2800
	O	2×10^{23}	3400	2800
	NO	1×10^{23}	3400	2800
3	N_2	8×10^{23}	2600	2700
	O_2	2×10^{23}	2600	2700
	O	8×10^{22}	2600	2700
	NO	6×10^{22}	2600	2700

References

[1] Hornung, H.G., "Non-equilibrium Dissociating Nitrogen Flow Over Spheres and Circular Cylinders," *Journal of Fluid Mechanics*, Vol. 53, 1972, pp. 149-176.

[2] Candler, G.V., "On the Computation of Shock Shapes in Nonequilibrium Hypersonic Flows," AIAA Paper 89-0312, Jan. 1989.

[3] Kewley, D.J. and Hornung, H.G., "Free-Piston Shock-Tube Study of Nitrogen Dissociation," *Chemical Physics Letters*, Vol. 4, No. 3, 1974, pp. 531-536.

[4] Boyd, I.D. and Gokcen, T., "Evaluation of Thermochemical Models for Particle and Continuum Simulations of Hypersonic Flow," *Journal of Thermophysics and Heat Transfer*, Vol. 7, 1993, pp. 406-411.

[5] Allen, R.A., Camm, J.C., and Keck, J.C., "Radiation from Hot Nitrogen," AVCO Everett Research Lab., Everett, MA, Research Rept. 102, April 1961.

[6] Park, C., "Assessment of a Two Temperature Kinetic Model for Dissociating and Weakly Ionizing Nitrogen," *Journal of Thermophysics and Heat Transfer*, Vol. 2, No. 1, 1988, pp. 8-16.

[7] Cleary, J.W., "Effects of Angle of Attack and Bluntness on Laminar Heating-Rate Distributions of a 15° Cone at a Mach Number of 10.6," NASA TN D-5450, October 1969.

[8] Cleary, J.W., "An Experimental and Theoretical Investigation of the Pressure Distribution and Flow Fields of Blunted Cones at Hypersonic Mach Numbers," NASA TN D-2969, August 1965.

[9] Muntz, E. P., "The Electron Beam Fluorescence Technique," AGARDograph 132.

[10] Muntz, E. P., Kunc, J. A. and Erwin, D. A., "A Pulsed Electron-Photon Fluorescence Technique for Temperatures and Specie Concentration Measurement at Points in Relatively Dense, Unseeded Air Flow," AIAA Paper 87-1526, January 1987.

[11] Wojcik, R., Schilling, J. N. and Erwin, D. A., "Rarefied Flow Diagnostics Using Pulsed High-Current Electron Beams," AIAA Paper 90-1515, January 1990.

[12] Cattolica, R. J., "Modern Developments in Electron-Beam Fluorescence," in *Rarefied Gas Dynamics*, ed. A. Beylich, VCH, Weinheim, 1991, pp. 1552-1592.

[13] Benker, W., Christensen, J., Frank, K., Gundel, H., Hartmann, W., Redel, T. and Steller, M., "Generation of Intense Electron Beam by the Pseudospark Discharge," *Plasma Science*, Vol. 17, 1989, pp. 754-757.

[14] Frank, K. and Christensen, J., "The Fundamentals of the Pseudospark and its Applications," *Plasma Science*, Vol. 17, 1989, pp. 748-753.

[15] McMillin, B.K., Palmer, J.L., and Hanson, R.K., "Temporally Resolved, Two-Line Fluorescence Imaging of NO Temperature in a Traverse Jet in Supersonic Cross Flow," *Applied Optics*, Vol. 32, No. 20, 1993, pp. 7532,7545.

[16] Palmer, J.L., McMillin, B.K., and Hanson, R.K., "Planar Laser-Induced Fluorescence Imaging of Velocity and Temperature in Shock Tunnel Free Jet Flow," AIAA Paper 92-0762, Reno, NV, January 1992.

[17] Palmer, J.L. and Hanson, R.K., " Planar Laser-Induced Fluorescence Imaging in Free Jet Flows with Vibrational Nonequilibrium," AIAA Paper 93-0046, Reno, NV, January 1993.

[18] Seitzman, J.M., Kychakoff, G., and Hanson, R.K., "Instantaneous Temperature Field Measurements Using Planar Laser-Induced Fluorescence," *Optics Letters*, Vol. 10, 1985, pp. 439-441.

[19] van Cruyningen, I., Lozano, A., and Hanson, R.K., "Quantitative Imaging of Concentration by Planar Laser-Induced Fluorescence," *Experiments in Fluids*, Vol. 10, 1990, pp. 41-49.

[20] Hanson, R.K., Seitzman, J.M., and Paul, P.H., "Planar Laser-Fluorescence Imaging of Combustion Gases," *Applied Physics B*, 1989, Vol. 50, pp. 441-454.

[21] Palmer, J.L., Thurber, M.C., Wehe, S.D., and Hanson, R.K., and Houwing, A.F.P., "PLIF Imaging of Transient Shock Phenomena in Hypersonic Flows," AIAA Paper 94-2642, Colorado Springs, CO, June 1994.

[22] Houwing, A.F.P., Boyce, R.R., Palmer, J.L., Thurber, M.C., Wehe, S.D., and Hanson, R.K., "PLIF Thermometry in a High-Temperature Shock Layer Flow on a Cylinder in a Supersonic Jet," submitted for presentation at 33rd Aerospace Sciences Meeting, Reno, NV, January 1995.

[23] Palmer, G., "Enhanced Thermochemical Nonequilibrium Computations of Flow Around the Aeroassist Flight Experiment," AIAA Paper 90-1702.

[24] Palmer, G. "Explicit Thermochemical Nonequilibrium Algorithm Applied to Compute Three-Dimensional Aeroassist Flight Experiment Flowfields," *Journal of Spacecraft and Rockets*, Vol. 27, 1990, pp. 545-553.

[25] Park, C., *Nonequilibrium Hypersonic Aerothermodynamics*, John Wiley and Sons, Inc., New York, 1989.

[26] Lordi, J.A., Mates, R.E., and Moselle, J.R., NASA CR-472, 1966.

[27] Muntz, E. P. and Erwin, D. A., "Rapid Pulse Electron Beam Fluorescence for Flow Field Diagnostics," in *New Trends in Instrumentation for Hypersonic Research*, ed. A. Boulier, p. 265, NATO ASI Series, Series E: Applied Sciences, Vol. 21, Kluwer, Dodrecht, 1993.

[28] Muntz, E. P., Boyd, I.D., and Ketsdever, A., "Rarefied Flow Testing in the 1990s: Measuring those Phenomena that are Difficult to Calculate," AIAA Paper 94-2639, June 1994.

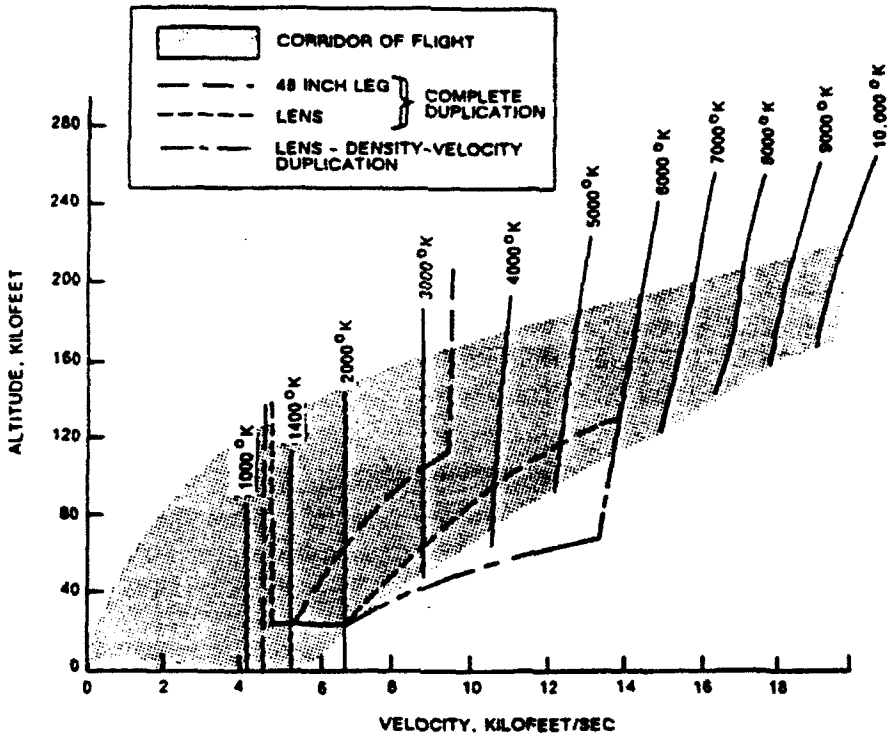

Fig. 1 Flight corridor available for testing in LENS.

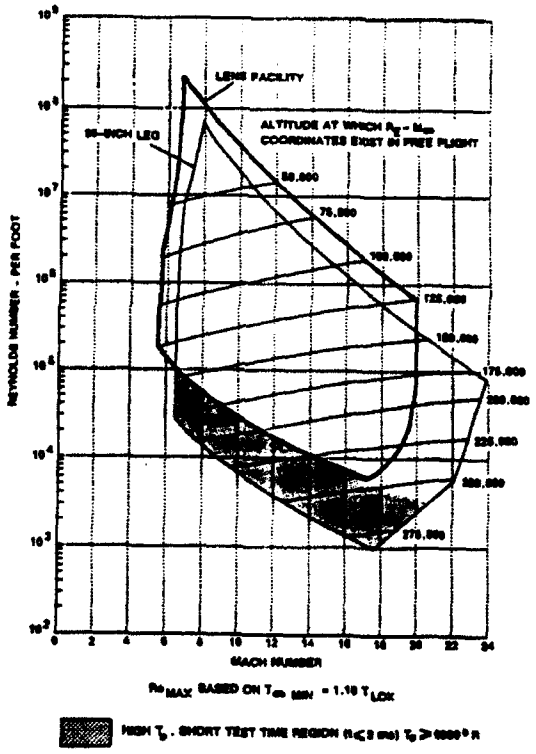

Fig. 2 Predicted performance of LENS facility.

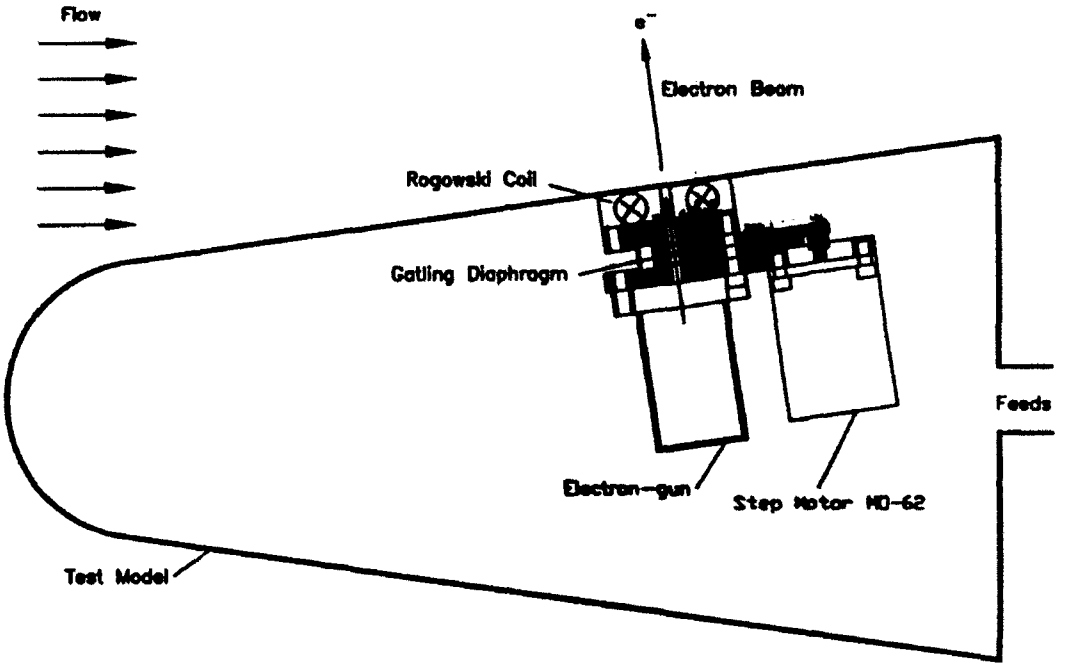

Fig. 3 Pulsed electron gun installation inside blunt cone model.

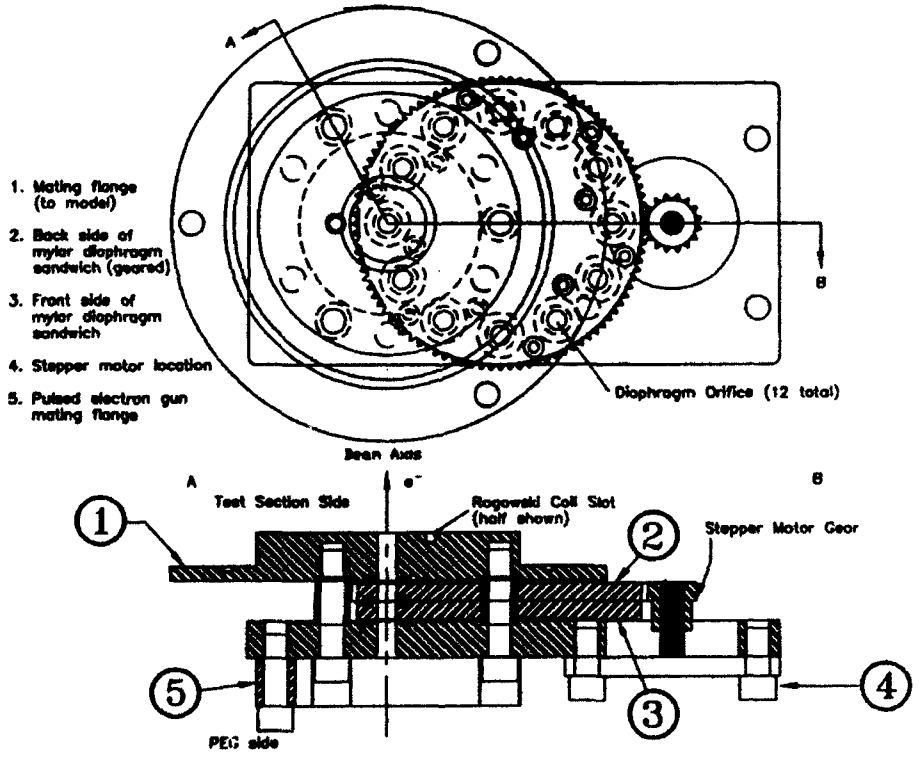

Fig. 4 Gatling diaphragm with evaporative windows for pulsed electron gun.

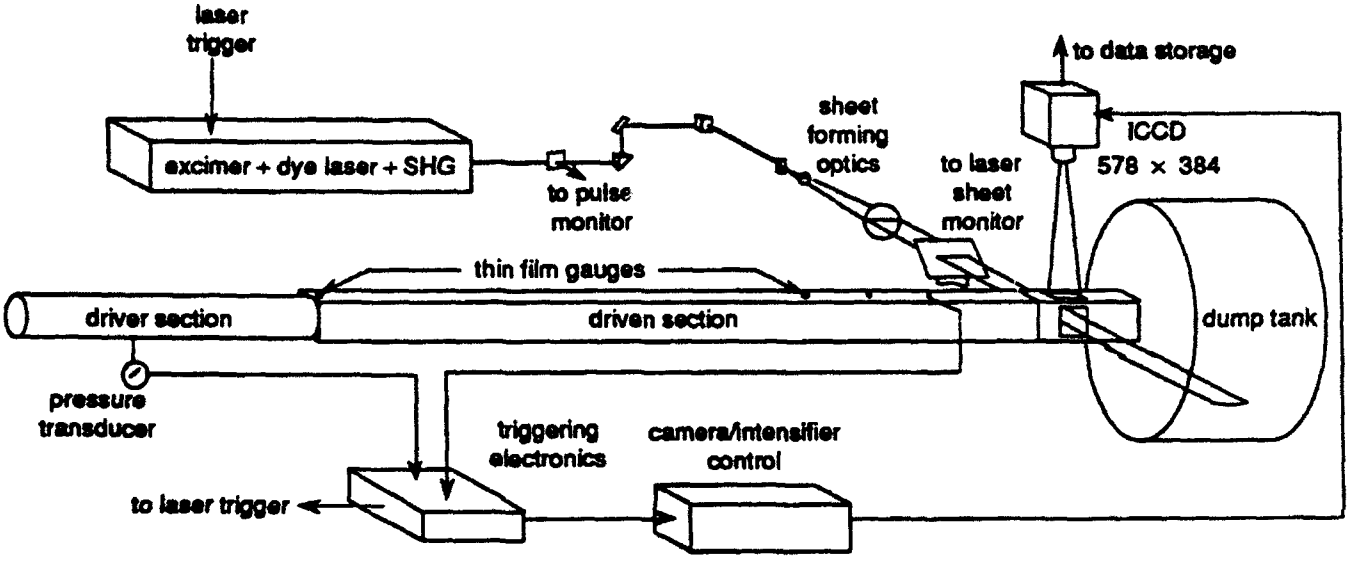

Fig. 5 Schematic of experimental facility at Stanford for PLIF imaging.

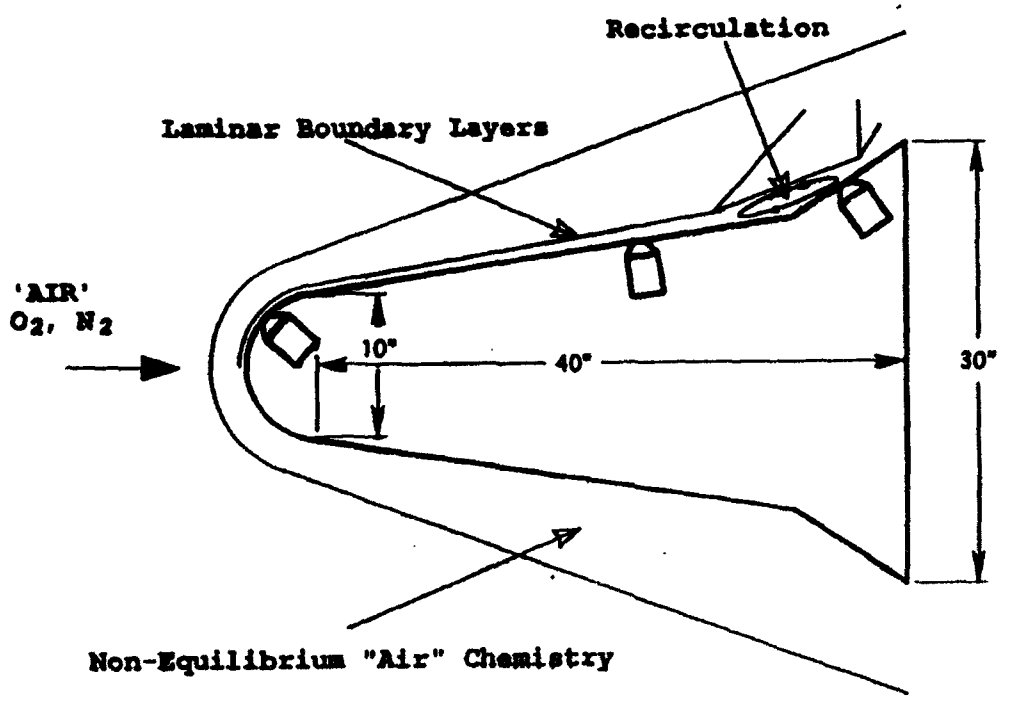

Fig. 6 Schematic diagram showing candidates for positioning of optical diagnostics instrumentation.

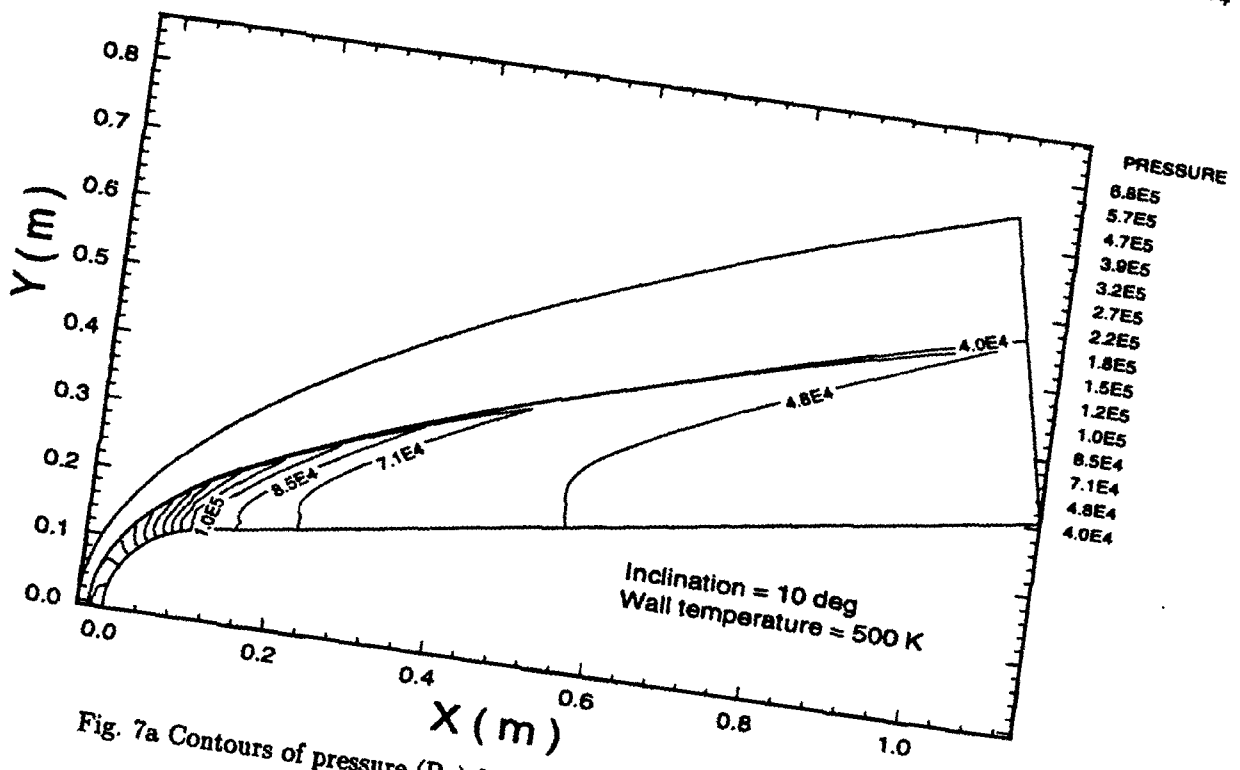

Fig. 7a Contours of pressure (Pa) for real air and geometry with 10° cone angle.

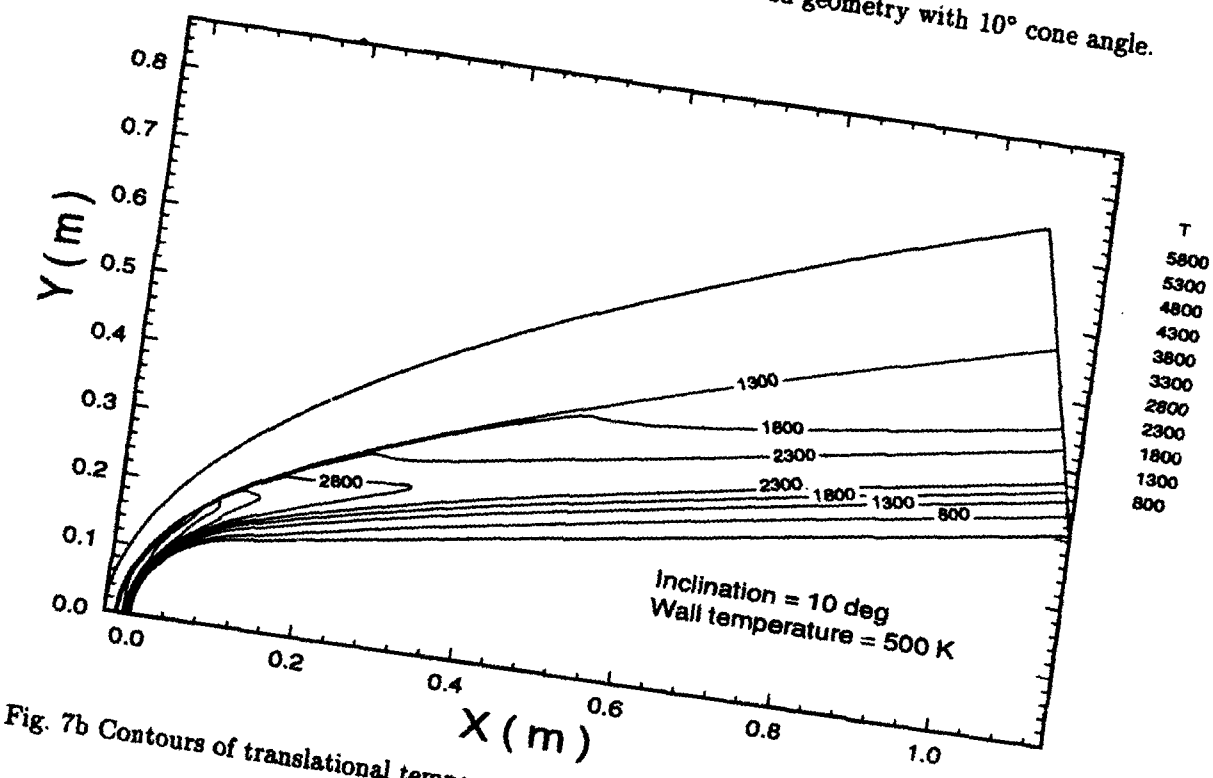

Fig. 7b Contours of translational temperature (K) for real air and geometry with 10° cone angle.

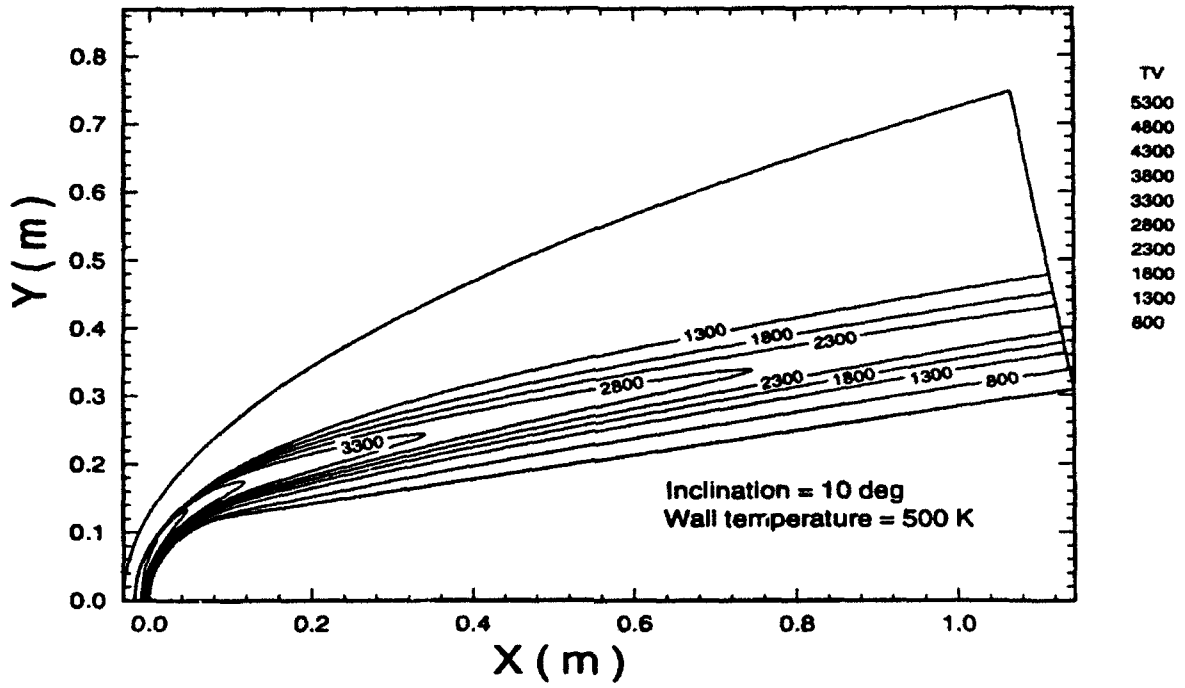

Fig. 7c Contours of vibrational temperature (K) for real air and geometry with 10° cone angle.

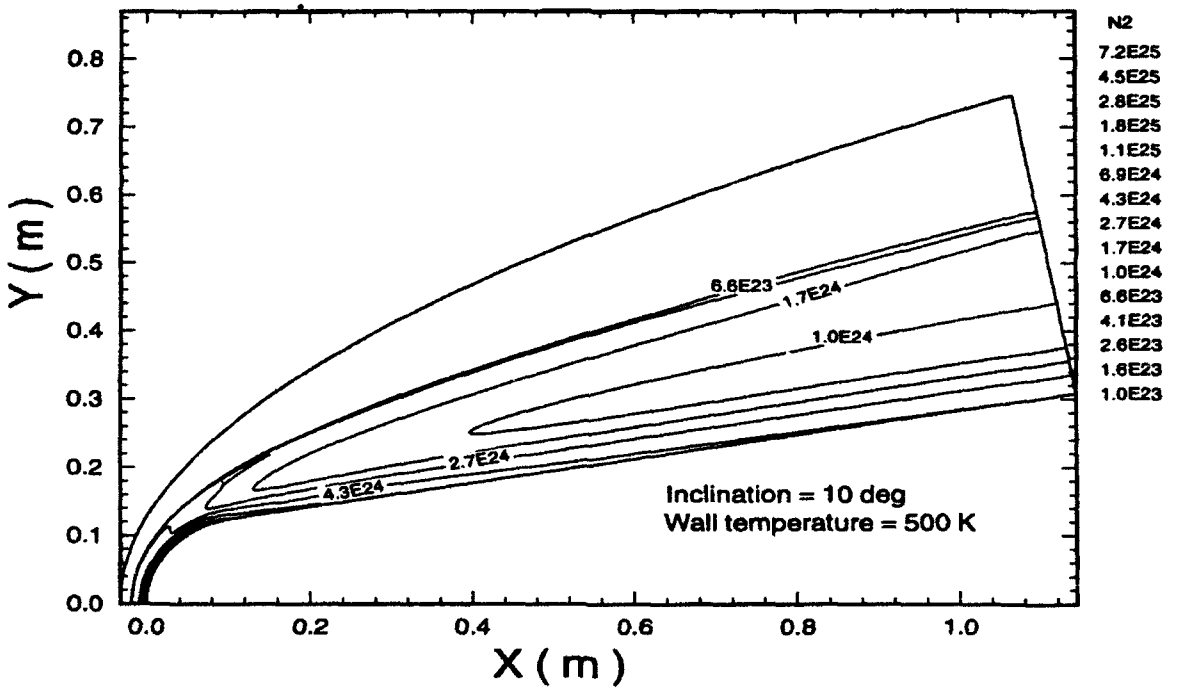

Fig. 7d Contours of N_2 number density (molecules per m^3) for real air and geometry with 10° cone angle.

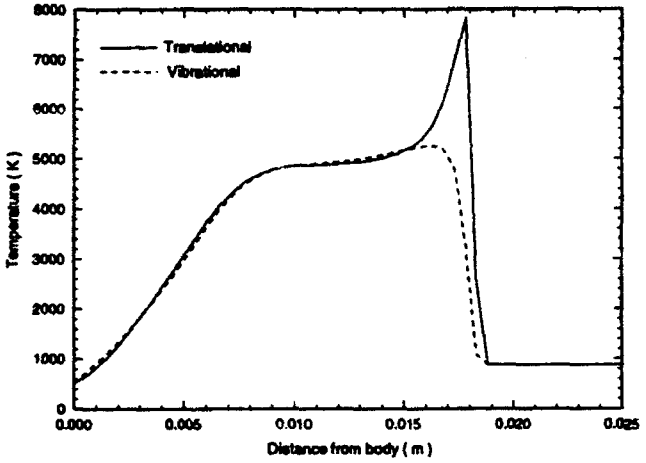

Fig. 8a Temperature profiles along stagnation line for real air and geometry with 10° cone angle.

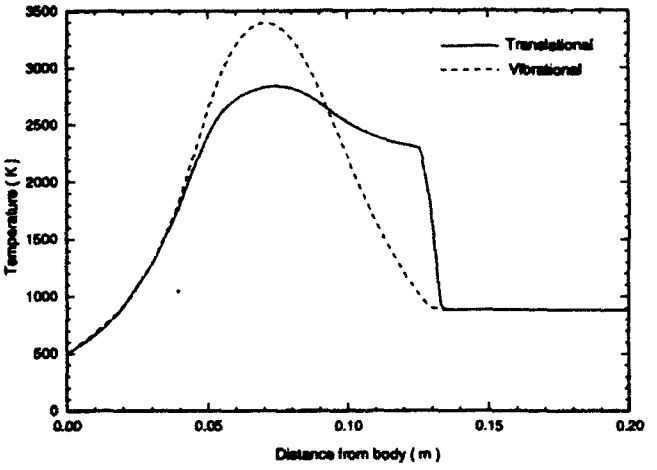

Fig. 9a Temperature profiles along diagnostic station 2 for real air and geometry with 10° cone angle.

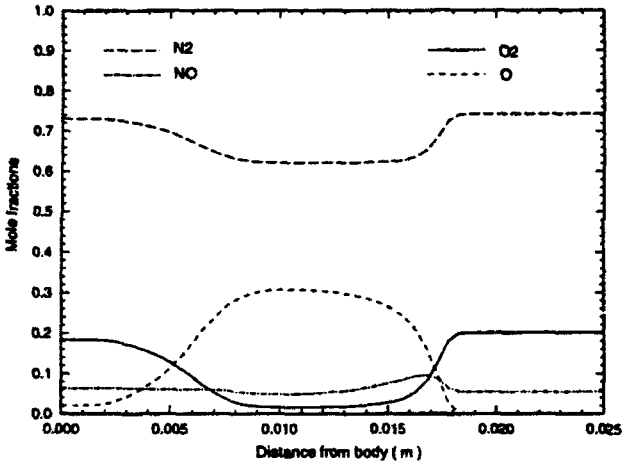

Fig. 8b Mole fraction profiles along stagnation line for real air and geometry with 10° cone angle.

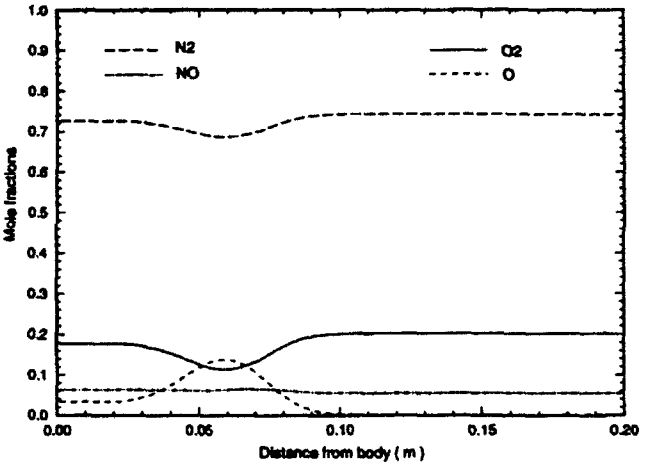

Fig. 9b Mole fraction profiles along diagnostic station 2 for real air and geometry with 10° cone angle.

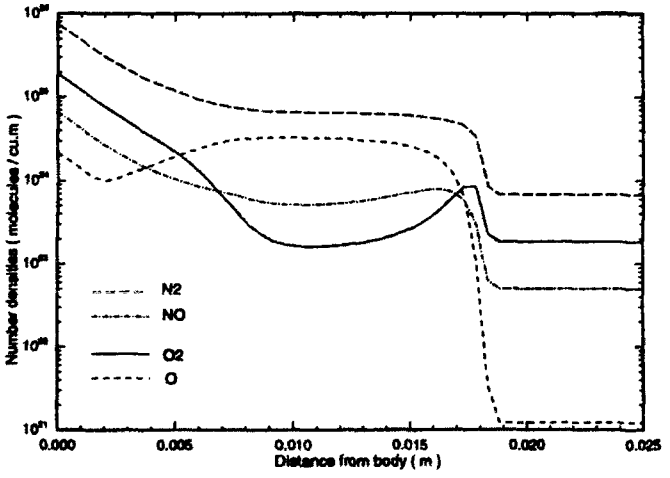

Fig. 8c Number density profiles along stagnation line for real air and geometry with 10° cone angle.

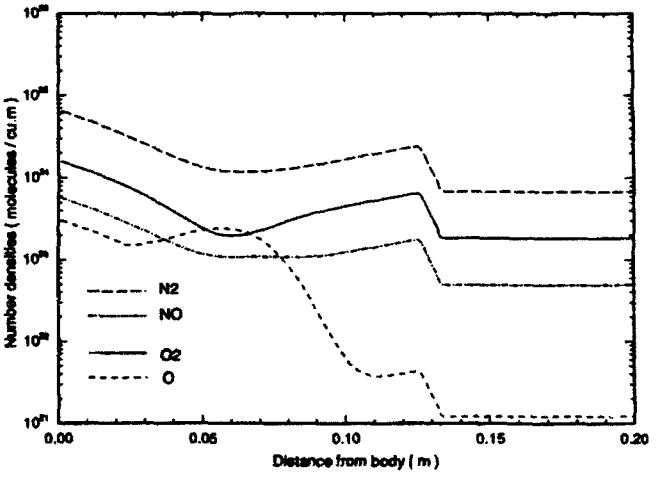

Fig. 9c Number density profiles along diagnostic station 2 for real air and geometry with 10° cone angle.

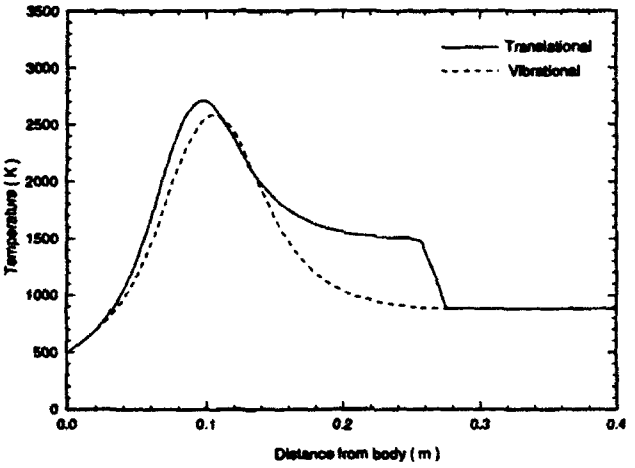

Fig. 10a Temperature profiles along diagnostic station 3 for real air and geometry with 10° cone angle.

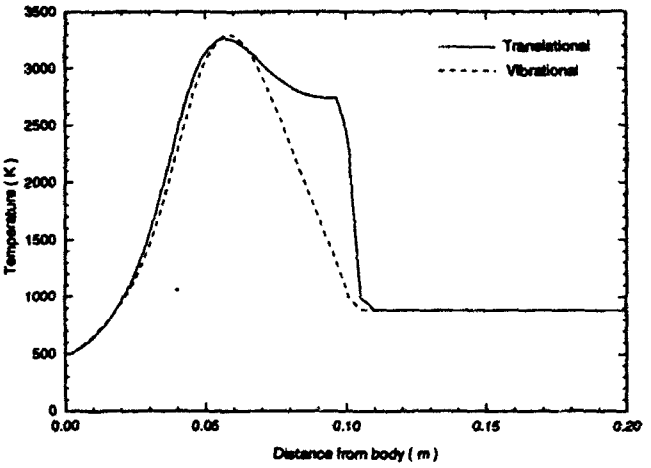

Fig. 11a Temperature profiles along diagnostic station 2 for real air and geometry with 20° cone angle.

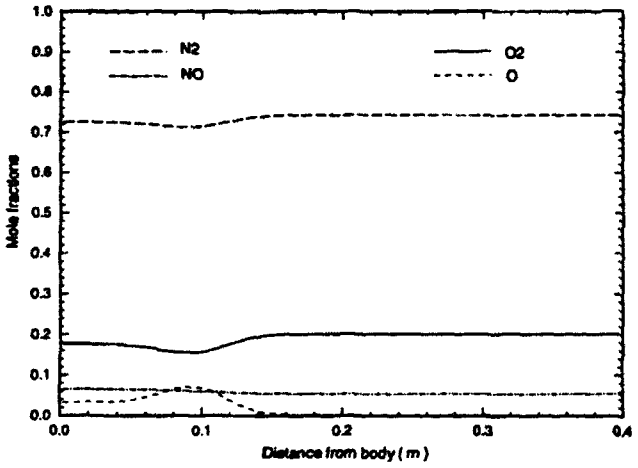

Fig. 10b Mole fraction profiles along diagnostic station 3 for real air and geometry with 10° cone angle.

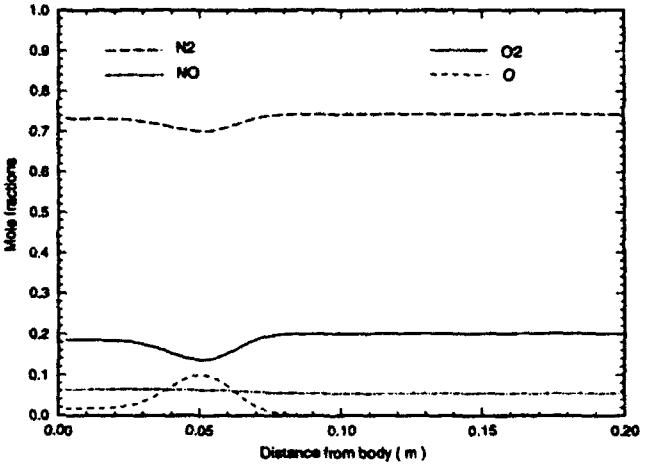

Fig. 11b Mole fraction profiles along diagnostic station 2 for real air and geometry with 20° cone angle.

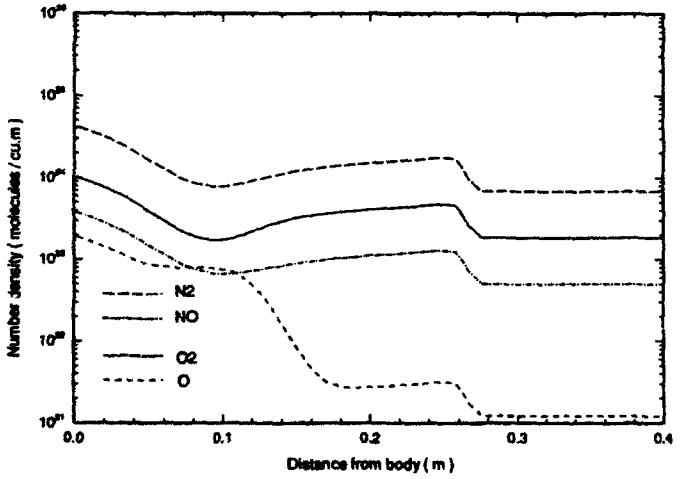

Fig. 10c Number density profiles along diagnostic station 3 for real air and geometry with 10° cone angle.

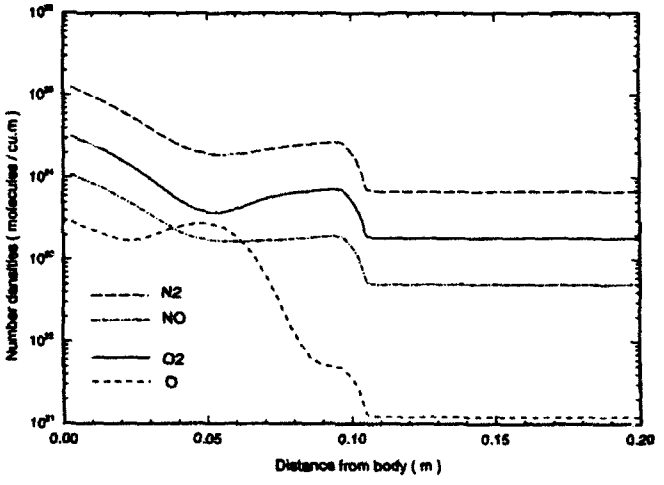

Fig. 11c Number density profiles along diagnostic station 2 for real air and geometry with 20° cone angle.

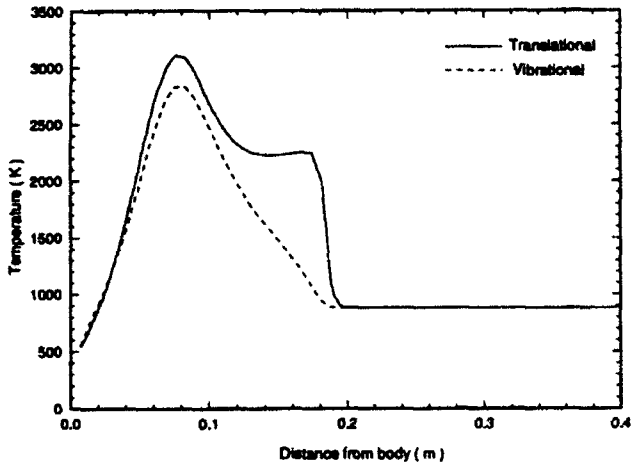

Fig. 11d Temperature profiles along diagnostic station 3 for real air and geometry with 20° cone angle.

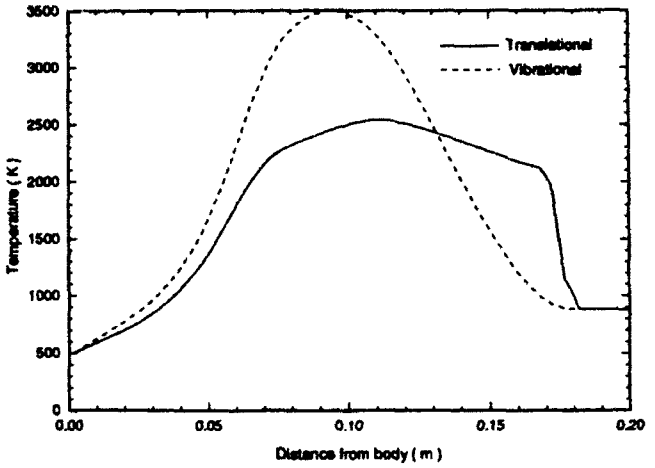

Fig. 12a Temperature profiles along diagnostic station 2 for real air and geometry with 0° cone angle.

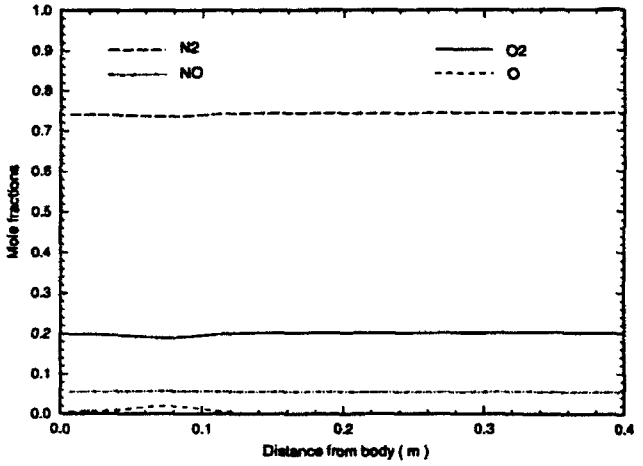

Fig. 11e Mole fraction profiles along diagnostic station 3 for real air and geometry with 20° cone angle.

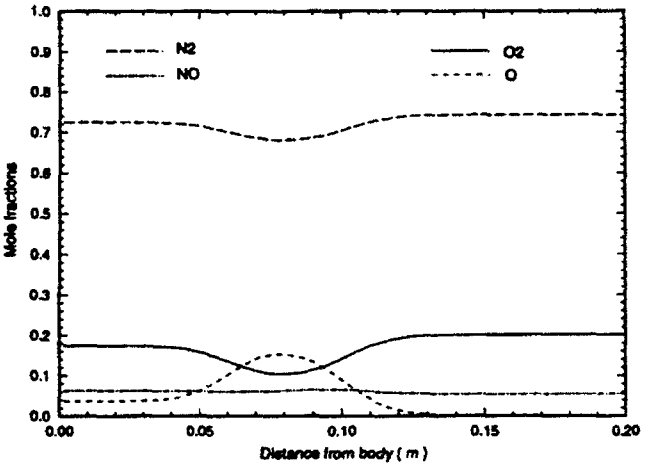

Fig. 12b Mole fraction profiles along diagnostic station 2 for real air and geometry with 0° cone angle.

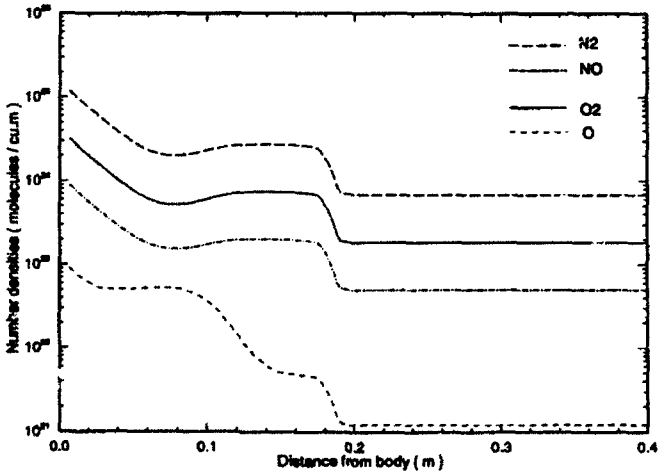

Fig. 11f Number density profiles along diagnostic station 3 for real air and geometry with 20° cone angle.

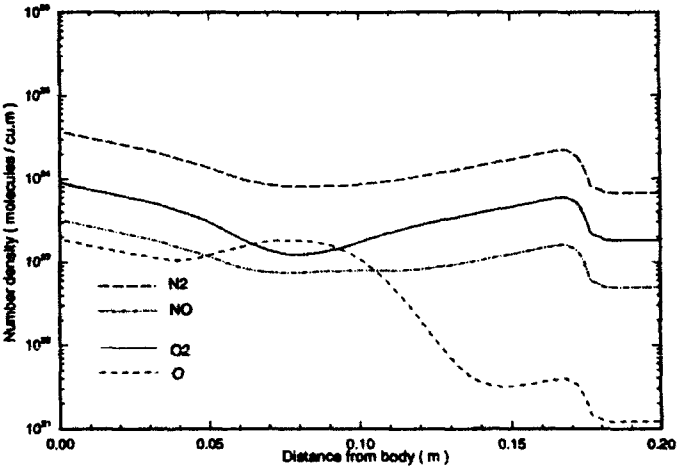

Fig. 12c Number density profiles along diagnostic station 2 for real air and geometry with 0° cone angle.

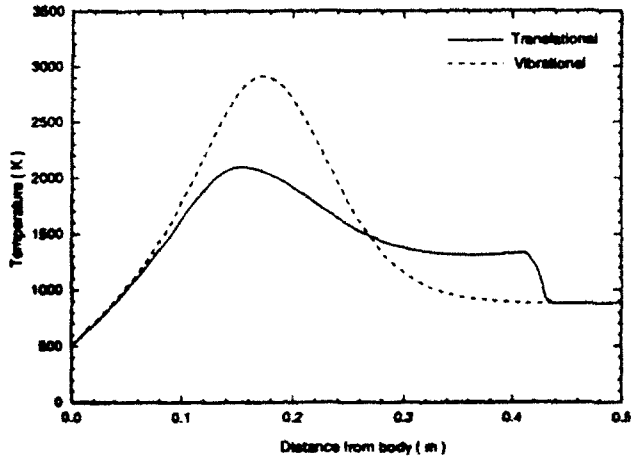

Fig. 12d Temperature profiles along diagnostic station 3 for real air and geometry with 0° cone angle.

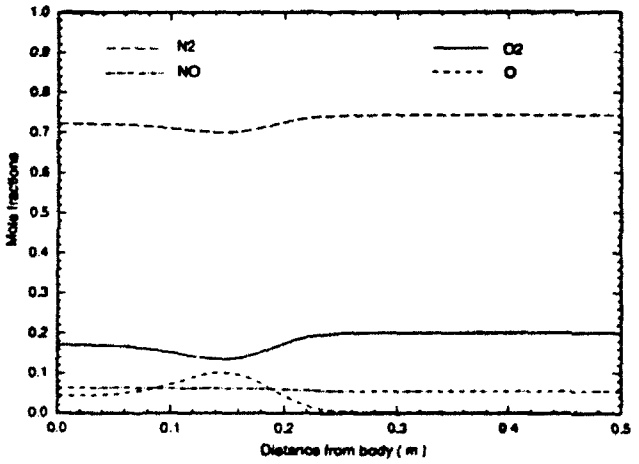

Fig. 12e Mole fraction profiles along diagnostic station 3 for real air and geometry with 0° cone angle.

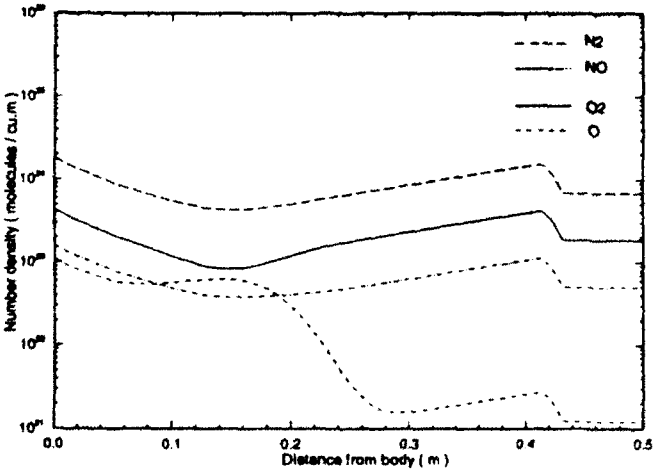

Fig. 12f Number density profiles along diagnostic station 3 for real air and geometry with 0° cone angle.

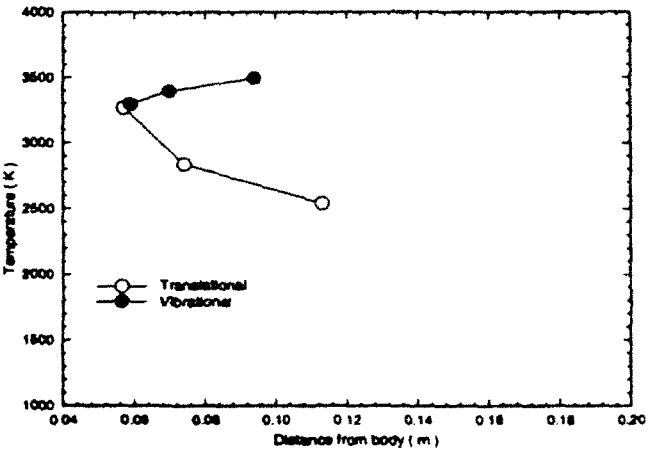

Fig. 13a Variation of peak temperature with distance from surface along diagnostic station 2 for all cone angles.

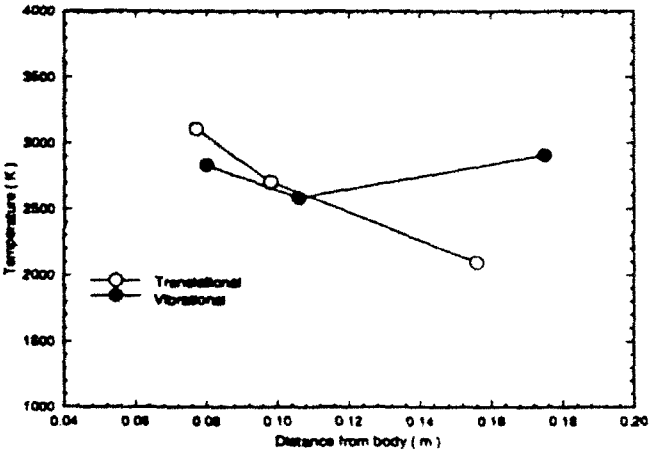

Fig. 13b Variation of peak temperature with distance from surface along diagnostic station 3 for all cone angles.

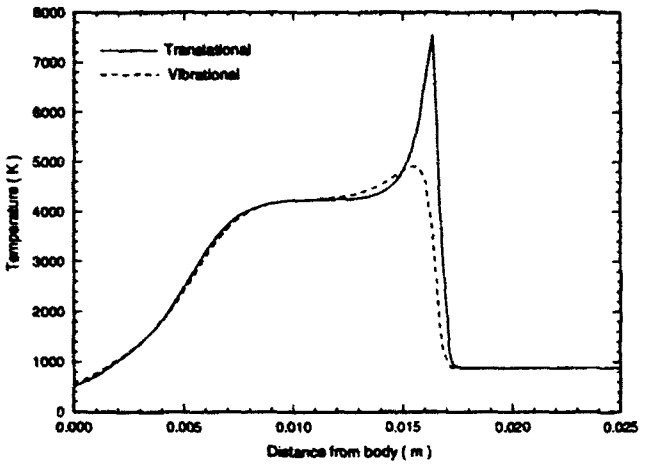

Fig. 14a Temperature profiles along stagnation line for fake air and geometry with 10° cone angle.

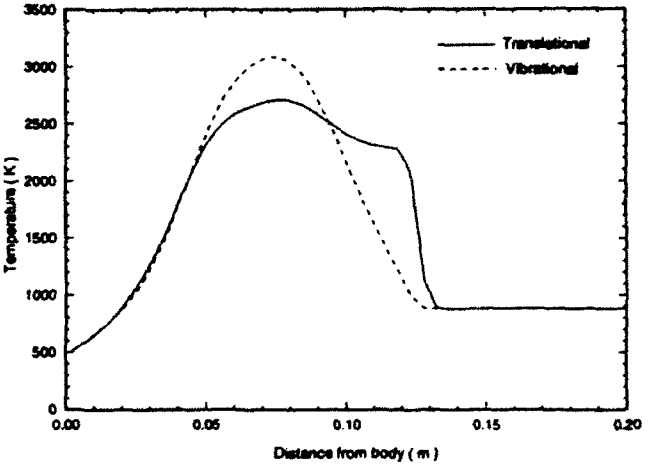

Fig. 14d Temperature profiles along diagnostic station 2 for fake air and geometry with 10° cone angle.

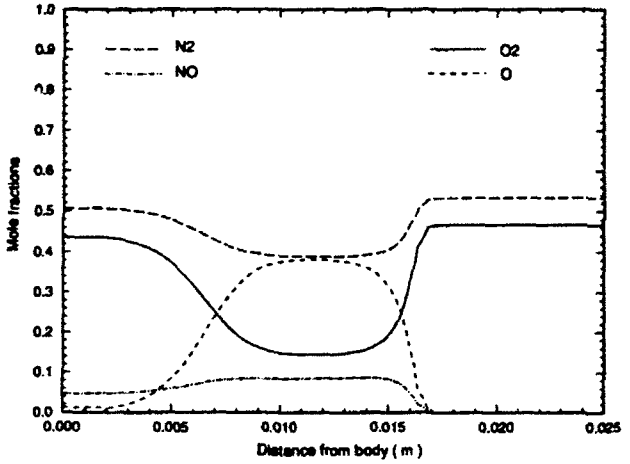

Fig. 14b Mole fraction profiles along stagnation line for fake air and geometry with 10° cone angle.

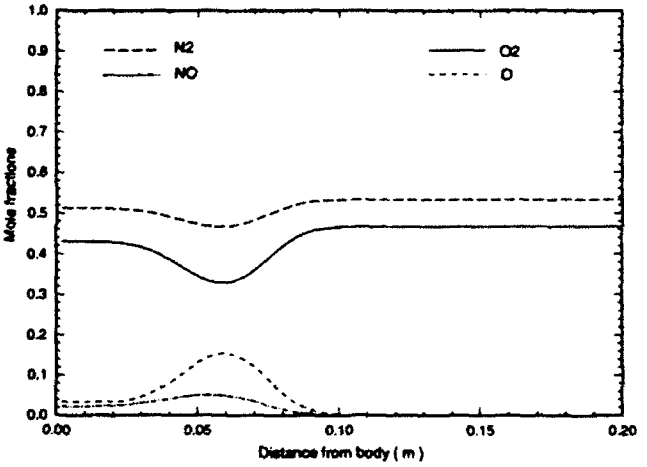

Fig. 14e Mole fraction profiles along diagnostic station 2 for fake air and geometry with 10° cone angle.

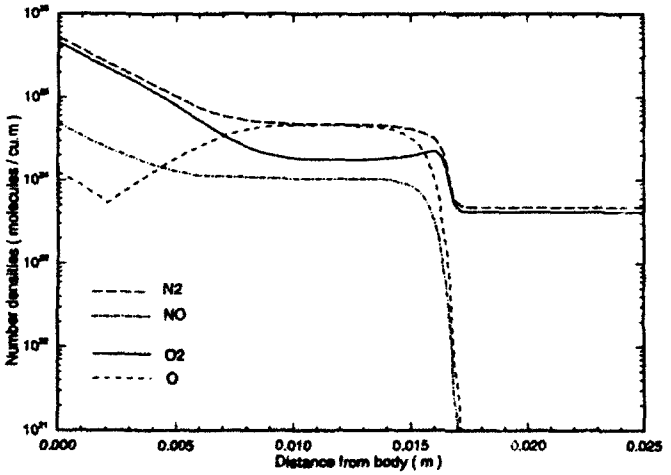

Fig. 14c Number density profiles along stagnation line for fake air and geometry with 10° cone angle.

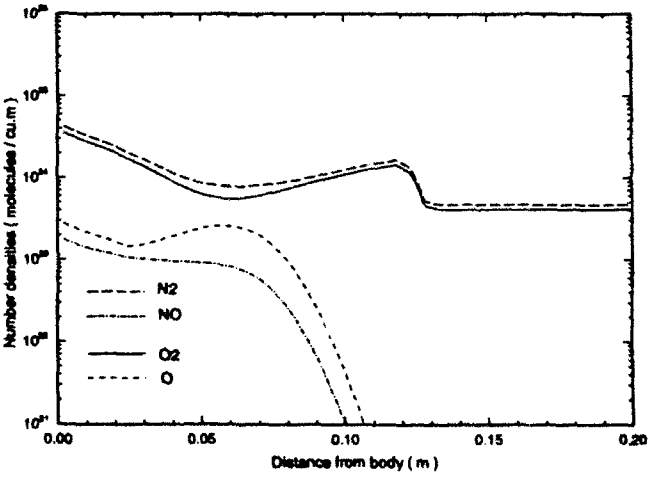

Fig. 14f Number density profiles along diagnostic station 2 for fake air and geometry with 10° cone angle.

AIAA-94-2642

PLIF IMAGING OF TRANSIENT SHOCK PHENOMENA IN HYPERSONIC FLOWS

J.L. Palmer,* A.F.P. Houwing,** M.C. Thurber,* S.D. Wehe,* and R.K. Hanson*

*High Temperature Gasdynamics Laboratory
Department of Mechanical Engineering
Stanford University
Stanford, CA 94305-3032 USA

**Department of Physics and Theoretical Physics
Faculty of Science
Australian National University
Canberra, ACT 0200 Australia

18th AIAA Aerospace Ground Testing Conference

June 20-23, 1994 / Colorado Springs, CO

PLIF IMAGING OF TRANSIENT SHOCK PHENOMENA IN HYPERSONIC FLOWS

J.L. Palmer,*† A.F.P. Houwing,**‡ M.C. Thurber,*† S.D. Wehe,*† and R.K. Hanson*††

*High Temperature Gasdynamics Laboratory
Department of Mechanical Engineering
Stanford University, Stanford, CA 94305-3032 USA

**Department of Physics and Theoretical Physics
Faculty of Science
Australian National University, Canberra ACT 0200 Australia

Abstract

Temporal sequences of planar laser-induced fluorescence (PLIF) images of several high-speed, transient flowfields created in a reflection-type shock tunnel facility were acquired. In each case, the test gas contained either nitric oxide or the hydroxyl radical, which were used as fluorescent species. The processes examined were: shock reflection from an endwall with a converging nozzle; underexpanded free jet formation; and the establishment of a bow shock over a circular cylinder located at the exit of a Mach 3, converging-diverging nozzle. A direct comparison was also made between PLIF imaging and Schlieren photography. The investigation demonstrated some of the capabilities of PLIF imaging diagnostics in complex, transient, hypersonic flowfields, including those with combustion.

I. Introduction

Time-resolved flow visualization can yield insight into many aspects of transient supersonic phenomena. Classical techniques, such as shadow and Schlieren photography and interferometry, have long been applied to the study of high-speed flowfields. Recently, advanced, laser-based diagnostics have been utilized in a variety of supersonic and hypersonic flows, including several with combustion. Here, temporal sequences of planar laser-induced fluorescence (PLIF) images of several transient, supersonic flowfields created in a reflection-type shock tunnel facility have been acquired which demonstrate some of the capabilities of PLIF as a flow visualization tool.

†Graduate Research Assistant, Student Member AIAA.
††Professor, Associate Fellow AIAA.
‡Senior Lecturer, Member AIAA.

The tunnel utilizes the stagnant, high-enthalpy gas, produced by the reflected wave in a shock tube, as it expands through a small, axisymmetric, converging nozzle or a larger, converging-diverging conical nozzle located at the endwall of the tube. An underexpanded free jet flowfield is created at the exit of the converging nozzle, as the gas exhausts into a test section. A large tank is connected past the test section to maintain a constant ambient pressure. A diaphragm may be placed at the exit of the smaller nozzle, between the shock tube and the jet test section and dump tank, allowing an ambient gas with a different composition and pressure than the test gas to be used. Similarly, at the exit of the converging-diverging nozzle, supersonic flow impinges on a cylinder located within the Mach cone of the emerging jet.

PLIF experiments utilize a thin sheet of laser light directed through the flowfield in the desired plane of observation. The laser is tuned to resonantly excite a particular electronic transition of an atomic or molecular species present in the flow. A portion of the fluorescent radiation is collected perpendicular to the observation plane by an optical system and imaged onto a two-dimensional solid-state array. Use of a pulsed laser can provide essentially instantaneous images, which may be acquired with precise timing. The resultant temporally integrated signal may then be analyzed to extract a spatially resolved property field. The repeatability of the flow conditions and structure allowed a single pulsed dye laser and digital camera system to be used here in acquiring a series of PLIF images at different times in sequential firings of the facility.

Several fundamental questions about the evolution of the flow up- and downstream of the converging nozzle have been addressed in this investigation. PLIF imaging of nitric oxide (NO) in the shock tunnel reservoir region was used to examine the shock

reflection process in a test gas seeded with a small amount of NO in argon (Ar). A series of NO PLIF images with high temporal and spatial resolution was acquired, providing midplane views of the flowfield at different delays with respect to the time at which the incident shock reached the endwall. The initial distortion of the reflected shock due to the nonplanarity of the endwall and the resultant perturbations in the reservoir were observable. At long delay times, disturbances arriving from upstream altered the pressure and temperature of the gas, thereby terminating the period of stable reservoir conditions.

Downstream of the converging nozzle, the transient free jet flow was studied using NO PLIF imaging as well. The flow conditions were identical to those used in imaging the stagnation zone; and the images were acquired at the same delay times. The bursting of the diaphragm placed at the nozzle exit and its subsequent passage through the imaged region were observed. The diaphragm's effect on the flow and the time required for its flight out of the field of view were of concern. The process of jet startup to a quasi-steady flow condition is illustrated in detail in these images.

PLIF images of the starting process of the free jet were also obtained by exciting the hydroxyl radical (OH) in a test gas mixture of combustion gases. The flowfield was created by loading Ar with small amounts of hydrogen (H_2) and oxygen (O_2) into the driven section of the shock tunnel. Combustion in the reservoir yielded a gas mixture with ~2% OH. As the gas exhausted through the nozzle, partial chemical freezing occurred, leaving a concentration of OH in the free jet adequate for PLIF imaging of the flowfield. The resulting sequence demonstrates the use of PLIF imaging in a complex, transient combustion flowfield.

The unsteady process leading to the establishment of a stable jet and bow shock before the circular cylinder at the exit of the Mach 3, converging-diverging nozzle has been observed using PLIF of NO. A direct comparison between one of these images and an example from a set of Schlieren photographs obtained under similar condition has also been made. Some of the advantages of planar flow measurements over classical, line-of-sight techniques are illustrated.

PLIF imaging has been applied extensively in this facility during its operation as a shock tube[1-3] and as a shock tunnel.[4-7] Temperature and velocity field measurements have been made in several flowfields, under a variety of flow conditions. The technique used here to construct a sequence of images from several runs of the facility was used previously in characterizing the free jet flow under different experimental conditions with PLIF and shadow photography[4] and in examining shock-induced ignition behind a reflected shock from an endwall with a V-shaped groove which created a combustion kernel.[1]

Transient supersonic flow and shock phenomena have been studied extensively with classical flow visualization techniques.[8] The process of shock reflection and nozzle starting or jet development in a planar nozzle with a rounded or sharp inlet, a transition nozzle, and an orifice plate was examined in detail by Amman and Reichenbach,[9] who obtained temporal sequences of shadowgraphs of these shock tunnel flows. Underexpanded free jet development has also been studied using a variety of classical flow imaging techniques.[10-14] Recently, several investigators have computed the flowfield during the reflection process in a shock tunnel nozzle;[15-18] simulations of jet transients have also been carried out.[13,19]

Other unsteady, supersonic flows with characteristics similar to those of the free jet expansion have been photographed using a variety of classical techniques. These examples include images of the flow from a gun muzzle just prior to the exit of the projectile,[20] shock formation upon diaphragm bursting in a shock tube,[21] a planar shock exiting the open end of a tube,[8,22-25] and diffraction of a shock wave around a convex corner,[26] which has been examined computationally as well.[26,27] Photographs showing the blast wave and gas plume from an ablation target after pulsed laser irradiation[28-30] also display many features in common with underexpanded free jet development.

The process of planar shock wave diffraction around a cylindrical or wedge-shaped obstruction has been studied experimentally with classical imaging techniques,[8,31,32] as well as numerically[16,31,33,34] by many investigators. These transients are closely related to the establishment process of flow over a cylinder located downstream of a shock tunnel nozzle, as considered here. Temporal sequences of Schlieren photographs of the starting process of flow over a wedge at the exit of a planar shock tunnel nozzle have also been obtained previously.[35]

II. Fluorescence Signal

The spectrally and temporally integrated fluorescence signal per unit volume of gas for weak excitation of an isolated absorption line is given by:

$$S = \frac{E_p\, g\, B}{A_{las}} \left(\frac{\chi_a P}{kT}\right) f_J(T) \left(\frac{A}{A+Q}\right) C_{opt} \qquad (1)$$

E_p is the laser pulse energy; g is the spectral convolution of the laser and absorption lineshapes; B is the rate of laser absorption; A_{las} is the cross sectional area of the laser sheet; χ_a is the mole fraction of the absorbing species; P is the pressure; T is the

temperature; k is the Boltzmann constant; $f_J(T)$ is the Boltzmann fraction of the absorbing state; A is the effective rate of spontaneous emission from directly and indirectly populated states; similarly, Q is the total electronic quenching rate of the excited state; and C_{opt} is a constant dependent on optical arrangement, collection efficiency, spectral filtering, temporal gating, etc.

The fluorescence signal is a function of temperature both explicitly, in an inverse manner, and implicitly, through the spectral convolution,[6] Boltzmann fraction,[36] and photon yield ($A/A+Q$). The signal is proportional to the gas pressure, and other pressure dependencies enter through the spectral convolution and photon yield terms. These factors often make the interpretation of an individual PLIF image difficult.

Selection of an absorption feature with an advantageous temperature sensitivity is important when imaging a flowfield with extreme property variations, such as a highly underexpanded free jet. In the experiments under discussion here, the overlapping $R_1+Q_{21}(6)$ transitions in the $A^2\Sigma^+\leftarrow X^2\Pi(0,0)$ band of NO and the $P_1(1)$ transition of the $A^2\Sigma^+\leftarrow X^2\Pi(1,0)$ band of OH at 226.09 and 282.25 nm, respectively, were excited. The temperature dependencies of the lower state population fractions of these lines are shown in Fig. 1. Both absorptions are strongest near 100 K, which is somewhat lower than the minimum temperature expected in the steady-state free jet flowfields. The curves in Fig. 1 suggest that as the temperature drops, an increasing fluorescence signal may be expected, since the signal is proportional to f_J/T, as shown in Eqn. 1. However, since the flow is isentropic, the pressure decreases even more sharply than the temperature as the gas expands. These effects, combined with increases in the spectral convolution and fluorescence yield with decreasing temperature and pressure, minimize the dynamic range of the PLIF signal. Images of the flow with adequate signal level and signal-to-noise ratio (S/N) throughout may thus be acquired. Overall, as will be seen below, the signal tends to decrease inside the core of the jet as the density ($\propto P/T$) falls, yielding a maximum dynamic range in the images of ~50-200 with S/N of ~10-50.

Across a normal shock, however, the signal has the opposite variation with density. The PLIF signal decreases behind the shock, where the temperature and pressure are elevated, primarily due to a decrease in Boltzmann fraction and an increase in electronic quenching. Examples of strong shocks observed in the images obtained here include the incident and reflected shocks in the reservoir region, the primary shocks emerging from the nozzles during their starting

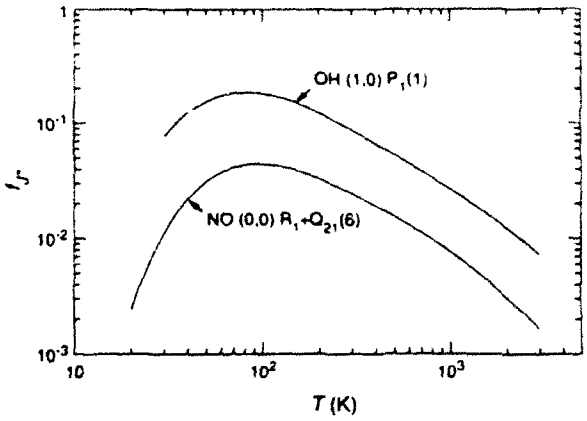

Figure 1: Rotational Boltzmann fractions of the states pumped in the PLIF imaging experiments as a function of temperature.

processes, the Mach disk imbedded in the free jet, and the cylindrical bow shock. The line selection made here tends to maximize the change in PLIF signal across the shocks, while staying within the allowable dynamic range.

III. Experimental Facility and Procedure

A. Shock Tunnel System

The reflection-type shock tunnel facility in which these experiments were performed has been described in detail previously.[4,5] Figure 2 shows a schematic of the facility, along with the PLIF imaging system. The driver section of the tube is 1.5 m in length; and the driven section is 4.5 m long, with a square interior cross section 7.6 cm on a side. Imaging experiments were performed in the reservoir and downstream of the nozzle exit, using two different nozzles. Optical access was achieved through UV-grade fused silica windows mounted in the walls of the reservoir and jet test sections.

The conditions for the three flowfields imaged in this investigation and the throat size of the nozzles used are given in Table 1. The initial pressure, P_1, at which the room temperature test gas was loaded into the facility is given, as is its composition. The conditions listed in the table for the reservoir region, P_s and T_s, are those calculated with one-dimensional shock theory from the measured shock speeds,[4] except in the case of flow #2, where additional chemical kinetics calculations were used to determine the properties.[7]

In the experiments with the converging nozzle (with throat diameter, D = 4.9 mm, flows #1 and 2), a diaphragm consisting of a 6 mm diameter circle of clear plastic tape was placed at the exit of the nozzle. The ambient gas composition and initial pressure were then allowed to differ from those of the test gas. With the Mach 3, conical nozzle (D = 17.5 mm, flow #3) in

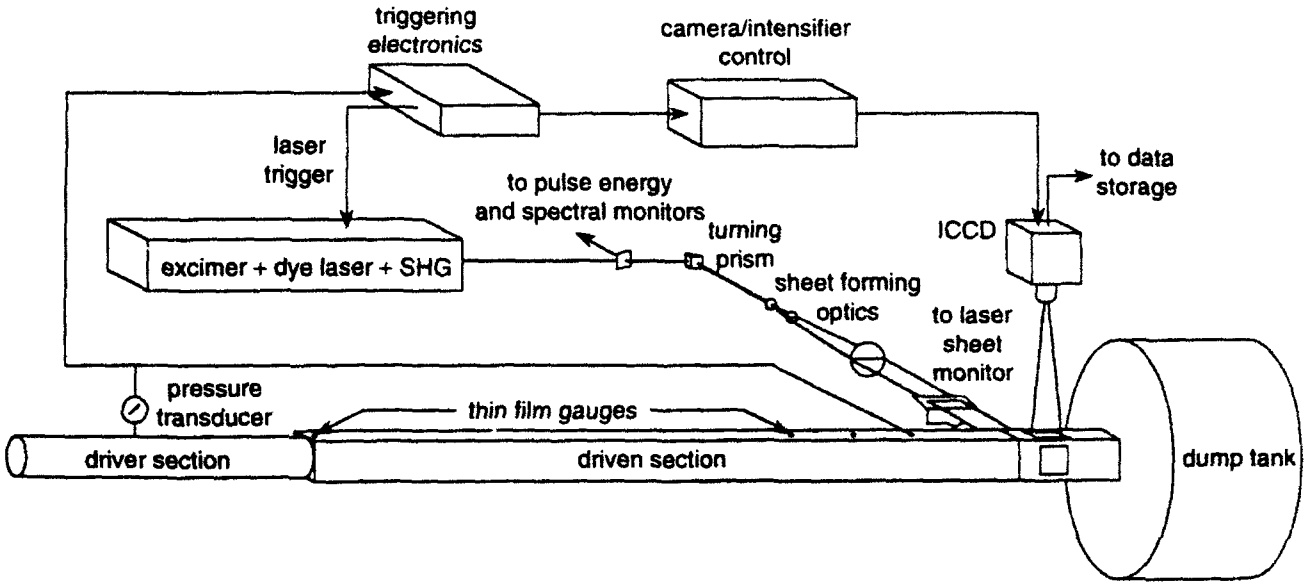

Figure 2: Schematic of experimental facility with associated optical and electronic components for PLIF imaging.

place, no diaphragm was used; and a single gas was loaded on both sides of the nozzle. The ambient gas composition, along with the ratio of the stagnation pressure of the reservoir gas to the ambient pressure, P_s/P_a, is given in Table 1 for each flow.

B. PLIF Imaging System

The technique used in imaging each of the flowfields considered here is listed in Table 1, along with the electronic transition that was pumped and the physical dimensions of the resulting images. Figure 3 shows the imaging geometry for each of the three cases. In all of the images, the primary flow is from left to right and the laser traverses the field of view from top to bottom.

Frequency-doubled photons from a tunable XeCl-pumped dye laser with Coumarin 450 or 540A dye were used to excite transitions in the $A^2\Sigma^+ \leftarrow X^2\Pi(0,0)$ band of NO and in the $A^2\Sigma^+ \leftarrow X^2\Pi(1,0)$ band of OH at 226 and 282 nm, respectively. In most regions of the flowfields, the laser was significantly broader than the absorption. The laser linewidth was ~0.35-0.45 cm^{-1}; while the absorption linewidth varied between 0.05 and 0.3 cm^{-1}. A thin, horizontal sheet of laser light was created using a series of lenses. Two cylindrical lenses telescoped the UV beam horizontally, expanding and then recollimating it to a width of 5-10 cm. A spherical lens focused the beam vertically to a thickness of ~350 μm at the flow axis. The portion of the laser sheet which passed through the imaged region had 0.25-0.5 mJ in each 30 ns pulse.

Broadband fluorescence resulting from excitation of the test gas by a single laser pulse was collected normal to the direction of laser propagation, as shown in Fig 2. The light was imaged onto a 578 × 384 pixel, cooled, intensified CCD array with a Nikkor UV lens (f/4.5) and then transferred to computer. Spectral filtering eliminated elastic scattering and fluorescence from the excited ro-vibrational bands, while allowing detection of radiative relaxation in bands with longer wavelengths. Further details of the specific implementation of the PLIF diagnostic for the NO imaging are given in Refs. 5 and 6 and for the OH imaging in Ref. 7.

flow #	test gas composition	P_1 (torr)	P_s (atm)	T_s (K)	ambient gas composition	D (mm)	P_s/P_a	imaging technique	line(s) pumped	flowfield imaged	image size (mm)	image size (pixels)
1	0.5% NO/Ar	60	2.5	1600	0.5% NO/Ar	4.9	190	NO PLIF	(0,0) $R_1 + Q_{21}(6)$	reservoir	34.1 × 53.9	117 × 185
										jet	41.2 × 28.3	266 × 183
2	5% H_2/5% O_2/Ar	22	3.2	3350	Ar	4.9	61	OH PLIF	(1,0) $P_1(1)$	jet	43.5 × 29.0	187 × 125
3	0.05% NO/Ar	60	4.3	2500	0.05% NO/Ar	17.5	54	NO PLIF	(0,0) $R_1 + Q_{21}(6)$	cylinder	31.3 × 46.2	128 × 189

Table 1: Conditions of shock tunnel imaging experiments.

The timing of the laser shot, intensifier activation, and image acquisition was synchronized electronically using a series of delays. A trigger signal from the pressure transducer located in the driver section initiated charging of the excimer laser capacitor banks just prior to diaphragm rupture. The thin film gauge closest to the shock tube endwall was used to initiate the sequence required to fire the laser/intensifier/camera system and to obtain a single PLIF image. A variable time delay which began the trigger sequence allowed observation of the flowfield at any desired time with respect to the moment at which the incident shock reached the shock tube endwall. The uncertainty in the delay time for each image was ± 2 μs, due to slight variations in the incident shock speed.

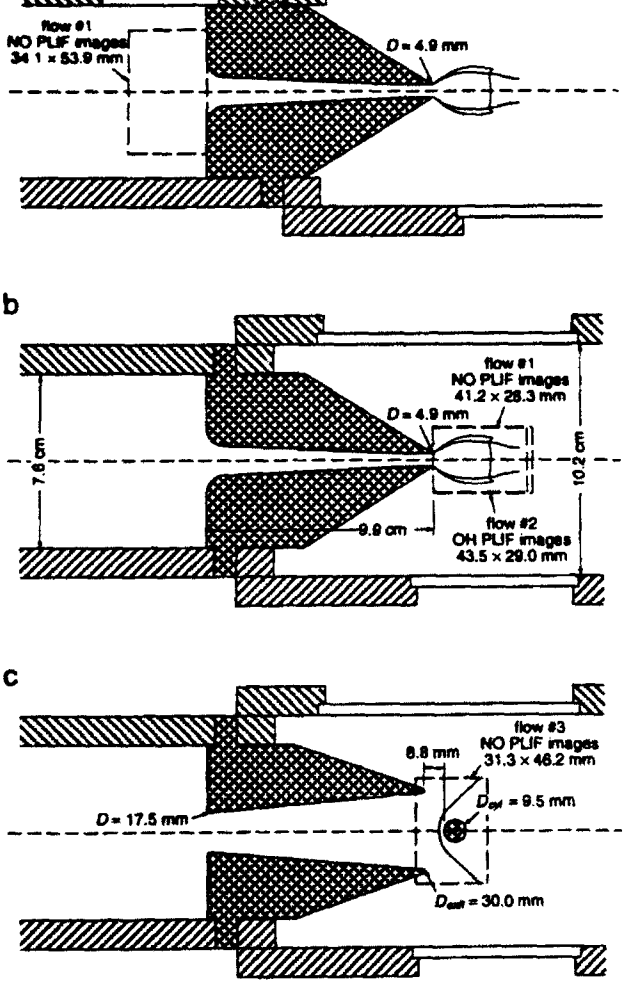

Figure 3. Fields of view used in PLIF imaging experiments: reservoir transient (a), free jet development (b), and development of flow over a cylinder (c).

The procedures described by Seitzman, et al.,[3] were used to correct the raw data images for single-shot laser sheet intensity variations, nonuniform collection efficiency, laser scattering, and background signal level on a pixel-by-pixel basis. Emission from the test gas, other than that induced by laser excitation, was neglected, since no signal above background was observed in images acquired in the usual way, but with the laser blocked. Following correction, the image pixels were binned (2 × 2 or 3 × 3) and the results trimmed to center them about the jet axis. Table I lists the final sizes of the images.

V. Results and Discussion

A. NO PLIF Imaging of Shock Reflection and Jet Formation

Figure 4 shows two series of NO PLIF images obtained in this investigation. The left image of each pair shows the shock tunnel reservoir region, bordering the endwall of the tube on the right, as shown in Fig. 3a; while that to the right shows the region downstream of the exit of the converging nozzle with D = 4.9 mm, as in Fig. 3b. The physical dimensions of the images and the conditions of the flowfield are given in table I as flow #1.

The scales to the far right of the image sequences indicate the signal levels corresponding to the gray tones in the images. Logarithmic scaling was used in both cases to increase the visibility of details in regions of the images with low relative signal. The signal in the reservoir images was inverted before being displayed so that the low signals (high densities) are represented by white and the high signals (low densities) by black. In the jet images, high signals are shown in white and low signals in black. The density does not strictly increase with signal level in the jet images, although the trend is for higher densities to be represented with white and lower ones with black, particularly inside the jet core beyond one diameter from the nozzle. The temperature sensitivity of the excited spectral feature of NO and the variations of the gas properties in the flowfields account for this apparent contradiction in signal dependence on density in the two imaged regions (see Sect. II).

The first frame (a) of the reservoir image sequence shows the incident shock 15 μs prior to its reflection from the endwall, as it traveled into the stagnant test gas at 820 ± 5 m/s. In the next three frames (b-d), the nonplanar reflected shock is visible. Secondary shocks behind the primary wave are also observable, particularly in image c, where a curved, outwardly-propagating conical shock extended from the primary wave back to the endwall. The circular intersection of

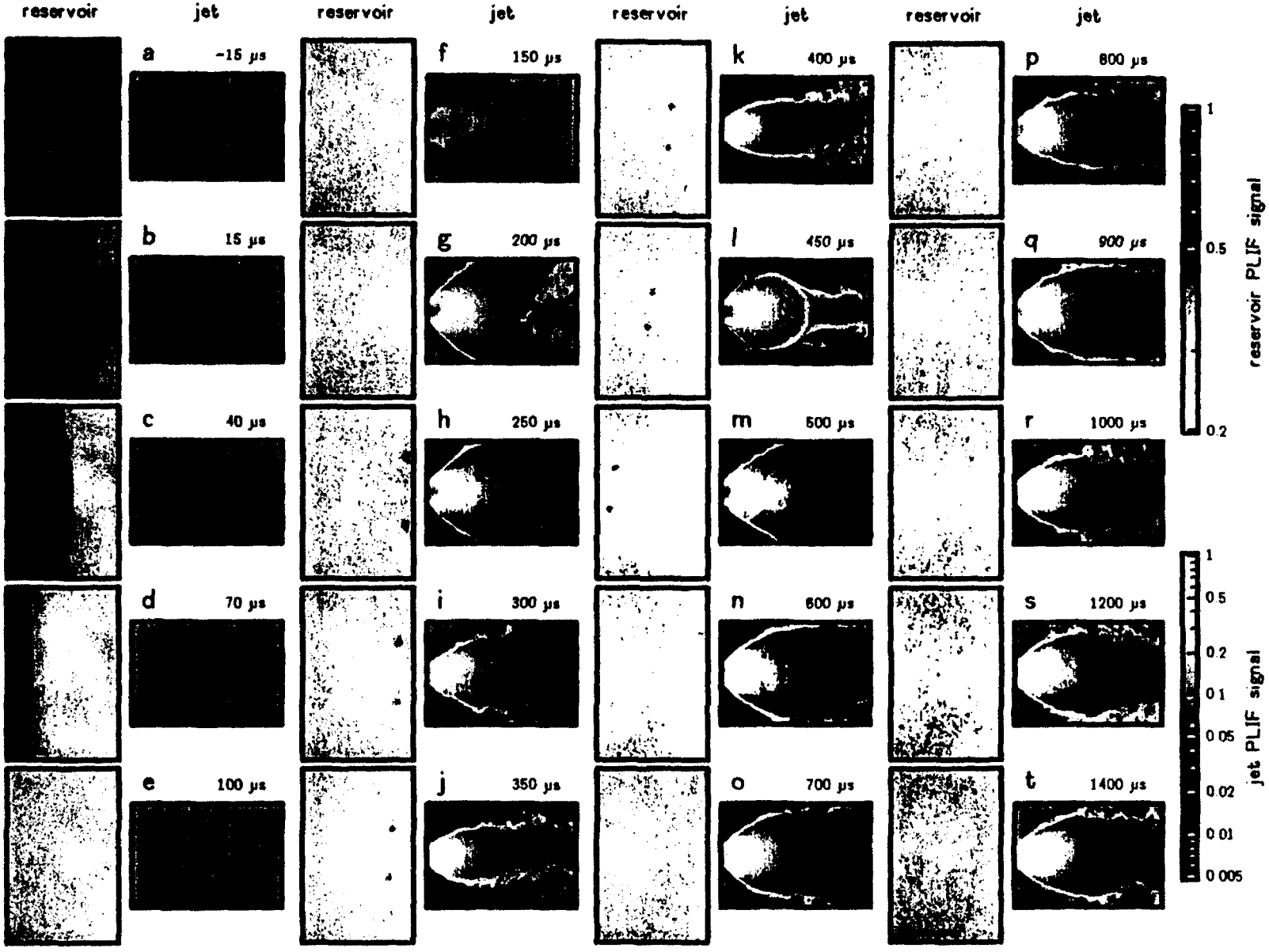

Figure 4: NO PLIF images of shock tunnel reservoir and free jet regions showing the transient flow process. The conditions used are listed in Table 1 as flow #1; the imaged areas are shown in Figs. 3a and b.

these waves quickly moved outward, as can be seen by comparing frames c and d, taken 30 ± 2 μs apart.

In frames e and f, disturbances in the reservoir caused by the flow of gas into the nozzle are visible. A compressive disturbance, seen as a bright, mushroom-shaped object in images g and beyond, then emerged from the nozzle entrance and propagated upstream. At the lip of the nozzle entrance, a vortex ring, appearing in the images as two dark circular spots, was generated behind this wave. As the vortex ring traveled upstream and eventually exited the field of view (frames h-m), outflow through the nozzle continued and stable, though nonuniform, conditions persisted in the reservoir region for nearly 800 μs (frames n-r). The final images in the reservoir sequence (s and t) show an increase in signal level, caused by a decrease in temperature and pressure, as expansion waves from upstream arrived at the endwall, thereby ending the period of steady conditions in the nozzle reservoir.

In Fig. 4, the first images of the free jet region (a-e) show only the stagnant ambient gas, as the primary shock wave had not yet traversed the nearly 10 cm long nozzle. In jet frame f, taken 150 μs after the incident shock reached the endwall, gas was observed emerging from the nozzle for the first time. A round blast wave-like shock emanated into the stagnant ambient region, from which a PLIF signal was also obtained because of the small NO concentration of the ambient gas. Turbulence was introduced into the flow exiting the nozzle by the bursting of the circle of plastic tape used as a diaphragm at the nozzle exit. Pieces of the diaphragm can be seen as a bright spot beyond which there is no PLIF signal because the tape lay in the laser sheet and as a dark spot closer to the nozzle, caused by a fragment between the observation plane and the camera. The free jet grew rapidly in size, assuming a characteristic barrel shape, as seen in frames g and h. The diaphragm fragments are observable in these images for the last time, as they were pushed downstream, out of the field of view. Once out of the jet core (after ~250 μs), they no longer influenced its behavior; and the transient proceeded as though no diaphragm had initially been present.[4]

Following the expansion of the blast wave and jet gas in frames f-h, a recompression of the free jet took place as reflected waves traveled back to the flow axis from the sidewalls of the test section. This phenomena is observed in the jet images shown in Figs. 4i-k. The process of the jet's reforming and re-expanding past its equilibrium size was repeated in frames l and m. In several runs of the experiment performed at each of these times, it was found that the occurrence of this cyclical process was highly repeatable. Beyond ~600 μs, the free jet was fairly stable, with variations in the barrel shock structure caused by weak interactions with the walls of the test section. Jet images m-t, acquired up to and including the point of observable reservoir degradation (frames s and t), display a relatively constant signal variation with position inside the jet core, indicating stable gas properties there. Small deviations of the overall signal level or symmetry about the jet axis resulted from shot-to-shot changes in the laser spectral lineshape,[4-6] which affects the PLIF signal through the spectral overlap term, as shown in Eqn. 1.

B. OH PLIF Imaging of Jet Formation

A sequence of OH PLIF images illustrating the formation of a supersonic free jet of combustion gases is displayed in Fig. 5. Details of the flow conditions and the imaging technique used are given in Table 1 and in Fig. 3b. The gray scale to the right of the images indicates the relationship between the PLIF signal level and the tones in the images. Again, logarithmic scaling was used; and the highest signal is represented with white while the lowest signal is shown in black.

The test gas, containing approximately 2% OH by volume, emerged from the nozzle ~110 μs after the incident shock wave reached the endwall of the tube. Figure 5a shows the jet region just after gas began to exhaust into the test section. In frame b, a moment in the evolution of the flow was captured that was also observed in the jet image of Fig. 4f. As seen previously in the NO PLIF images of the jet transient, diaphragm particles were initially imbedded in the jet. They were quickly propelled downstream by the gas plume, as seen in frames a-d. The establishment of the barrel shock structure took place promptly; and again, the jet was observed expanding into the test section (frames c and d) and then being compressed by inwardly-propagating shocks reflected from the walls (frames e-g). In frame e, a structure closely resembling a laminar flame sheet is observable. The final frames, h and i, show the underexpanded free jet in an apparently quasi-steady state, likely having an unsteady shock position and shape similar to that noted above in discussion of the NO PLIF jet images.

The ambient gas in this case yielded no fluorescence signal, since it contained only Ar. The test gas was diluted and OH radicals chemically quenched by mixing with the ambient, leading to low PLIF signals outside of the jet core. The region downstream of the Mach disk, where elevated temperatures led to enhanced chemical nonequilibrium and mixing had yet to take place, was an exception. The location of the highest PLIF signal was, however,

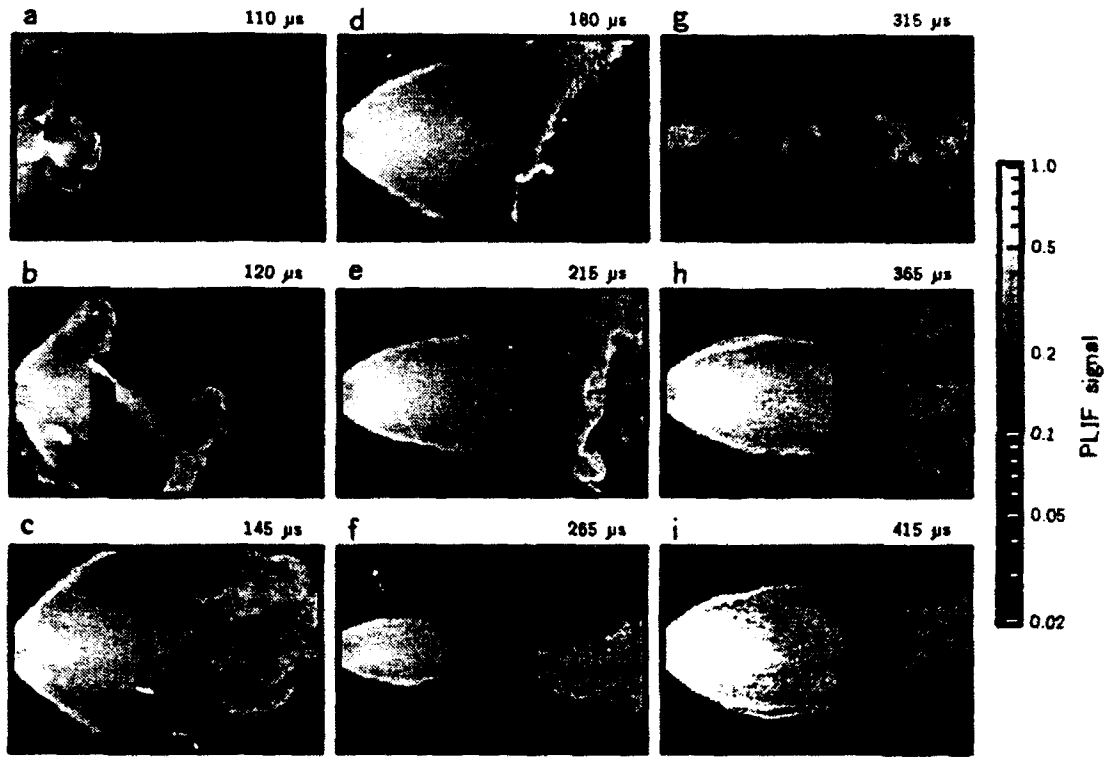

Figure 5: OH PLIF images of the development of a free jet issuing from a sonic nozzle. The conditions used are listed in Table 1 as flow #2; the imaged area is shown in Fig. 3b.

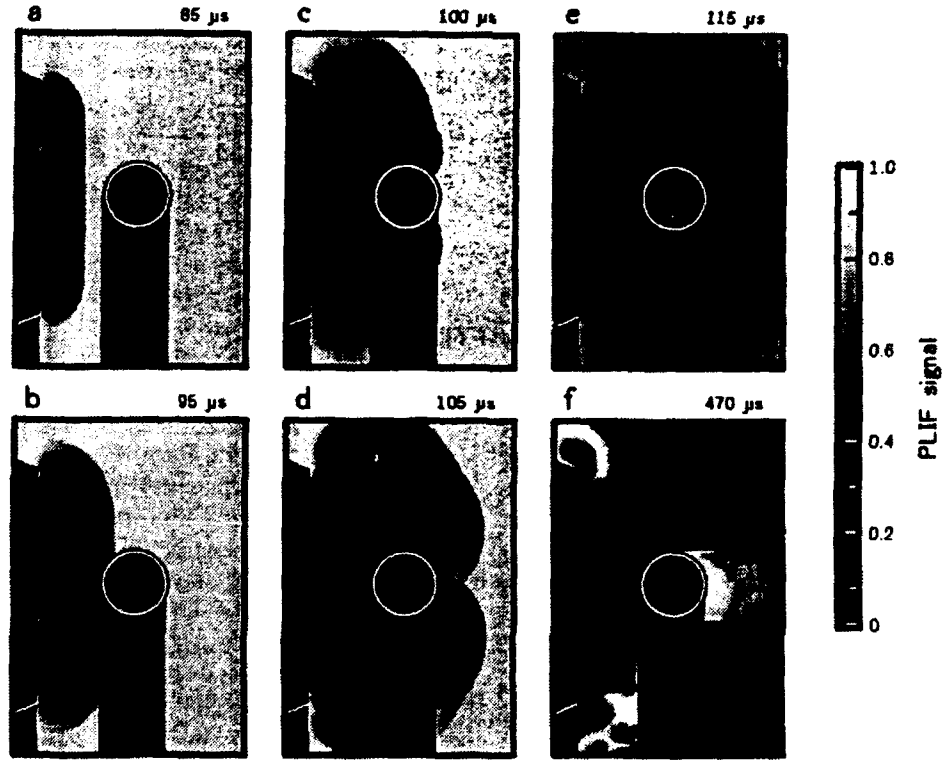

Figure 6: NO PLIF images of the development of a bow shock over a cylinder downstream of the Mach 3 nozzle exit. The conditions used are listed in Table 1 as flow #3; the imaged area is shown in Fig. 3c.

inside the jet core, within a few diameters of the nozzle exit. Due to the combined effects of the changing flow conditions and the temperature dependence of the absorption line chosen, the region of highest density did not yield the highest PLIF signal in the images.

C. NO PLIF Imaging of Development of Flow over a Cylinder

Figure 6 shows a series of NO PLIF images obtained at the exit of a Mach 3, conical nozzle in the shock tunnel facility. The conditions of the gas and the size and geometry of the images is given in Table 1 and in Fig. 3c. The 9.5 mm diameter cylinder and the lower edge of the nozzle have been highlighted in the images, to aid the reader's understanding. Masking was applied to these images to eliminate signal artifacts where the laser sheet was blocked by these objects. At the far right side of Fig. 6, a gray bar shows the tone used to represent a given PLIF signal level in the images. The highest signal level is shown in white and the lowest in black in the images. The trend in this sequence is for higher densities to be shown in black and lower densities in white.

No diaphragm was used between the reservoir and ambient regions; therefore, the ambient conditions were identical to those of the test gas in the shock tube prior to the arrival of the incident wave. The early images in the sequence (frames a and b) show an organized flow exiting the nozzle, in contrast with the initially turbulent flow observed at the exit of the converging nozzle in the previous two examples, where a diaphragm was used. The smooth, laminar flow pattern observed is reminiscent of that seen as gas expands from a converging nozzle without a diaphragm.[4]

As soon as the jet gas reached the cylinder, a bow shock began to develop, as seen in Fig. 6b. The shock layer grew rapidly about the cylinder as the gas advanced into the test section, as seen in frames b-d, taken over a time interval of only 10 ± 2 μs. Complex shock interaction patterns are visible in frames c and d after the initial simple wave reflection at the cylinder surface became a Mach reflection upon moving further around the body. Vortical structures behind the cylinder are visible in frame e, which indicate the formation of a turbulent wake. The quasi-steady flowfield comprising a Mach 3 jet impinging on a cylinder located within its Mach cone is shown in frame f, taken 470 μs after the incident shock reached the endwall and the entrance of the nozzle. The bow shock structure reached an equilibrium and its final stand-off distance from the body is seen to be smaller than that observed in the earlier images.

Figure 7 provides a direct comparison between one of the NO PLIF images shown in Fig. 6 and a Schlieren photograph obtained under the same experimental conditions using a video camera, a 30 ns duration light source,[4] and a vertical knife edge, frames a and b, respectively. In the Schlieren image, the full outline of the nozzle is visible as well as the support for the cylinder, a sting located well out of the midplane of the flowfield so as not to affect the flow imaged in the PLIF experiments. As was done previously, a white circle has been placed in the Schlieren image to indicate the position of the cylinder; and masking has been used to eliminate the signal in regions of the image where the nozzle, cylinder, or sting blocked the transmitted light. The Schlieren image was corrected for nonuniform illumination after being background subtracted. The dimensions of the resulting centered, trimmed image are 31.1 × 44.9 mm over 202 × 291 pixels.

The bow shock is clearly defined in both images, taken at a delay of 100 ± 2 μs, as are the shock structures toward the rear of the cylinder. The slight discrepancy in the locations of the primary features of the flow are attributable to the uncertainty in the timing of the images and the cylinder's being slightly closer to the nozzle exit in the Schlieren image (frame b) than in the PLIF image (frame a). The vortex ring, visible as dark regions near each side of the nozzle in frame a, is less obvious in the Schlieren image, due to the line-of-sight nature of the measurement and the fact that the structure is axisymmetric and of rather small extent. Bright, curved lines in the Schlieren image near the edges of the nozzle suggest a structure across or around the nozzle exit. However, interpretation of the image is more difficult than for the PLIF images.

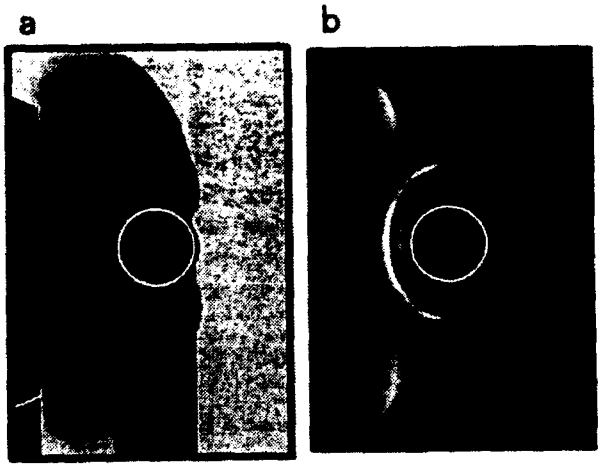

Figure 7: Comparison of (a) a frame from the NO PLIF image series shown in Fig. 6 and (b) a Schlieren image taken at a similar delay time, 100 ± 2 μs, under the same flow conditions.

VI. Summary and Conclusions

The flow characteristics up- and downstream of a small, axisymmetric, converging nozzle were observed in PLIF images of the shock reflection and free jet development processes with a test gas of Ar seeded with NO. A qualitative indication of the degree of disturbance of the reservoir caused by the nozzle was obtained. Stable reservoir conditions of 1600 K and 2.5 atm were found to exist for ~800 μs, for the flow considered here. In another image sequence acquired downstream of the nozzle, the unsteady process leading to the development of an underexpanded free jet was observed. The presence of a diaphragm at the nozzle exit was found to strongly affect the flow initially. However, ~100 μs after bursting, its fragments were pushed out of the jet and had no further influence on the main flow. The quasi-steady free jet was established within ~500 μs of the primary shock exiting the converging nozzle. After that time, images showed that the jet core was steady, although the size and shape of the surrounding barrel shock varied because of lateral wave reflections inside the test section.

Free jet formation was also observed in a series of OH PLIF images, using a reservoir with a mixture of combustion gases diluted in Ar with ~2% OH at 3350 K and 3.2 atm. As was the case previously, a great deal of detail was visible in the images. The high *S/N* of the signal, high spatial resolution, and flow-stopping temporal resolution allowed particularly fine visualization of the transient reacting flowfield. Many of the features seen in the NO jet images were observed, the most notable being the cyclical nature of the starting process. The flow was found to stabilize ~350 μs after shock reflection.

A conical, converging-diverging nozzle was used to produce a supersonic flow at Mach 3 which impinged on a circular cylinder located downstream of the nozzle exit. The process leading to formation of a bow shock in front of the cylinder was captured using PLIF of NO. A comparison was also made between PLIF imaging and Schlieren photography of this flowfield. The complementarity of the two techniques was illustrated, although it was found that PLIF imaging provided information unobtainable with a line-of-sight technique.

Several aspects of imaging demonstrated in this investigation confirm that PLIF is an excellent flow visualization tool. The spatial resolution inherent in a planar measurement allows a better understanding of complex, three-dimensional flowfields than is possible with traditional, line-of-sight techniques. PLIF imaging performed with a pulsed laser source provides the temporal resolution needed to capture the evolution of transient, hypersonic flows. Use of strongly fluorescent seeded or naturally-occurring tracers, such as NO and OH, yields images with a high degree of in-plane spatial resolution and adequate *S/N* to allow observation of important details in the flow.

Acknowledgment

The authors gratefully acknowledge the contributions of Drs. J.M. Seitzman and B.K. McMillin to this investigation. The work was supported by the U.S. Air Force Office of Scientific Research, Aerospace Sciences Directorate.

References

1. B.K. McMillin, M.P. Lee, P.H. Paul, and R.K. Hanson, "Planar Laser-Induced Fluorescence Imaging of Shock-Induced Ignition," *23rd Symp. (Int'l.) on Combustion*, The Combustion Institute, Pittsburgh, 1990, pp. 1901-1914.

2. B.K. McMillin, J.L. Palmer, and R.K. Hanson, "Temporally Resolved, Two-Line Fluorescence Imaging of NO Temperature in a Transverse Jet in a Supersonic Cross Flow," *Appl. Opt.*, Vol. 32, No. 36, pp. 7532-7545 (1993).

3. J.M. Seitzman, J.L. Palmer, A.L. Antonio, R.K. Hanson, P.A. DeBarber, and C.F. Hess, "Instantaneous Planar Thermometry of Shock-Heated Flows Using PLIF of OH," AIAA Paper No. 93-0802.

4. J.L. Palmer, B.K. McMillin, and R.K. Hanson, "Planar Laser-Induced Fluorescence Imaging of Underexpanded Free Jet Flow in a Shock Tunnel Facility," AIAA Paper No. 91-1687.

5. J.L. Palmer and R.K. Hanson, "Planar Laser-Induced Fluorescence Imaging in Free Jet Flows with Vibrational Nonequilibrium," AIAA Paper No. 93-0046.

6. J.L. Palmer and R.K. Hanson, "Single-Shot Velocimetry Using Planar Laser-Induced Fluorescence Imaging of Nitric Oxide," AIAA Paper No. 93-2020.

7. J.L. Palmer and R.K. Hanson, "PLIF Measurements of Temperature and Velocity in a Reacting Supersonic Free Jet With OH," AIAA Paper No. 94-0618.

8. H. Oertel, "33 Years of Research by Means of Shock Tubes at the French-German Research Institute at Saint-Louis," *Shock Tubes and Waves, Proc. of the 14th Int'l. Symp. on Shock Tubes and Shock Waves*, Sydney, Australia, 1983, pp. 3-13.

9. H.O. Amman and H. Reichenbach, "Unsteady Flow Phenomena in Shock-Tube Nozzles," *9th Int'l. Shock Tube Symp.*, Stanford, CA, 1973, pp. 96-112.

10. V.G. Maslennikov and B.M. Dobrynin, "Onset of Quasi-Steady Flow Structure in the Initial Portion of Two-Dimensional Nitrogen Jets for Different Values of the Environmental Pressure," *Sov. Phys. Tech. Phys.*, Vol. 26, No. 6, pp. 698-702 (1981).

11. B. Sturtevant and S.W. Kieffer, "Vapor Explosions and the Blast Wave at Mt. St. Helens," *Shock Tubes and Waves, Proc. of the 14th Int'l. Symp. on Shock Tubes and Shock Waves*, Sydney, Australia, 1983, pp. 17-25.

12. V.V. Golub, A.I. Kharitonov, Y.L. Sharov, and A.M. Shulmeister, "Two-Direction Visualization of Vortex Rings Emerging in the Course of Formation of the Supersonic Jet," *Flow Visualization V, Proc. of the 5th*

Int'l. Symp. on Flow Visualization, Prague, Czechoslovakia, 1989, ed., R. Reznick, pp. 556-561.

13. S. Matsumura, N. Sekine, K. Takayama, and O. Onodera, "Flow Visualization Study of Shock Waves in Automobile Exhaust Systems," *Flow Visualization V, Proc. of the 5th Int'l. Symp. on Flow Visualization*, Prague, Czechoslovakia, 1989, ed., R. Reznick, pp. 779-784.

14. A.V. Emel'yanov and A.V. Eremin, "Generalised Empirical Laws of Starting Discontinuity Dynamics Associated with the Startup of Underexpanded Jets," *J. Appl. Mech. Tech. Phys.*, Vol. 32, No. 5, pp. 665-669 (1991).

15. A.B. Britan, A.Ya. Rudnitskii, and A.M. Starik, "Parameter Formation Behind the Reflected Wave in a Shock Tube with a Nozzle," *Fluid Dyn.*, Vol. 22, No. 4, pp. 622-628 (1987).

16. P.A. Jacobs, "Simulation of Transient Flow in a Shock Tunnel and a High Mach Number Nozzle," NASA CR 187606, ICASE Rept. No. 91-60, Jul., 1991.

17. P. Prodromou and R. Hillier, "Computation of Unsteady Nozzle Flows," *24th Symp. (Int'l.) on Combustion*, The Combustion Institute, Pittsburgh, 1992, pp. 1113-1118.

18. J.Y. Yang, C.A. Hsu, C.T. Jiang, and B. Miller, "Computation of Shock Diffraction in External and Internal Flows," *24th Symp. (Int'l.) on Combustion*, The Combustion Institute, Pittsburgh, 1992, pp. 1063-1068.

19. M.L. Norman, L. Smarr, K.-H.A. Winkler, and M.D. Smith, "Structure and Dynamics of Supersonic Jets," *Astron. Astrophys.*, Vol. 113, pp. 285-302 (1982).

20. K. Oswatitsch, *Contributions to the Development of Gasdynamics*, eds., W. Schneider and M. Platzer, Friedr. Vieweg and Sohn, Braunschweig, Wiesbaden, 1980, p. 347.

21. M.A. Liberman and A.L. Velikovich, *Physics of Shock Waves in Gases and Plasmas*, Springer-Verlag, NY, 1986, p. 64.

22. K.C. Phan and J.L. Stollery, "The Effect of Suppressors and Muzzle Brakes on Shock Wave Strength," *Shock Tubes and Waves, Proc. of the 14th Int'l. Symp. on Shock Tubes and Shock Waves*, Sydney, Australia, 1983, pp. 519-526.

23. A. Abe and K. Takayama, "Shock Wave Diffraction from the Open End of a Shock Tube," *AIP Conf. Proc. No. 208: Current Topics in Shock Waves, 17th Int'l. Symp. on Shock Waves and Shock Tubes*, Bethlehem, PA, 1989, ed., Y.W. Kim, pp. 270-275.

24. S.B. Bazarov, T.V. Bazhenova, O.V. Bulat, V.V. Golub, and A.M. Shulmeister, "Three-Dimensional Diffraction of Shock Wave," *Shock Waves, Proc. of the 18th Int'l. Symp. on Shock Waves*, Sendai, Japan, 1991, ed., K. Takayama, pp. 251-254.

25. Y. Da-Peng, M. Peng-Cheng, W. Hai-Lin, and H. An-Zhi, "The Methods of Extracting and Registering Shock Wave-fronts from Series Interferograms of Transient Flow Field," *Proc. of the SPIE, Interferometry: Techniques and Analysis*, San Diego, CA, 1992, pp. 184-189.

26. R. Hillier and M.J. Netterfield, "Computation of Shock Wave Diffraction and Unsteady Shock-Boundary Layer Interaction," *AIP Conf. Proc. No. 208: Current Topics in Shock Waves, 17th Int'l. Symp. on Shock Waves and Shock Tubes*, Bethlehem, PA, 1989, ed., Y.W. Kim, pp. 228-233.

27. K. Matsuo, T. Aoki, and H. Kashimura, "Diffraction of a Shock Wave Around a Convex Corner," *AIP Conf. Proc. No. 208: Current Topics in Shock Waves, 17th Int'l. Symp. on Shock Waves and Shock Tubes*, Bethlehem, PA, 1989, ed., Y.W. Kim, pp. 252-257.

28. R. Srinivasan, "A Comparative Study of the Ablation of Polyimide (Kapton) Films by Pulsed(ns) Ultraviolet and Infrared(9.17 mm) Lasers," *AIP Conf. Proc., Laser Ablation: Mechanisms and Applications II, 2nd Int'l. Conf.*, Knoxville, TN, 1993, eds., J.C. Miller and D.B. Geohegan, pp. 439-443.

29. R. Kelly and A. Miotello, "Pulsed-Laser Sputtering of Atoms and Molecules. Part I: Basic Solutions for Gas-Dynamic Effects," *Appl. Phys. B*, Vol. B57, pp. 145-158 (1993)

30. J. Palau, P. Serra, M. Varela, J. Esteve, F. Sanchez, and J.L. Morenza, "Time and Oxygen Background Pressure Dependence of $YBa_2Cu_3O_7$ Laser-Ablated Plumes Analyzed by Fast Intensified-CCD Imaging," *AIP Conf. Proc., Laser Ablation: Mechanisms and Applications II, 2nd Int'l Conf.*, Knoxville, TN, 1993, eds., J.C. Miller and D.B. Geohegan, pp. 427-432.

31. I.I. Glass, J. Kaca, D.L. Zhang, H.M. Glaz, J.B. Bell, J.A. Trangenstein, J.P. Collins, "Diffraction of Planar Shock Waves over Half-Diamond and Semicircular Cylinders An Experimental and Numerical Comparison," *AIP Conf. Proc. No. 208: Current Topics in Shock Waves, 17th Int'l. Symp. on Shock Waves and Shock Tubes*, Bethlehem, PA, 1989, ed., Y.W. Kim, pp. 246-251

32. H. Sugiyama, T. Arai, H. Nagumo, H. Sueki, M. Izumi, and K. Takayama, "An Experimental and Numerical Study of the Shock Wave-Induced Flows Past a Circular Cylinder in a Dusty-Gas Shock Tube," *AIP Conf. Proc. No. 208: Current Topics in Shock Waves, 17th Int'l. Symp. on Shock Waves and Shock Tubes*, Bethlehem, PA, 1989, ed., Y.W. Kim, pp. 258-263.

33. C.E. Needham, D.F. Dawson, and J.E. Crepeau, "Shock Diffraction over a Flat Plate," *Shock Waves, Proc. of the 18th Int'l. Symp. on Shock Waves*, Sendai, Japan, 1991, ed., K. Takayama, pp. 246-250.

34. S. Sivier, J. Baum, E. Loth, and R. Lohner, "Vorticity Produced by Shock Wave Diffraction," *Shock Waves, Proc. of the 18th Int'l. Symp. on Shock Waves*, Sendai, Japan, 1991, ed., K. Takayama, pp. 143-150.

35. C.E. Smith, "The Starting Process in a Hypersonic Nozzle," *J. Fluid Mech.*, Vol. 24, Part 4, pp. 625-640.

36. W.G. Vincenti and C.H. Kruger, Jr., *Introduction to Physical Gas Dynamics*, Wiley, N.Y., 1965.